Adhesion and friction effects in soft contact mechanics: from shell buckling to viscoelastic rolling

Politecnico di Bari

LIBERATORIA PER L'ARCHIVIAZIONE DELLA TESI DI DOTTORATO

Al Magnifico Rettore
del Politecnico di Bari

Il/la sottoscritto/a **Roohollah Nazari** nato/a a **IRAN** il **02/04/1993**

residente a **Bari** in via Nicola Bavaro 47 email **r.nazari@phd.poliba.it**

iscritto al 3° anno di Corso di Dottorato di Ricerca in **Mechanical Engineering__** ciclo_**38**

ed essendo stato ammesso a sostenere l'esame finale con la prevista discussione della tesi dal titolo:

Adhesion and Friction Effects in Soft Contact Mechanics: From Shell Buckling to Viscoelastic Rolling

DICHIARA

1) di essere consapevole che, ai sensi del D.P.R. n. 445 del 28.12.2000, le dichiarazioni mendaci, la falsità negli atti e l'uso di atti falsi sono puniti ai sensi del codice penale e delle Leggi speciali in materia, e che nel caso ricorressero dette ipotesi, decade fin dall'inizio e senza necessità di nessuna formalità dai benefici conseguenti al provvedimento emanato sulla base di tali dichiarazioni;
2) di essere iscritto al Corso di Dottorato di ricerca **Mechanical Engineering** ciclo **38_**, corso attivato ai sensi del "*Regolamento dei Corsi di Dottorato di ricerca del Politecnico di Bari"*, emanato con D.R. n.286 del 01.07.2013;
3) di essere pienamente a conoscenza delle disposizioni contenute nel predetto Regolamento in merito alla procedura di deposito, pubblicazione e autoarchiviazione della tesi di dottorato nell'Archivio Istituzionale ad accesso aperto alla letteratura scientifica;
4) di essere consapevole che attraverso l'autoarchiviazione delle tesi nell'Archivio Istituzionale ad accesso aperto alla letteratura scientifica del Politecnico di Bari (IRIS-POLIBA), l'Ateneo archivierà e renderà consultabile in rete (nel rispetto della Policy di Ateneo di cui al D.R. 642 del 13.11.2015) il testo completo della tesi di dottorato, fatta salva la possibilità di sottoscrizione di apposite licenze per le relative condizioni di utilizzo (di cui al sito http://www.creativecommons.it/Licenze), e fatte salve, altresì, le eventuali esigenze di "embargo", legate a strette considerazioni sulla tutelabilità e sfruttamento industriale/commerciale dei contenuti della tesi, da rappresentarsi mediante compilazione e sottoscrizione del modulo in calce (Richiesta di embargo);
5) che la tesi da depositare in IRIS-POLIBA, in formato digitale (PDF/A) sarà del tutto identica a quelle **consegnate**/inviate/da inviarsi ai componenti della commissione per l'esame finale e a qualsiasi altra copia depositata presso gli Uffici del Politecnico di Bari in forma cartacea o digitale, ovvero a quella da discutere in sede di esame finale, a quella da depositare, a cura dell'Ateneo, presso le Biblioteche Nazionali Centrali di Roma e Firenze e presso tutti gli Uffici competenti per legge al momento del deposito stesso, e che di conseguenza va esclusa qualsiasi responsabilità del Politecnico di Bari per quanto riguarda eventuali errori, imprecisioni o omissioni nei contenuti della tesi;
6) che il contenuto e l'organizzazione della tesi è opera originale realizzata dal sottoscritto e non compromette in alcun modo i diritti di terzi, ivi compresi quelli relativi alla sicurezza dei dati personali; che pertanto il Politecnico di Bari ed i suoi funzionari sono in ogni caso esenti da responsabilità di qualsivoglia natura: civile, amministrativa e penale e saranno dal sottoscritto tenuti indenni da qualsiasi richiesta o rivendicazione da parte di terzi;
7) che il contenuto della tesi non infrange in alcun modo il diritto d'Autore né gli obblighi connessi alla salvaguardia di diritti morali od economici di altri autori o di altri aventi diritto, sia per testi, immagini, foto, tabelle, o altre parti di cui la tesi è composta.

Luogo e data **Bari 16/12/2025** Firma DocuSigned by: Roohollah Nazari 6B8ED32AEAE041C...

Il/La sottoscritto, con l'autoarchiviazione della propria tesi di dottorato nell'Archivio Istituzionale ad accesso aperto del Politecnico di Bari (POLIBA-IRIS), pur mantenendo su di essa tutti i diritti d'autore, morali ed economici, ai sensi della normativa vigente (Legge 633/1941 e ss.mm.ii.),

CONCEDE

- al Politecnico di Bari il permesso di trasferire l'opera su qualsiasi supporto e di convertirla in qualsiasi formato al fine di una corretta conservazione nel tempo. Il Politecnico di Bari garantisce che non verrà effettuata alcuna modifica al contenuto e alla struttura dell'opera.
- al Politecnico di Bari la possibilità di riprodurre l'opera in più di una copia per fini di sicurezza, back-up e conservazione.

Luogo e data **Bari 16/12/2025** Firma DocuSigned by: Roohollah Nazari 6B8ED32AEAE041C...

The doctoral scholarship was funded by the European Union - Next Generation EU, Mission 4 Component 1 CUP D93C22000740005

Department of Mechanics, Mathematics and Management
MECHANICAL AND MANAGEMENT ENGINEERING
Ph.D. Program
SSD: ING-IND/14 Mechanical design and machine

Final Dissertation

Adhesion and Friction Effects in Soft Contact Mechanics: From Shell Buckling to Viscoelastic Rolling

by
Roohollah Nazari

Supervisors:

Prof. Michele Ciavarella

Prof. Antonio Papangelo

Coordinator of Ph.D Program:

Prof. Giuseppe Casalino

Course XXXVIII, 01/11/2022 - 31/10/2025

The doctoral scholarship was funded by the European Union - Next Generation EU, Mission 4 Component 1 CUP D93C22000740005

Department of Mechanics, Mathematics and Management
MECHANICAL AND MANAGEMENT ENGINEERING
Ph.D. Program
SSD: ING-IND/14 Mechanical design and machine

Final Dissertation

Adhesion and Friction Effects in Soft Contact Mechanics: From Shell Buckling to Viscoelastic Rolling

by
Roohollah Nazari

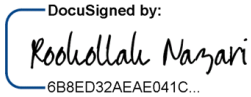

Referees:

Prof. Vladislav Yastrebov

Prof. Ivan Argatov

Supervisors:

Prof. Michele Ciavarella

Prof. Antonio Papangelo

Coordinator of Ph.D Program:

Prof. Giuseppe Casalino

Course XXXVIII, 01/11/2022 - 31/10/2025

Abstract

This thesis presents a comprehensive study of the coupled effects of adhesion and friction in soft and thin-walled structures, with emphasis on how interfacial phenomena control deformation, stability, and energy dissipation. By combining theoretical analysis, numerical modeling, and classical experimental inspiration, the work aims to provide a unified understanding of adhesive contact mechanics in viscoelastic and compliant systems.

The thesis begins with a detailed theoretical framework that reviews the fundamental mechanics of adhesive and frictional contact. Classical models such as those of Hertz, Johnson–Kendall–Roberts (JKR), Derjaguin–Muller–Toporov (DMT), and Maugis are discussed together with their extensions to viscoelastic and rough interfaces. The chapter also highlights the physical role of interface traction, surface energy, and time-dependent viscoelastic behavior, establishing the basis for the subsequent computational studies.

The second part investigates the interplay of adhesion and friction in the mechanical stability of thin spherical shells in contact with rigid substrates. Through finite element simulations, it is shown that interfacial adhesion and friction can suppress the classical buckling instability by redistributing in-plane stresses and providing additional constraint against normal displacement. The results quantify how adhesion enhances the critical load for buckling and how friction introduces tangential stiffness, altering both the buckling mode and the post-buckling path. This study clarifies the dual stabilizing mechanisms of adhesive and frictional interactions and provides scaling relations linking adhesion energy, shell thickness, and curvature.

The following chapter focuses on the sliding of a rigid cylinder on a viscoelastic adhesive substrate. Using a boundary element method (BEM) coupled with a cohesive-zone description based on the Lennard–Jones potential and the Standard Linear Solid model, the analysis explores the effect of the Maugis–Tabor parameter (λ) on the contact asymmetry and frictional dissipation. The results reveal that adhesion modifies the distribution of contact pressure and causes a velocity-dependent transition between adhesive and viscoelastic friction regimes, in agreement with theoretical predictions and experimental observations from polymer systems.

The final part of the thesis is inspired by the classical experiments of Barquins and Roberts on the rolling of rigid cylinders over viscoelastic substrates. A numerical framework is developed to reproduce these experiments, combining adhesive traction and vis-

coelastic dissipation in a cohesive contact formulation. The simulations accurately reproduce the non-monotonic dependence of rolling resistance on velocity observed experimentally. Comparison with the Persson–Brener analytical theory (2010) confirms the validity of the model and elucidates the relative roles of adhesive hysteresis and bulk viscoelastic losses in determining the overall friction. This study bridges experimental findings and theoretical formulations, offering new insight into energy dissipation mechanisms in adhesive rolling contacts.

Collectively, these studies establish a coherent multiscale framework for understanding adhesion–friction coupling in soft matter. By linking continuum mechanics, surface physics, and viscoelastic dissipation, the thesis advances predictive modeling of adhesive contacts across different loading modes—buckling, sliding, and rolling. The findings contribute to the broader understanding of soft tribology and have potential applications in flexible electronics, bio-inspired adhesion, and soft robotic interfaces, where control of adhesion and friction at compliant interfaces is essential.

Contents

List of Figures

Chapter 1

Introduction

1.1 Background and Motivation

Soft materials and thin structures are ubiquitous in both natural and engineered systems, ranging from biological membranes, cells, and tissues to synthetic capsules, elastomers, and flexible devices. Their ability to undergo large deformations and recover their shape under relatively small loads is rooted in their low elastic modulus and high compliance, properties that make them highly sensitive to surface interactions. Among these interactions, adhesion and friction are particularly significant, as they dictate contact mechanics, stability, and energy dissipation across multiple length scales [1–4]. Understanding how these interfacial phenomena interact with the intrinsic viscoelasticity of soft materials is essential for predicting their behavior in applications ranging from soft robotics and bioinspired adhesion to flexible electronics and tribological systems.

Thin elastic shells represent one of the most classical yet complex systems in solid mechanics, capable of exhibiting large deformations and geometric instabilities such as snap-through or buckling. While these phenomena have been extensively studied in the context of structural mechanics [5–7], the influence of surface adhesion and interfacial friction on their stability remains comparatively unexplored. Recent investigations have shown that contact interactions can significantly alter the load–displacement response of thin shells, either stabilizing or destabilizing them depending on the interface conditions [8, 9]. In particular, the phenomenon of snap-back instability—where the system transitions abruptly between equilibrium states—is of central interest in the design of bistable structures and soft actuators. However, most previous studies neglect interfacial adhesion or treat it only under small deformation assumptions, leaving open the question of whether adhesion and friction can be tuned to control or suppress buckling under large strains.

In addition to static instabilities, dynamic contact phenomena in soft materials are profoundly influenced by viscoelastic effects. When a soft viscoelastic body slides or

rolls on a rigid substrate, the interplay between adhesion, deformation rate, and hysteretic dissipation produces highly nonlinear frictional behavior. Classical experiments by Grosch [10], Schallamach [11, 12], and Barquins and Roberts [13] revealed that the coefficient of friction of rubber-like materials follows a characteristic bell-shaped dependence on sliding velocity, reflecting a balance between adhesive and viscoelastic energy losses. Theoretical models based on linear viscoelasticity [14–16] and modern numerical simulations [17, 18] have provided valuable insights, yet a unified framework that consistently couples adhesion, friction, and viscoelastic dissipation across different loading regimes is still lacking.

The present work addresses these gaps by developing a comprehensive study of soft contact mechanics that spans both structural instability and tribological regimes. The first part of the research focuses on the buckling behavior of thin spherical shells in adhesive and frictional contact with rigid surfaces. Through Finite Element Method (FEM) simulations supported by experimental validation, it is shown that adhesion and friction can synergistically delay or completely suppress snap-through instability. The second part investigates the sliding friction of a viscoelastic cylinder in adhesive contact, using a Boundary Element Method (BEM) formulation to quantify the respective contributions of adhesive and viscoelastic dissipation as functions of the Maugis–Tabor parameter and sliding velocity. The final part extends the analysis to rolling friction, where viscoelastic bulk losses and adhesive hysteresis at the contact edges jointly determine the total rolling resistance. Together, these studies form a coherent picture of how adhesion, friction, and viscoelasticity interact to govern the mechanics of soft interfaces.

By bridging shell mechanics and soft tribology, this thesis contributes to a more unified understanding of surface-dominated phenomena in deformable materials. Beyond advancing theoretical contact mechanics, the findings have practical implications for designing materials and devices where interfacial control is critical—such as microstructured adhesives, soft robotic grippers, biomimetic sensors, and energy-dissipating coatings.

1.2 Structure of the Thesis

This thesis is organized into seven chapters, each building progressively toward a comprehensive understanding of adhesion and friction effects in soft contact mechanics. Following this introduction, Chapter 2 presents a detailed literature review on adhesion, friction, and viscoelasticity, summarizing the classical theories of adhesive contact and recent advances in soft interface modeling. Chapter 3 investigates the nonlinear buckling of thin elastic shells in adhesive and frictional contact with rigid substrates, combining finite element analyses with experiments to identify critical adhesion thresholds for stability. Chapter 4 explores the sliding friction behavior of viscoelastic contacts through a boundary element approach, highlighting the transition between adhesive and viscoelas-

tic dissipation regimes. Chapter 5 extends the study to rolling contact, analyzing how viscoelasticity and adhesive hysteresis contribute to the overall rolling resistance. Chapter 6 integrates and compares the results from the previous chapters, emphasizing the interconnections between structural instability and frictional energy dissipation. Finally, Chapter 7 concludes the thesis, summarizing the main findings, discussing their implications, and outlining potential directions for future research.

Overall, this thesis provides a consistent framework that connects static and dynamic aspects of soft contact mechanics, revealing how adhesion and friction can be harnessed to control deformation, stability, and dissipation in soft materials.

Chapter 2

Literature Review

2.1 Introduction to Adhesion

Adhesion refers to the attractive forces that hold two surfaces or particles together, even in the presence of mechanical stresses that tend to separate them [19]. These adhesive forces are crucial in numerous contexts—ranging from microscale phenomena such as cell adhesion, bacterial aggregation, and drug delivery vesicles, to macroscale examples like contact lens attachment and soft robotics.

Adhesive interactions can arise from multiple underlying mechanisms, including mechanical interlocking, chemical bonding,electrostatic attraction and dispersive forces:

- **Mechanical adhesion** (or interlocking) occurs when adhesives penetrate surface pores or irregularities and physically "lock" the surfaces together. A practical example includes rubber bonded to textiles or paper.
- **Chemical adhesion** results from the formation of covalent, ionic, or hydrogen bonds at the interface between two materials. This is typical of many glues and structural adhesives, where chemical reactions form strong, durable joints [20].
- **Electrostatic adhesion** arises from the attraction between oppositely charged surfaces or from charge redistribution at the interface of contacting materials. When two materials with different electron affinities come into contact and then separate, an imbalance of electric charge—known as *triboelectric charging*—can generate adhesive forces that hold the surfaces together. This mechanism is particularly relevant in applications such as electroadhesive grippers used in robotics, where a controlled electric field enables objects to be picked up and released without mechanical fasteners or chemical adhesives. Electrostatic adhesion is also observed in everyday phenomena such as dust particles adhering to plastic surfaces or fabrics clinging after drying [21].

- **Dispersive adhesion** is attributed to weak van der Waals interactions between molecules. While these forces are individually weak, their collective effect can generate substantial adhesion—most notably demonstrated in the gecko's ability to climb walls and ceilings. As illustrated in Figure 2.1, geckos utilize a sophisticated hierarchical structure in their toe pads that enables strong, reversible, and residue-free adhesion. Their foot hairs are directionally aligned, self-cleaning, and effective across diverse surface conditions, including underwater and vacuum environments [22].

Inspired by this biomimetic adhesion mechanism, researchers have developed a variety of synthetic adhesive systems that replicate gecko-like performance. In real-world applications, adhesion is often governed by a combination of these mechanisms, making it a complex and highly interdisciplinary topic of study.

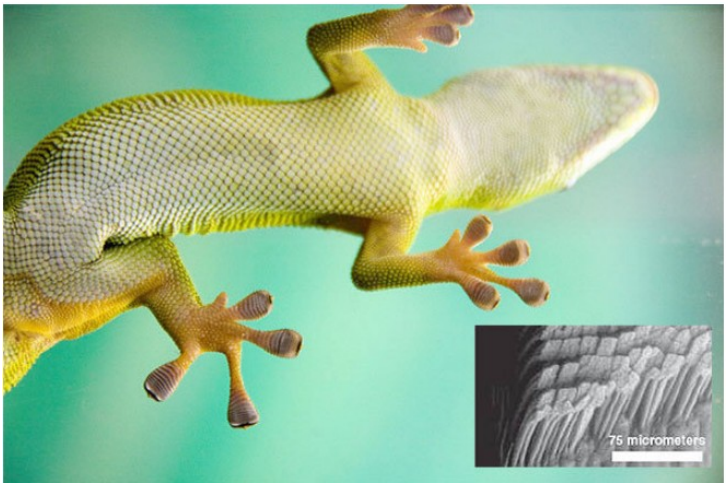

Figure 2.1: Hierarchical microstructure of gecko foot responsible for van der Waals-based adhesion [22].

The adhesive interaction between two contacting bodies ultimately stems from atomic-scale interatomic forces, primarily governed by weak and long-range van der Waals interactions.

Although van der Waals interactions are among the weakest forces between atoms and molecules, their collective effect across many atomic pairs can result in significant adhesive forces between macroscopic solids. These interactions are especially critical in soft materials, thin shells, and bio-inspired structures where surface forces dominate bulk behavior.

This thesis focuses on van der Waals interactions that contribute to adhesive contact. Several types of van der Waals potentials are introduced and analyzed, starting from the atom–atom level and extending to atom–surface and surface–surface configurations through integration techniques.

Additionally, a number of classical adhesive contact models are reviewed, including the assumptions and simplifications they employ. These models provide critical tools for understanding adhesion in compliant structures and are widely used in the analysis of contact mechanics in thin shells, soft interfaces, and nanocomposites.

2.2 Van der Waals Interactions Between Atoms

This section introduces van der Waals interactions between particles, such as atoms, molecules, and ions. Unlike other types of intermolecular forces that depend on specific molecular characteristics, van der Waals forces are universally present, occurring between all particles regardless of their chemical nature.

In contrast to covalent or ionic bonds—which involve the sharing or transfer of electrons— van der Waals interactions originate from correlated fluctuations in the polarization of adjacent particles [23]. Though individually weak, these forces can collectively exert significant influence, particularly in nanoscale systems.

Attractive intermolecular interactions can be divided into four main types: dipole–dipole interactions (known as Keesom forces), ion–dipole interactions, dipole–induced dipole interactions (Debye forces), and instantaneous dipole–induced dipole interactions (London dispersion forces). The combination of Keesom, Debye, and London dispersion forces is commonly referred to as the van der Waals attraction.

The total long-range van der Waals interaction between two particles can be expressed as the sum of these components:

$$U_{\mathrm{VDW}}(h) = U_{\mathrm{Keesom}} + U_{\mathrm{Debye}} + U_{\mathrm{London}} = -\frac{C_{\mathrm{VDW}}}{h^6} \tag{2.1}$$

where h is the separation distance between the particles, and C_{VDW} is a constant that depends on their polarizabilities and interaction strengths.

2.2.1 Keesom Interactions

Dipole–dipole interactions arise between molecules with permanent dipole moments. These electrostatic interactions cause molecules to orient themselves such that the positive end of one dipole is attracted to the negative end of another, leading to a reduction in the system's potential energy. A typical example is hydrogen chloride (HCl), where dipoles align due to these forces.

Keesom interactions specifically describe the attractive forces between permanent dipoles, averaged over all possible rotational orientations according to Boltzmann statistics. These interactions are temperature-dependent and diminish with increasing intermolecular distance.

The potential energy of the Keesom interaction as a function of separation distance h is expressed as [23]:

$$U_{\text{Keesom}}(h) = -\left(\frac{u_1^2 u_2^2}{3(4\pi\varepsilon_0\varepsilon)^2 kT}\right)\frac{1}{h^6} \tag{2.2}$$

where u_1 and u_2 are the dipole moments of the interacting molecules, ε_0 is the vacuum permittivity, ε is the relative permittivity of the medium, k is the Boltzmann constant, T is the absolute temperature, and h is the intermolecular separation distance.

Keesom interactions constitute one of the three primary components of van der Waals forces, playing a significant role in long-range molecular attractions.

2.2.2 Debye Interactions

Debye interactions describe the attractive force between a molecule with a permanent dipole and another molecule that is non-polar but becomes temporarily polarized due to the influence of the dipole field. Unlike ion–dipole interactions, the electric field responsible for polarization in this case originates from a permanent dipole rather than a charged species.

These dipole–induced dipole interactions are generally weaker than dipole–dipole (Keesom) interactions but are stronger than London dispersion forces. The potential energy of the Debye interaction as a function of the separation distance h is given by [23]:

$$U_{\text{Debye}}(h) = -\left(\frac{u_1^2\alpha_2 + u_2^2\alpha_1}{(4\pi\varepsilon_0\varepsilon)^2}\right)\frac{1}{h^6} \tag{2.3}$$

In this expression, u represents the permanent dipole moment, α_1 and α_2 are the polarizabilities of the interacting species, ε_0 is the vacuum permittivity, ε is the relative permittivity of the medium, and h denotes the intermolecular distance.

Debye interactions contribute significantly to van der Waals forces, especially in heterogeneous systems involving both polar and non-polar components.

2.2.3 London Dispersion Interactions

London dispersion forces are temporary attractive interactions that emerge when fluctuations in the electron distribution within atoms or molecules lead to the formation of instantaneous dipoles. These short-lived dipoles can induce corresponding dipoles in neighboring particles, resulting in a net attractive force. Dispersion forces are present in all atoms and molecules, irrespective of their polarity.

The classical expression derived by London for the dispersion interaction energy between two identical atoms or molecules is given by [23]:

$$U_{\text{London}}(h) = -\left(\frac{3\alpha_1\alpha_2 I_1 I_2}{2(4\pi\varepsilon_0)^2(I_1+I_2)}\right)\frac{1}{h^6} \tag{2.4}$$

In this equation, α_1 and α_2 are the polarizabilities, I_1 and I_2 are the first ionization potentials of the interacting atoms or molecules, ε_0 is the vacuum permittivity, and h represents the distance between the particles.

Similar to Keesom and Debye interactions, London dispersion forces exhibit a $1/h^6$ dependence on intermolecular separation, highlighting their long-range but relatively weak nature.

2.2.4 Lennard–Jones potential

The Lennard–Jones (LJ) potential, introduced by John Lennard-Jones in 1924, is a simple model for the interaction between two neutral atoms or molecules. It captures both the long-range van der Waals attraction and the short-range repulsion due to electron-cloud overlap governed by the Pauli exclusion principle [24]. Its most common form is

$$U_{\text{LJ}}(h) = 4U_0\left[\left(\frac{h_0}{h}\right)^{12} - \left(\frac{h_0}{h}\right)^{6}\right], \tag{2.5}$$

where U_0 is the well depth (minimum potential energy), h_0 is the separation at which the potential crosses zero, and h is the interatomic distance. The potential attains its minimum at $h = 2^{1/6}h_0$ (since $\mathrm{d}U_{\text{LJ}}/\mathrm{d}h = 0$ there). The h^{-12} term represents short-range Pauli repulsion from overlapping orbitals, whereas the h^{-6} term provides the attractive van der Waals tail. Because of its simplicity, the LJ potential is widely used in molecular simulations.

2.3 Van der Waals interactions between surfaces and solids

In this section we examine long-range van der Waals interactions between solids and surfaces. Starting from the pair interaction potential derived in the previous section, one can integrate over all atoms in a body to obtain an atom–surface potential, and then perform a second integration over the other body to arrive at the surface–surface interaction. Following this approach, de Boer derived the potential between two parallel half-spaces by integrating the van der Waals pair potential [25]. Because the geometry influences the result, different surface shapes lead to different functional forms; representative cases are illustrated in Figure 2.2. If additional long-range interactions—such as electrostatic forces or steric (e.g., polymer-mediated) effects in liquids—are present, the overall potential becomes correspondingly more complex.

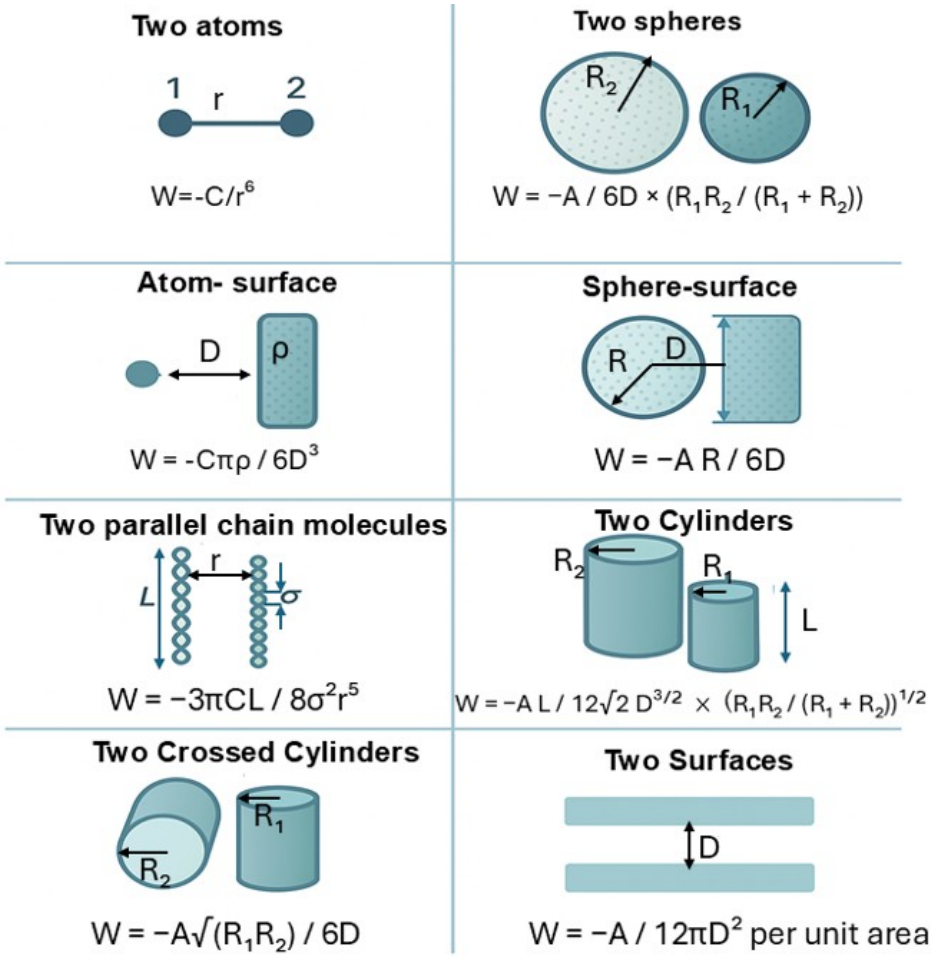

Figure 2.2: Van der Waals interaction free energies between bodies for different geometries, in which A is Hamaker constant, C is the coefficient in the atom-atom potential [23].

2.4 Surface Energy and classic adhesive models

2.4.1 Surface energy

For the intermolecular potentials discussed above, the depth of the energy minimum is often identified with the work of adhesion. The work of adhesion between two media (1 and 2), denoted W_{12}, is the reversible change in free energy per unit area required to separate their interface from contact to infinite separation (units: $\mathrm{J\,m^{-2}}$).

Creating one unit area of free surface of material 1 is equivalent to separating two half-areas of material 1 from contact. Hence the surface energy of material 1 equals one half of its work of cohesion:

$$\gamma_1 = \tfrac{1}{2} W_{11}. \tag{2.6}$$

An analogous relation holds for material 2, $\gamma_2 = \frac{1}{2} W_{22}$.

When two media are brought into contact, the free-energy change associated with

increasing their interfacial area by one unit defines the interfacial (surface) energy γ_{12}. Conceptually, this process can be viewed as: (i) create one unit area of each free surface (cost $\gamma_1 + \gamma_2$), then (ii) form the interface, which returns the work of adhesion W_{12}. Combining these steps yields the Dupré relation:

$$\gamma_{12} \;=\; \gamma_1 + \gamma_2 - W_{12} \;=\; \tfrac{1}{2}W_{11} + \tfrac{1}{2}W_{22} - W_{12}. \tag{2.7}$$

Here W_{11} and W_{22} denote the cohesive works for media 1 and 2, respectively, while W_{12} is the adhesive work between them[26, 27] .

2.4.2 Classical adhesion models

Although the original derivations consider only van der Waals attraction, the same integration can be performed using the Lennard–Jones potential, as shown by Maugis [28]. The general form of the potential between two adhering surfaces is expressed as:

$$U_{LJ}(h) = C_s \left[\left(\frac{h_0}{h} \right)^{a_1} - \left(\frac{h_0}{h} \right)^{a_2} \right] \tag{2.8}$$

where the constant C_s and the exponents a_1 and a_2 depend on the material properties, surface geometries, and the surrounding environment.

The corresponding disjoining pressure is obtained by differentiating Equation 2.8 with respect to h:

$$p(h) = -\frac{dU_{LJ}(h)}{dh} = C_s' \left[\left(\frac{h_0}{h} \right)^{a_1+1} - \left(\frac{h_0}{h} \right)^{a_2+1} \right] \tag{2.9}$$

Figure 2.3 schematically illustrates the Lennard–Jones potential as a function of the separation distance h, together with the associated disjoining pressure. At short distances, the pressure becomes negative, corresponding to repulsion, while at larger separations it turns attractive and decays with increasing distance. The equilibrium position is reached at $h = h_0$. Several classical solid adhesion models are introduced by adopting different assumptions based on this potential.

2.4.2.1 Hertz Theory

The classical Hertz theory [29] addresses the problem of a rigid sphere indenting an elastic half-space, or equivalently, the contact between two elastic spheres in the absence of adhesion. Hertz provided the stress distribution within the contact area and established the relations among the main measurable quantities: the applied compressive load F_H, the approach distance d_H, and the contact radius a_H. These are given by:

$$a_H^3 = \frac{3F_H R}{K} \tag{2.10}$$

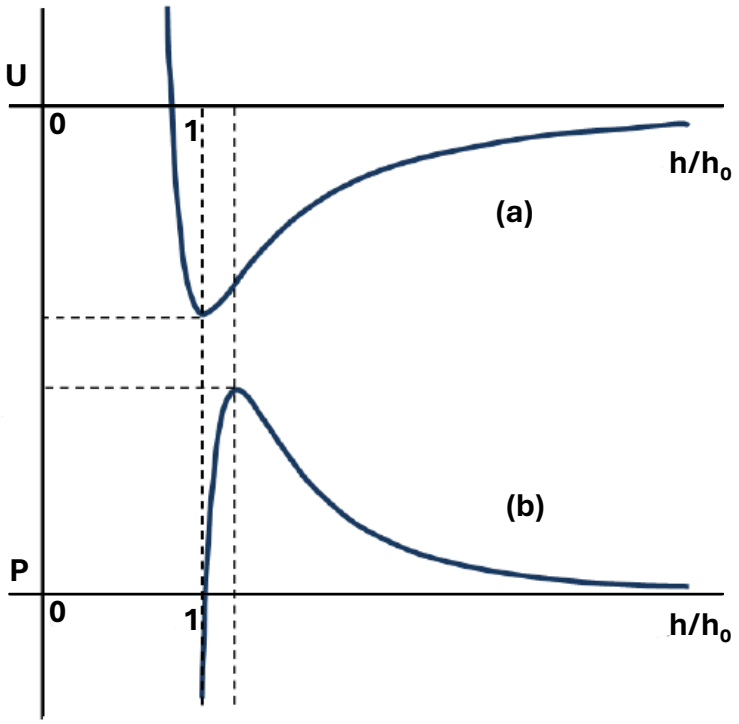

Figure 2.3: Lennard-Jones potential as a function of distance, with (a) energy and (b) corresponding disjoining pressure.

and

$$d_H = \frac{a_H^2}{R} = \left(\frac{9F_H^2}{K^2R}\right)^{1/3}, \tag{2.11}$$

where R is the effective radius of curvature, and K is the effective elastic modulus defined as:

$$\frac{1}{K} = \frac{3}{4}\left(\frac{1-v_1^2}{E_1} + \frac{1-v_2^2}{E_2}\right), \tag{2.12}$$

with E_i and v_i $(i = 1, 2)$ denoting the Young's modulus and Poisson's ratio of the two materials, respectively.

2.4.2.2 Johnson-Kendall-Roberts (JKR) Theory

In the region where two surfaces come into contact, the separation between them is often on the order of atomic dimensions. At this scale, adhesive forces resulting from long-range intermolecular interactions become significant. To account for these effects, Johnson, Kendall, and Roberts developed a model that incorporates surface adhesion by representing it as an idealized force of infinite magnitude and zero range. This model, now known as the JKR theory [30], demonstrated that a finite contact area exists even in the absence of an external load, and that a "pull-off" force is required to detach the

sphere from the surface once contact has been established.

The influence of surface energy leads to an infinite tensile stress at the edge of the contact zone. The equilibrium relationship between the contact radius a_J and the applied load F_J is expressed as:

$$a_J^3 = \frac{3R}{4K}\left(F_J + 3\pi\gamma R + \sqrt{6\pi\gamma R F_J + (3\pi\gamma R)^2}\right) \tag{2.13}$$

Here, γ is the work of adhesion [J/m^2], which represents the energy required per unit area to create a new surface.

A comparison between JKR and Hertzian contact theory is presented in Figure 2.4. Importantly, even at the critical pull-off point, the contact radius remains non-zero, and the corresponding pull-off force can be expressed as:

$$F_{\min} = -\frac{3}{2}\pi\gamma R \tag{2.14}$$

At this condition, the system also exhibits a minimum contact radius given by:

$$a_{\min}^3 = \frac{3\pi\gamma R^2}{2K} \tag{2.15}$$

This result highlights that while the critical pull-off force is independent of Young's modulus E, the minimum contact radius depends on the elastic properties of the materials through the parameter K.

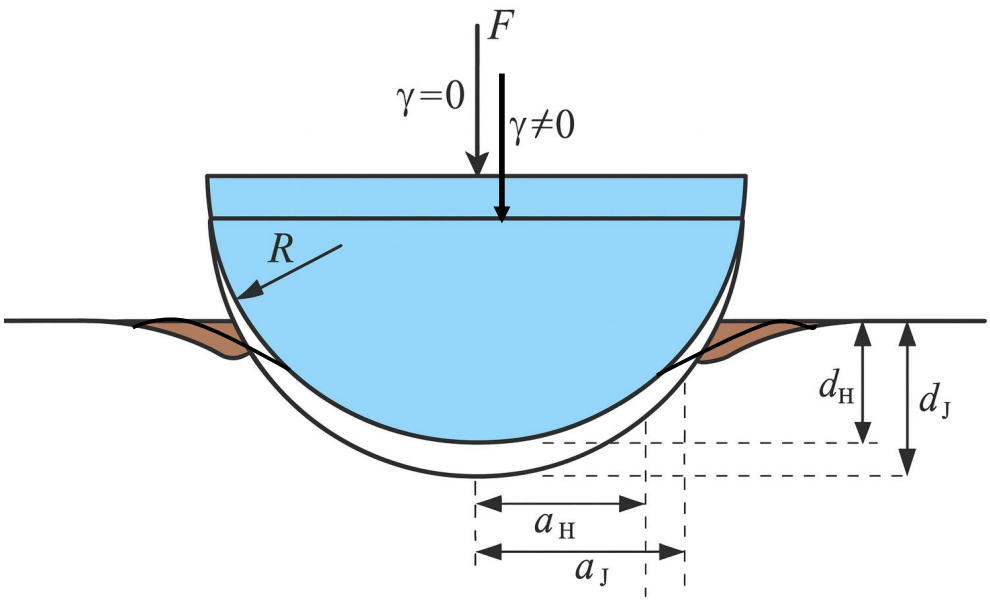

Figure 2.4: Comparison between a Herzian contact and a JKR contact under same load.

2.4.2.3 Derjaguin-Muller-Toporov (DMT) Theory

An alternative adhesion model, developed by Derjaguin, Muller, and Toporov (DMT), considers the case of an infinite range of intersurface forces and predicts a markedly different mechanical response [31]. In this theory, the adhesive forces act in a narrow annular region surrounding the contact area but do not significantly deform the contact profile, which remains essentially Hertzian.

The resulting pull-off force predicted by the DMT model differs from that obtained using the JKR theory and is given by:

$$F_c = -2\pi\gamma R \tag{2.16}$$

2.4.2.4 Maugis' Cohesive Zone Theory

To reconcile the differences between the JKR and DMT models, Tabor [32] highlighted that the primary limitation of the DMT theory is its neglect of surface deformations caused by adhesive forces around the contact area, while the main shortcoming of the JKR theory is its omission of adhesive forces acting outside the contact zone. Building on this observation, Tabor and later Maugis [33] applied the Dugdale cohesive zone model to develop a unified framework describing the transition between JKR and DMT behavior for cases involving a finite adhesive force magnitude p^* and a finite interaction range h^*.

The transition between the two regimes is characterized by the Tabor parameter, defined as:

$$\lambda = \left(\frac{R\gamma^2}{Eh^{*3}}\right)^{1/3} \tag{2.17}$$

where R is the effective radius, γ is the work of adhesion, E is the elastic modulus, and h^* is the characteristic range of adhesive forces. The JKR model is applicable when $\lambda > 3$, while the DMT model is valid when $\lambda < 0.25$. The relationship between the contact radius and the applied load across the JKR-DMT transition is illustrated in Figure 2.5.

The transition can also be represented in terms of the disjoining pressure p^* and the intersurface separation h^*, as shown in Figure 2.6. Although the Lennard-Jones potential (solid line) accurately describes the interfacial interactions, its mathematical complexity makes it difficult to apply to practical contact problems. To address this, the Dugdale cohesive zone model simplifies the description by assuming that adhesive forces are constant within the cohesive zone ($0 < h \leq h^*$) and zero beyond it ($h > h^*$).

In this model, the product of the adhesive force magnitude and the cohesive zone range equals the work of adhesion, and this quantity is matched to the area under the Lennard-Jones potential curve. When the intersurface force is long-ranged with a low magnitude,

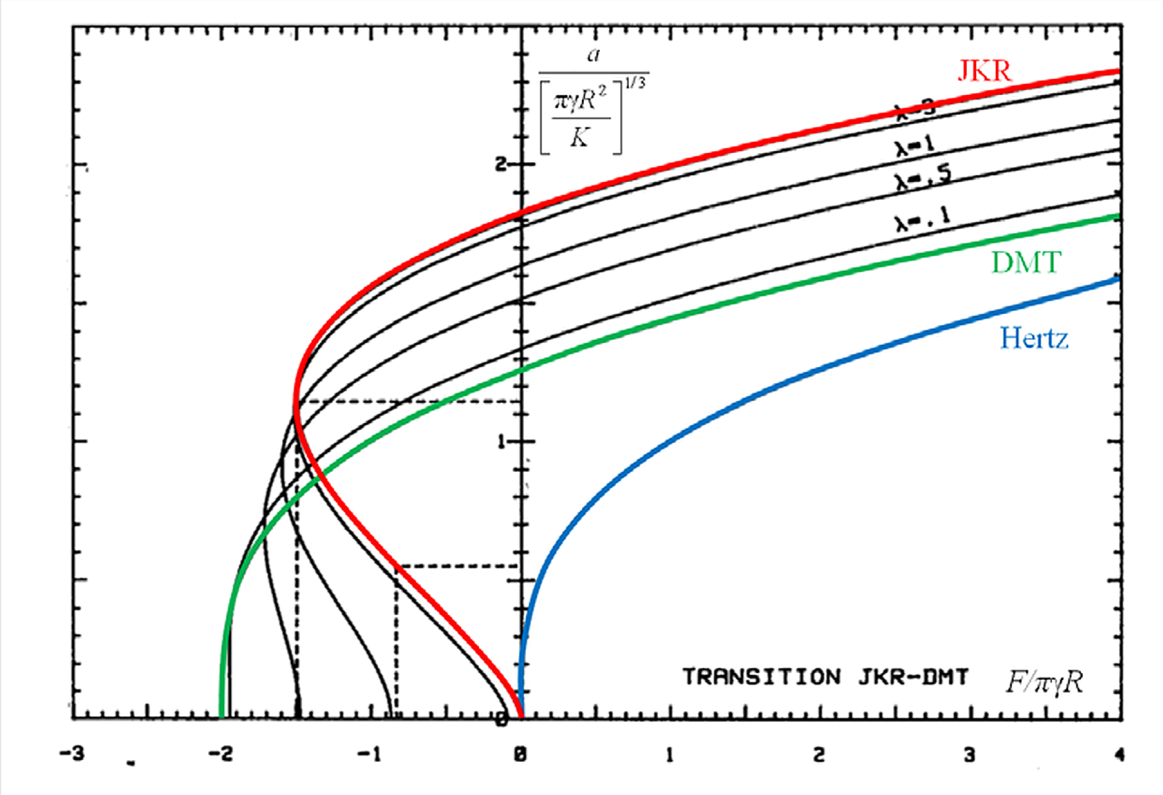

Figure 2.5: Relation between radius of contact and applied load for various λ [28] .

the contact behavior approaches the DMT limit. Conversely, when the interaction range is short and the force magnitude is very high, the JKR model is more appropriate. Both limiting cases are depicted in Figure 2.6.

2.5 Viscoelastic Materials: Fundamentals and Characteristics

Viscoelastic materials, such as polymers, are widely used in a variety of engineering and scientific fields due to their unique combination of properties, including low friction, low weight, minimal noise generation, cost-effectiveness, dimensional stability, biocompatibility, and long-term load-bearing capacity. Consequently, viscoelastic contact phenomena are encountered in numerous applications, such as the optimization of chocolate texture in the food industry [34], the interaction between human skin and surgical tools in biomedical engineering [35], tire–road contact in the automotive sector [36], and the flow of basaltic lava in geothermal systems [37].

A thorough understanding of the interfacial mechanics of viscoelastic materials is essential for the design and analysis of both engineered systems and natural processes. Important aspects to consider include time-dependent deformation, lubrication behaviour,

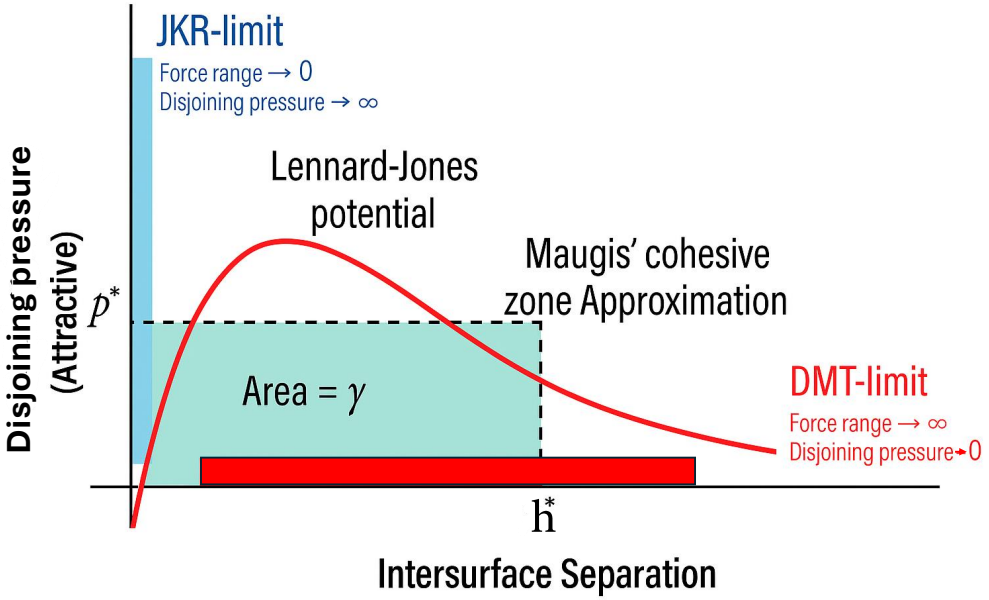

Figure 2.6: A schematic drawing of Lennard-Jones potential, JKR, DMT, Maugis.

energy dissipation, and the effects of frictional heating. For instance, the service life of a polymer-based knee prosthesis depends strongly on its time-dependent mechanical response under various loading and lubrication conditions associated with human activity [38]. A deeper understanding of these contact phenomena enables the development of more efficient products, reduced energy consumption, and improved performance. Increasing performance demands, the need to reduce material usage, and the drive to minimise environmental impact continue to motivate the development of analytical and numerical tools for modelling viscoelastic behaviour.

This section introduces key concepts, terminology, and fundamental relationships used to describe the contact mechanics of viscoelastic materials. It also briefly reviews the theory of linear viscoelasticity and the Boltzmann superposition principle, based on well-established references in the field [39–44].

2.5.1 Characteristics of Viscoelastic Materials

All materials deform when subjected to external loads. An ideal elastic solid follows Hooke's law, which defines a linear relationship between stress and strain. Such a material deforms instantaneously when loaded and returns completely to its original configuration upon unloading. In contrast, a Newtonian fluid undergoes continuous and irreversible deformation under shear stress, with stress being proportional to strain rate.

Viscoelastic materials exhibit behaviour that combines these two responses. They deform instantaneously like elastic solids but also undergo time-dependent deformation due to viscous effects. In linear viscoelastic materials, the relationship between stress and

strain satisfies the principle of superposition. However, unlike purely elastic solids, the stress state at a given time does not depend solely on the instantaneous strain but rather on the entire deformation history. This behaviour is typically described through time-dependent constitutive functions such as the relaxation modulus or creep compliance.

Typical examples of materials exhibiting linear viscoelastic behaviour under moderate deformation include elastomers, polymers, gels, bituminous materials, and biological soft tissues. Under small and short-duration loads, some materials may be approximated as elastic, whereas for larger deformations or long-term loading conditions, a complete viscoelastic formulation is necessary for accurate prediction.

The response of viscoelastic materials is strongly influenced by loading rate, time, and temperature. Useful experimental characterisations include creep tests, stress relaxation tests, cyclic loading protocols, and dynamic mechanical analysis. In the context of linear viscoelasticity, deformation is recoverable after unloading; permanent or residual strains occur only when additional mechanisms such as plasticity, material damage, or non-linear flow are present.

Finally, three fundamental manifestations of viscoelasticity—creep, stress relaxation, and hysteresis—are central to describing the time-dependent response of such materials. These phenomena will be discussed individually in the following sections.

2.5.1.1 Creep

Creep refers to the time-dependent increase in strain under a constant load (Figure 2.7). When a load is first applied, an instantaneous elastic deformation occurs. This is followed by a gradual, time-dependent deformation known as creep strain, which typically increases at a decreasing rate until reaching a steady-state value. Upon unloading, the material undergoes immediate elastic recovery followed by slower anelastic recovery. Some permanent deformation may remain due to viscous flow. Creep behaviour provides valuable insight into a material's dimensional stability and long-term load-bearing performance.

2.5.1.2 Stress Relaxation

Stress relaxation is the phenomenon in which the internal stress of a viscoelastic material gradually decreases with time under constant strain and temperature (Figure 2.8). This occurs due to molecular or microstructural rearrangements that allow stress to dissipate even when deformation remains fixed. Stress relaxation behaviour is particularly significant in applications requiring long-term dimensional or mechanical stability, such as biomedical implants and structural components.

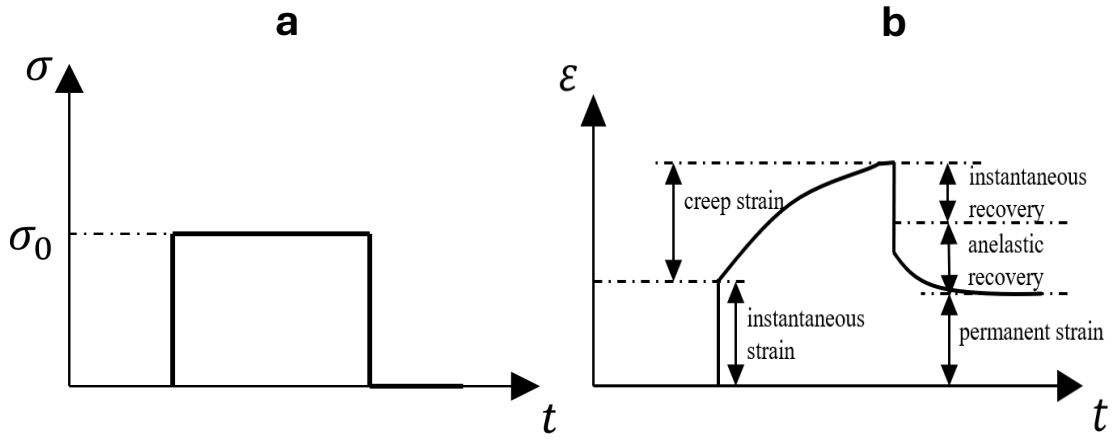

Figure 2.7: Input and output in a creep test for viscoelastic materials: (a) load input and (b) response of strain with time.

2.5.1.3 Hysteresis

Hysteresis refers to the time-dependent lag between changes in strain and changes in stress in a viscoelastic material subjected to cyclic loading at a constant temperature. This behaviour occurs because viscoelastic materials simultaneously exhibit elastic (solid-like) and viscous (fluid-like) responses, resulting in partial energy dissipation during each loading cycle. A typical hysteresis loop is illustrated in Figure 2.9.

Consider a viscoelastic material subjected to a sinusoidal stress input of the form:

$$\sigma(t) = \hat{\sigma}\sin(\omega t) \tag{2.18}$$

For an ideal elastic material, the strain response is perfectly in phase with the applied stress and is expressed as:

$$\varepsilon(t) = \hat{\varepsilon}\sin(\omega t) \tag{2.19}$$

In this case, all the mechanical work performed by the external load during deformation is stored as elastic potential energy and fully recovered during unloading. Therefore, no energy is dissipated as heat.

For an ideal viscous material, the strain response lags the stress by a phase angle of $\pi/2$, given by:

$$\varepsilon(t) = \hat{\varepsilon}\sin\left(\omega t - \frac{\pi}{2}\right) \tag{2.20}$$

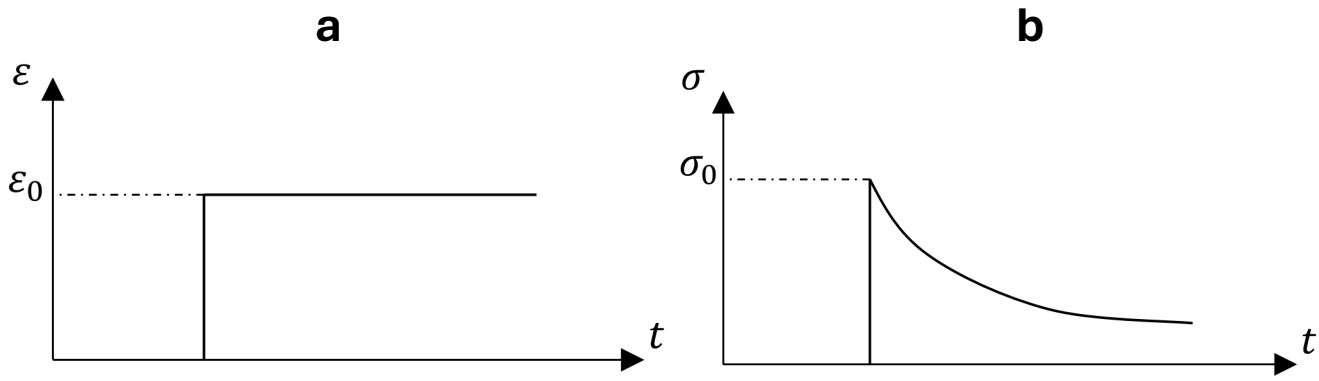

Figure 2.8: Input and output in a stress relaxation test for viscoelastic materials: (a) strain input and (b) response of stress with time.

This phase difference indicates that the input mechanical energy is entirely converted into heat, and no elastic energy is recovered.

In contrast, a viscoelastic material exhibits an intermediate behaviour, with the strain response lagging behind the applied stress by a phase angle χ such that $0 < \chi < \frac{\pi}{2}$:

$$\varepsilon(t) = \hat{\varepsilon} \sin(\omega t - \chi) \tag{2.21}$$

The phase shift χ represents the energy dissipation due to the viscous component of the material's response. Because of this lag, the stress–strain curve over one loading cycle forms a closed loop, known as the hysteresis loop, where the area enclosed by the loop corresponds to the mechanical energy lost per cycle, typically converted into heat.

Moreover, as illustrated in Figure 2.9, the area under the unloading curve is smaller than that under the loading curve, indicating irreversible energy loss. This hysteretic energy dissipation is a critical factor in applications where damping, vibration absorption, and energy dissipation are desired, such as in polymer bearings, soft tissue mechanics, and shock-absorbing systems.

2.5.2 Constitutive Law and Relevant Rheological Models

The theory of small-strain linear viscoelasticity forms the fundamental basis for modelling the mechanical behaviour of viscoelastic materials. Although this framework originates

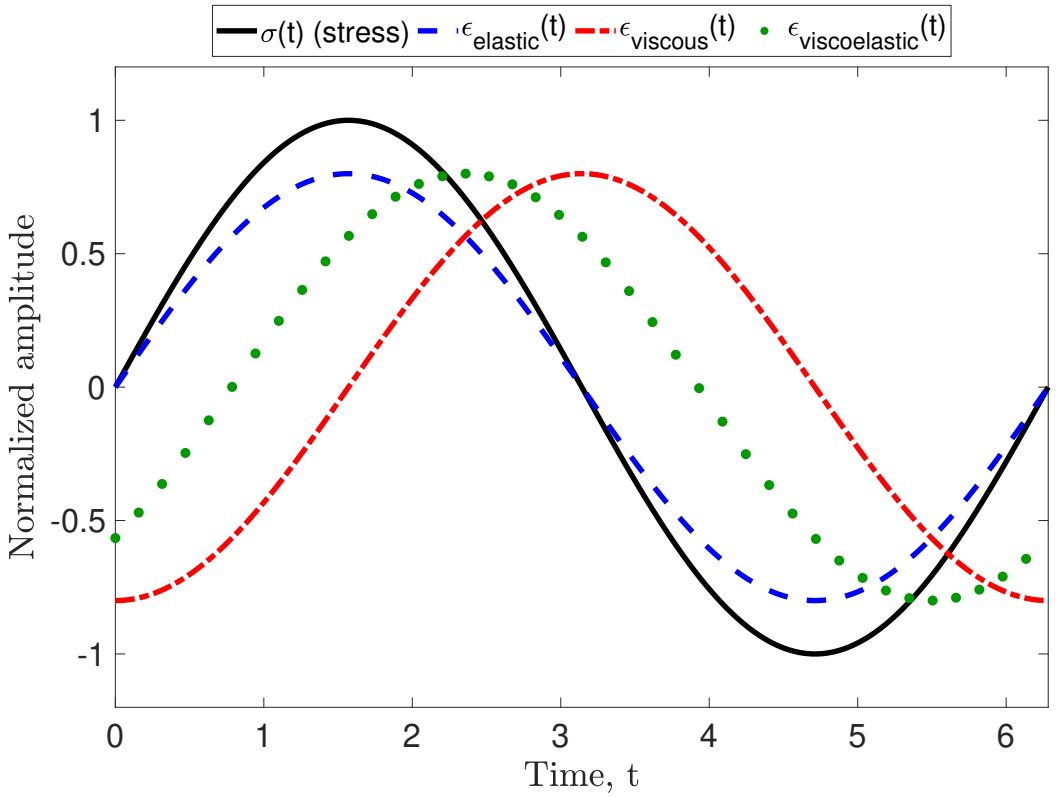

Figure 2.9: The strain response to sinusoidal stress (black line) of different materials: elastic (blue line),viscous (red line) and viscoelastic (green scatter).

from linear elasticity, it remains a valuable starting point even in more complex cases, such as nonlinear viscoelastic contact problems. For materials exhibiting a linear stress–strain relationship, the response of stress to a sequence of strain inputs (and vice versa) is cumulative, allowing the total response to be represented as the sum of the individual contributions.

Two fundamental time-dependent material properties are widely used to characterise the constitutive behaviour of linear viscoelastic materials: the creep compliance, $\Phi(t)$, and the relaxation modulus, $\Psi(t)$. The creep compliance describes the time-dependent strain response to a unit change in stress, thereby representing the creep behaviour of the material. Conversely, the relaxation modulus characterises the time-dependent stress response to a unit change in strain, capturing the phenomenon of stress relaxation. These two functions are crucial in analysing the transient contact response of viscoelastic materials.

Boltzmann Superposition Principle

The constitutive behaviour of linear viscoelastic materials is often described using the Boltzmann superposition principle, which states that the total response of a material to

multiple excitations is the sum of the individual responses to each excitation considered independently.

For example, the stress $\sigma_1(t)$ at time t resulting from a strain ε_1 applied at an earlier time t_1^0 can be written as:

$$\sigma_1(t) = \Psi(t - t_1^0)\varepsilon_1 H(t - t_1^0) \tag{2.22}$$

where $H(t)$ is the Heaviside step function. Similarly, the stress $\sigma_2(t)$ due to another strain ε_2 applied at time t_2^0 is:

$$\sigma_2(t) = \Psi(t - t_2^0)\varepsilon_2 H(t - t_2^0) \tag{2.23}$$

For a continuous distribution of strain increments, the total stress response becomes:

$$\sigma(t) = \int_{0^-}^{t} \Psi(t - t_0) \frac{d\varepsilon(t_0)}{dt_0}\, dt_0 \tag{2.24}$$

Similarly, the strain response to a stress history can be expressed as:

$$\varepsilon(t) = \int_{0^-}^{t} \Phi(t - t_0) \frac{d\sigma(t_0)}{dt_0}\, dt_0 \tag{2.25}$$

Relationship Between Creep Compliance and Relaxation Modulus

In contrast to purely elastic materials, where compliance and modulus are reciprocals, the relationship between creep compliance and relaxation modulus in linear viscoelastic materials is more complex. In the time domain, their relationship is expressed as:

$$\int_{0}^{t} \Phi(t - t_0)\Psi(t_0)\, dt_0 = t \tag{2.26}$$

In the Laplace transform domain, however, the relationship simplifies to:

$$\Phi(s)\Psi(s) = \frac{1}{s^2} \tag{2.27}$$

where $\Phi(s)$ and $\Psi(s)$ are the Laplace transforms of $\Phi(t)$ and $\Psi(t)$, respectively, and $s = a + jb$ is the Laplace complex frequency parameter.

Rheological Models

The time-dependent mechanical behaviour of viscoelastic materials is often modelled using rheological models, which consist of ideal mechanical elements: springs (representing

perfectly elastic solids, where stress is proportional to strain) and dashpots (representing Newtonian fluids, where stress is proportional to strain rate).

When a spring and a dashpot are connected in series (Figure 2.10(a)), the resulting model is known as the Maxwell model. This model effectively captures the stress relaxation behaviour of viscoelastic materials but cannot describe creep and recovery phenomena. In contrast, when the two elements are arranged in parallel (Figure 2.10(b)), the resulting Kelvin–Voigt model accurately describes creep behaviour but fails to capture instantaneous elastic response.

Since these basic two-element models provide only qualitative descriptions, more complex models are often constructed by combining multiple Maxwell or Kelvin–Voigt units. A widely used example is the Maxwell–Wiechert model (Figure 2.10(c)), which can represent materials with multiple relaxation times. The number of elements in a generalized Wiechert model depends on the natural distribution of relaxation times within the material.

The relaxation time τ_i for the i-th Maxwell element is defined as:

$$\tau_i = \frac{\eta_i}{G_i} \tag{2.28}$$

where η_i is the viscosity of the i-th dashpot and G_i is the modulus of the corresponding spring.

Using the Maxwell–Wiechert model, the relaxation modulus of any linear viscoelastic material can be described by fitting experimental data from standard relaxation tests to the following Prony series equation:

$$\Psi(t) = G_0 + \sum_{i=1}^{n} G_i \exp\left(-\frac{t}{\tau_i}\right)$$

The spectrum of relaxation times in linear viscoelastic materials can be represented by including as many exponential terms as necessary to achieve the desired accuracy of curve fitting. Once the relaxation modulus function is obtained, the corresponding creep compliance function can be determined using their mathematical relationship in the Laplace domain (see Equation 2.27). When the Maxwell–Wiechert model includes only one relaxation time, it reduces to the Zener model, also known as the Standard Linear Solid (SLS) model. The SLS model is commonly used in numerical studies of viscoelastic contact problems due to its ability to describe both creep and stress relaxation phenomena.

Non-linear Viscoelastic Behaviour

When viscoelastic materials undergo large deformations or when their creep and relaxation functions depend on both time and stress (or strain), their behaviour becomes

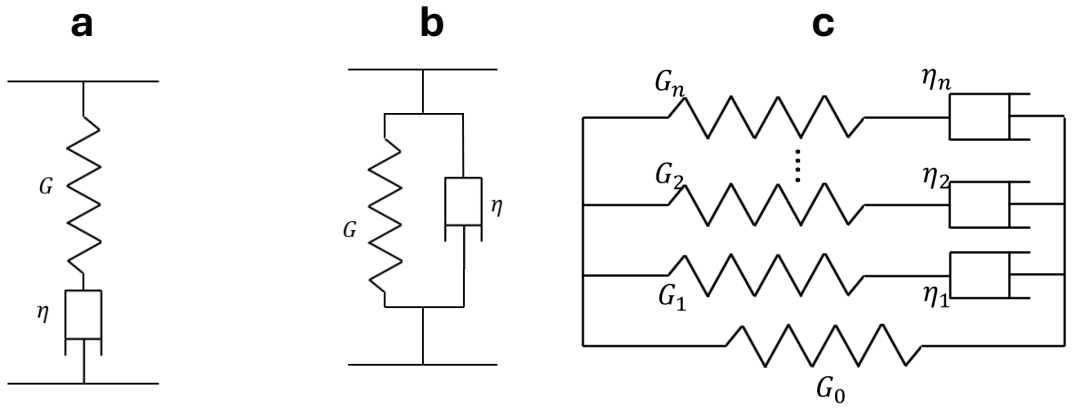

Figure 2.10: Rheological models describing the behaviour of linear viscoelastic materials: (a) Maxwell model, (b) Kelvin-Voigt model and (c) Maxwell–Wiechert.

non-linear. In such cases, the Boltzmann superposition principle is no longer applicable, and more advanced constitutive models are required.

Several researchers have proposed generalized constitutive equations for non-linear viscoelastic materials. Green [45], Spencer [46], and Pipkin and Rogers [47] developed multiple-integral formulations using multivariable relaxation functions as kernels. Leaderman [48], Brueeller [49], and Schapery [50] proposed single-integral approaches based on non-linear stress–strain relationships. These formulations form the basis of modern non-linear viscoelastic constitutive modelling.

2.6 Contact Modelling of Viscoelastic Materials

The study of contact behaviour in viscoelastic materials is essential for understanding and predicting their performance in a wide range of engineering and scientific applications, including seals, biomedical implants, tires, damping systems, and soft robotic components. Accurate modelling of viscoelastic contact phenomena is a critical step in designing reliable components, optimising tribological performance, and assessing durability under realistic service conditions.

This section provides an overview of the main theoretical and numerical approaches used to model viscoelastic contact problems, starting with the simplest case of dry contact. In this scenario, no lubricants are present, thermal effects are neglected, and the material response is assumed to follow linear viscoelasticity. The discussion begins with

the classical indentation problem, which represents the most fundamental type of viscoelastic contact and serves as the basis for analysing more complex interactions.

Subsequently, the focus shifts to tangential contact problems, including quasi-static partial slip contact as well as dynamic sliding and rolling contact conditions. These problems are of particular relevance to real-world applications such as tire-road interactions, polymer-based bearing systems, and various mechanical components subjected to repetitive motion. In addition, models that incorporate surface adhesion effects in viscoelastic contact are examined, highlighting their importance in soft material mechanics, biological interfaces, and contact phenomena at micro- and nanoscale levels.

Together, these modelling approaches form a comprehensive framework for describing the combined effects of deformation, time-dependence, friction, and adhesion in viscoelastic contact mechanics. They also serve as the foundation for more advanced analyses and design methodologies in modern engineering systems.

2.6.1 Indentation

Indentation is the basic setting for viscoelastic contact: a rigid indenter is pressed into, and possibly withdrawn from, a viscoelastic half-space, and the resulting load–depth history reveals the time-dependent response of the material. In the simplest dry and non-adhesive case, linear viscoelasticity makes it possible to recast familiar elastic solutions into time-domain relations by means of hereditary integrals (Figure 2.11 (a)) . This makes indentation a natural starting point before addressing tangential loading, rolling, or surface roughness.

Lee showed that using the Laplace transform reduces linear viscoelastic boundary-value problems to their elastic counterparts, avoiding the direct handling of time-dependent constitutive laws [51]. Radok clarified that this transformation can be applied independently of a particular elastic solution [52]. Assuming non-adhesive contact with a monotonically increasing contact area, Lee and Radok obtained spherical indentation solutions for linear viscoelastic solids [53]. Their analysis implemented what later became known as the elastic–viscoelastic correspondence principle, first introduced by Alfrey [54] and generalized by Tsien [55], in which elastic relations are converted to viscoelastic ones by replacing elastic moduli or compliances with the appropriate relaxation or creep functions. For example, the Hertzian load–depth law $P_{\mathrm{el}} = \frac{4}{3}E^{*}R^{1/2}\delta^{3/2}$ leads, in the Lee–Radok setting, to the hereditary form

$$P(t) = \frac{4}{3}R^{1/2}\int_{0}^{t} E(t-\tau)\,\frac{\mathrm{d}}{\mathrm{d}\tau}\left[\delta(\tau)^{3/2}\right]\mathrm{d}\tau, \tag{2.29}$$

with $E(\cdot)$ the relaxation modulus and $\delta(t)$ the indentation depth.

The original restrictions in [53], namely idealized geometry and a monotonically grow-

ing contact radius, motivated several extensions. Hunter [56] and Graham [57] treated cases with a contact radius that increases monotonically or attains a single maximum. Yang [58] generalized the indenter shape to arbitrary quadratic profiles. Ting [59, 60] removed the monotonicity requirement and allowed arbitrary time-dependent contact radii and multiple, disconnected contact regions, which greatly expanded the range of analytical solutions.

Experimental and theoretical work further developed the indentation framework. Oyen [61] studied pyramidal and spherical indentation under triangular and trapezoidal loading histories. Using Ting's formalism, Greenwood [62] obtained solutions for axisymmetric indenters on a viscoelastic half-space. For full-face contact configurations, Fu [63] derived closed-form relations between load and penetration. Through the correspondence principle, Yakovenko and Goryacheva [64] analyzed periodic contact by arrays of identical spherical indenters, including mutual interactions. Building on Lee and Radok, Papangelo and Ciavarella [65] examined cyclic, repetitive spherical indentation and quantified viscoelastic dissipation. For layered systems, Argatov and Mishuris provided analytical results for elliptical [66], rebound spherical [67], and cylindrical [68] indentation of thin compressible and incompressible viscoelastic layers. Chen et al. [69] used Hankel transforms to treat a viscoelastic layer bonded to an elastic half-space.

Closed-form solutions are powerful but face practical limits when surface roughness, non-monotonic load histories, or complex rheology with multiple relaxation times are present, and the resulting algebra can hinder routine use. These challenges motivated efficient numerical schemes. Kalker solved indentation for arbitrarily shaped rigid punches on a viscoelastic half-space using the matrix inversion method (MIM) [70] and later introduced the two-scale iterative method (TIM) to accelerate boundary element formulations [71]. Using the correspondence principle with the Boussinesq kernel [72], Chen et al. [73] derived the surface displacement response to arbitrary traction fields and implemented a fast FFT-based boundary element method (often called a semi-analytical method, SAM) using discrete-convolution FFT (DC-FFT). Initially aimed at non-conformal normal contact of polymers with broad relaxation spectra and complex topographies, this framework was extended by Koumi et al. [74] to study embedded elastic inhomogeneities and their time-dependent influence on normal and shear stresses, by Liu et al. [75] to investigate composite viscoelastic materials and the effects of inhomogeneity location and volume fraction on effective moduli, and by Spinu [76] to simulate line-contact configurations.

Recent developments include the reformulation by Zhao et al. [77], who expressed surface deformation in terms of the time derivative of the creep compliance rather than pressure, achieving improved efficiency while retaining accuracy. Anisotropic viscoelastic indentation has been addressed by Nguyen and Hwu [78, 79] using boundary element models with time stepping. Beyond continuum BEM, Olsson and Jelagin [80] proposed a discrete-element normal contact model for viscoelastic particles; while effective in many

scenarios, its unloading predictions are approximate because they rely on the Lee–Radok assumptions.

A recurring observation in spherical indentation of viscoelastic bodies is the existence of two distinct pressure profiles: a smooth, Hertzian-like distribution (see, for example, (Figure 2.11-b) in [81]) and profiles that develop pronounced peaks at the contact edge ((Figure 2.11-c) in [81]). Such behaviors have been widely reported in the literature on viscoelastic indentation [77, 81]. To rationalize these differences, Wang et al. [81] carried out a numerical study based on a semi-analytical method (SAM) and showed that the pressure shape is sensitive to the rheological parameters of a standard linear solid, in particular to the ratio of retardation time to relaxation time. An alternative viewpoint was put forward by Koumi et al. [82], who argued that the contact configuration primarily dictates the outcome: a viscoelastic sphere indenting a rigid plane yields a Hertzian-type distribution, whereas a rigid sphere on a viscoelastic half-space produces edge spikes. Together, these results indicate that both the material time scales and the assignment of viscoelasticity to the contacting bodies must be specified to predict pressure profiles reliably.

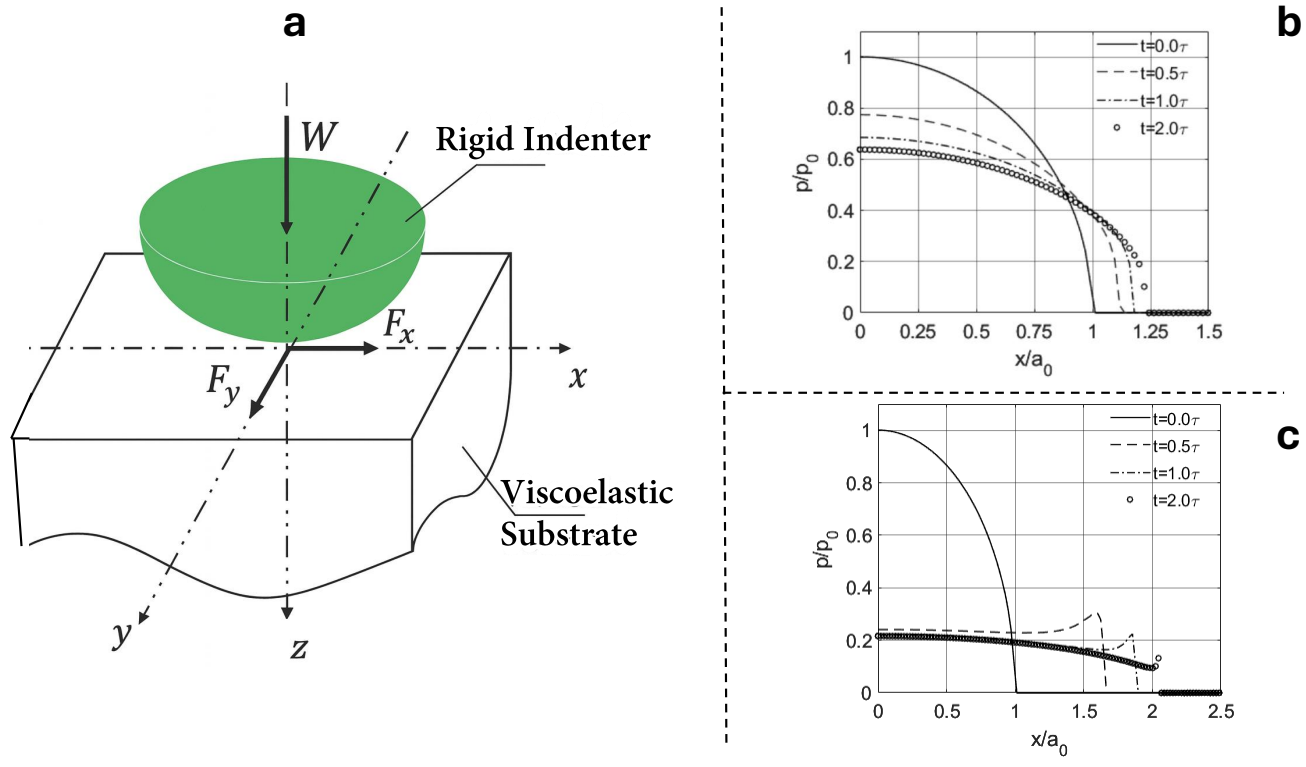

Figure 2.11: Typical geometry of dry viscoelastic contact problems in the indentation case (a). Different shapes of pressure profiles for spherical indentation of viscoelastic bodies, modified from the work of Wang *et al.* [81]: (b) Hertzian-type pressure distribution and (c) pressure profile exhibiting edge spikes. Here, a_0 and p_0 denote the Hertzian contact radius and peak pressure, respectively, calculated using the instantaneous modulus of the viscoelastic material.

2.6.2 Frictionless or frictional sliding and rolling contact

Relative motion between contacting bodies, in the form of sliding or rolling, is common in applications such as tire–road interaction. Early work on viscoelastic substrates began with Hunter [83], who analyzed two-dimensional frictionless rolling of a rigid cylinder on a viscoelastic half-space. At low to moderate speeds the resulting pressure departs markedly from the elastic case, developing an asymmetric profile with a leading-edge spike that drives an asymmetric surface deformation. Morland [84] extended the analysis to line contact between two viscoelastic cylinders with different radii and constitutive responses, while Panek and Kaller [85] generalized Hunter's steady-state result to three-dimensional settings using an approximation based on elastic line-integral theory. Beyond plane strain, Aleksandrov et al. [86] treated the frictionless sliding of a smooth sphere on a viscoelastic half-space. These classical approaches typically assumed idealized rheology with a single relaxation time.

A different analytical route was proposed by Persson [87], who assumed that viscoelastic stiffening with speed can be represented by a frequency-dependent modulus while the pressure remains Hertzian. This theory gives reasonable estimates of rolling friction for rigid cylinders or spheres on flat viscoelastic substrates, but it does not resolve non-Hertzian pressure shapes that arise in force-driven problems.

Finite element models were employed in early numerical studies of viscoelastic sliding and rolling [88–92], but the need for very fine meshes at the interface and in the bulk to capture real roughness and strong gradients limits their efficiency. Boundary-element-based formulations have therefore become popular. Carbone and Putignano [93] developed a steady-state scheme for sliding and rolling in which the viscoelastic medium can be treated as either a half-space [94] or a finite layer [95–97] by adjusting thickness in the governing equations. Their results show that increasing sliding speed reduces the contact area due to viscoelastic effects. Layered configurations were examined by Torskaya and Stepanov [98, 99], who considered a viscoelastic layer on a rigid substrate and a rigid coating on a viscoelastic substrate. For a viscoelastic layer on a rigid base, hysteretic losses grow with layer thickness, whereas a rigid coating on a viscoelastic base exhibits the opposite trend; internal stress fields in smooth sliding contacts were also quantified.

Zhao et al. [77] introduced an efficient formulation for frictionless sliding and rolling by expressing surface deformation in terms of the time derivative of the creep compliance. Transient problems have been addressed by several groups: Koumi et al.[74] simulated rolling of a rigid indenter on a viscoelastic half-space with material inhomogeneity; using Green's function molecular dynamics, Dokum and Nicola [100] obtained transient and steady solutions for frictionless indentation and rolling of a rigid cylinder on a viscoelastic half-plane; Wallace et al. [101] treated transient sliding and rolling with distinct properties in the layer and the substrate; and Zhang et al. [102] investigated imperfect

bonding between layer and substrate, finding that subsurface stresses are reduced when the interface is not perfectly bonded.

It is important to distinguish between the absence of explicit interfacial friction and viscoelastic dissipation. In the "frictionless" studies above, no Coulomb-type shear law is enforced at the interface, so tangential traction does not arise from interfacial friction; however, hysteretic losses due to viscoelasticity are still present and are commonly reported via an apparent friction coefficient times the normal load. When dry friction is present, the contact may experience a quasi-static partial slip regime before gross sliding. In partial slip there is no overall relative motion, but the contact splits into stick and slip zones whose extents evolve with tangential load; in gross sliding the bodies move continuously relative to each other.The typical evolution of the stick and slip regions with increasing tangential load in a spherical viscoelastic partial slip problem is illustrated in Figure 2.12.

Numerical treatments of partial slip in viscoelastic media include a semi-analytical model of conformal pin-on-plate contact by Dayalan and Sundaram [103] for fretting, and a finite element study by Bonari and Paggi [104] for a sinusoidal indenter on a finite viscoelastic layer. Using a boundary-element approach, Wang et al. [81] analyzed spherical contacts with full coupling between normal and tangential tractions and reported an abrupt transition from partial slip to gross sliding driven by the time-dependent nature of viscoelasticity. Nguyen and Hwu [105] obtained stick–slip solutions for anisotropic viscoelastic solids using a time-stepping scheme.

Dry friction in rolling and sliding has also been examined in simplified settings. Goriacheva [106] studied cylindrical rolling with Coulomb friction but found the pressure field unchanged when the two viscoelastic bodies have identical properties, eliminating normal–tangential coupling. Using the Goodman approximation [107], which neglects the influence of shear on normal pressure while retaining the effect of pressure on shear, Goryacheva and Sadeghi [108] analyzed Coulomb friction in cylindrical rolling or sliding of an elastic substrate covered by a viscoelastic layer. Excluding the partial slip stage, Goryacheva et al. [109, 110] simulated frictional sliding of a sphere on a viscoelastic half-space and showed that Coulomb shear increases peak pressure and shifts the contact region in the direction of motion. For rolling with layers, Goryacheva and Miftakhova [111] demonstrated that the extent of local slippage in frictional rolling is strongly affected by the presence and properties of a viscoelastic coating.

Beyond unidirectional motion, reciprocating contacts have been addressed numerically. Putignano, Carbone and Dini [112, 113] developed a boundary element framework for oscillatory contact between a sinusoidal indenter and a viscoelastic half-space. Santeramo et al. [114] proposed a boundary element methodology for conformal contact of viscoelastic materials; although restricted to frictionless, steady-state contact of two-dimensional circular geometries, it complements existing tools for reciprocating and

conformal problems.

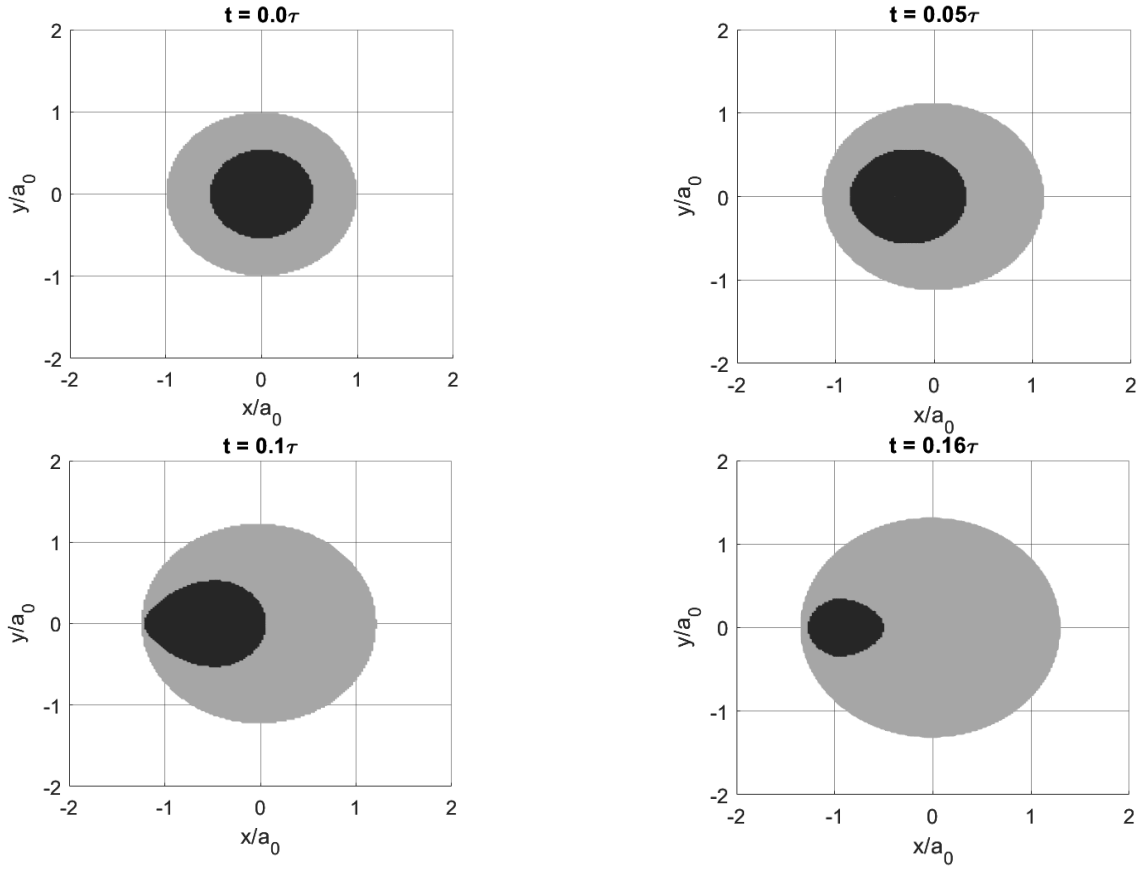

Figure 2.12: Evolution of the stick (dark) and slip (grey) regions with increasing tangential input for a viscoelastic material (reproduced from the work of Wang et al. [81]): (a) t = 0.0τ, (b) t = 0.05τ, (c) t = 0.1τ and (d) t = 0.16τ.

2.6.3 Viscoelastic–adhesive contact

A common limitation of the models reviewed above is the neglect of adhesion. In practice, attractive surface forces are almost always present and decay with separation, and even if they are relatively weak, they can strongly influence contact when, for example, the surfaces are very smooth or one of the bodies is highly compliant [115]. Viscoelastic solids are often soft and readily deformable, so contact with a rigid counterface can create a large real contact area. This narrows the gap between contact pressure and adhesive traction, and omitting adhesion can compromise the reliability of purely viscoelastic predictions.

The combined treatment of adhesion and viscoelasticity is still developing. Many available solutions enrich elastic or viscoelastic formulations with adhesive fields drawn from classical adhesive contact theories, such as the Johnson–Kendall–Roberts (JKR) model and the Derjaguin–Muller–Toporov (DMT) model. Both address a smooth sphere on a flat, but under different assumptions, leading to different results. As summarized by Tabor, the two regimes are separated by a dimensionless Tabor parameter λ, which

depends on the sphere radius, composite modulus, work of adhesion, and interaction range: JKR is appropriate for $\lambda \gtrsim 3$, DMT for $\lambda \lesssim 0.25$. In broad terms, JKR applies to larger, more compliant contacts, whereas DMT is suited to smaller, stiffer ones; neither alone captures all adhesive behaviors.

Fracture mechanics concepts have played a central role in early viscoelastic–adhesive studies [116–118]. Hui et al. [119] combined JKR with viscoelastic fracture mechanics to model spherical contact with adhesion. Using Ting's framework [120] and Tabor's [32] self-consistent adhesive description , Haiat et al. [121] obtained solutions for viscoelastic spheres in adhesive contact. Lin and Hui [122] developed a FEM model with adhesion represented by a Dugdale–Barenblatt cohesive zone [123, 124]. Barthel and Frétigny [125] proposed analytical results for elastomer contacts based on JKR, expressing the effective adhesion energy as a function of the contact-edge velocity. Yu et al. [126] formulated a model that blends the viscoelastic indentation approach of Chen [73] with fracture mechanics (Schapery [50]) and the JKR/DMT/Maugis theories. Using the Maugis–Dugdale law to relate traction to gap, Goryacheva and Makhovskaya analyzed adhesion effects in sliding contacts for spherical indenters [110, 127] and periodic surfaces [109] on viscoelastic substrates.

A fully deterministic normal-contact model was recently proposed by Afferrante and Violano [128] using FEM, where adhesion is introduced via nonlinear springs obeying a Lennard–Jones traction–separation relation, inspired by the Derjaguin approximation [129]. They showed that, for short-range adhesion, viscous dissipation localizes near the contact edge and analyzed pull-off loads for smooth viscoelastic contacts. In parallel, Müser and Persson [130] provided numerical support for the Persson–Brener crack-propagation picture of viscoelastic adhesion [131], finding a maximum in the work of adhesion at intermediate pull-off velocities and emphasizing that realistic dissipation requires an accurate description of short-range adhesion. Carbone et al. [132] numerically examined steady sliding with adhesion and reported that the hysteretic friction versus velocity curve is markedly altered compared to the adhesiveless case, exhibiting a more pronounced peak.

At smaller scales and with patterned surfaces, Yang et al. [133] simulated the adhesive contact between a sphere and a two-dimensional nano-wavy surface and found that viscoelastic effects are negligible at high approach speeds, but at low speeds they increase the maximum contact area and the pull-off load relative to purely elastic behavior. They also observed a monotonic dependence of pull-off force on the waviness parameter and a nonmonotonic trend for the maximum contact area. More recently, Pérez-Ràfols et al. [134] studied adhesive hysteresis and concluded that the effective work of adhesion increases due to viscoelastic stiffening, and, in cases where viscoelastic dissipation is confined to the edges of a wavy contact, the contributions of surface roughness and viscoelasticity to hysteresis appear approximately additive. This assertion warrants further

investigation because their analysis considered a single-wavelength roughness rather than a broadband, realistic rough surface.

2.7 Importance of Interface Contact in Shell Adhesion and Buckling

Adhesion between thin deformable shells and solid substrates is a complex phenomenon governed by interfacial interactions that couple surface physics and structural mechanics. The stability and deformation of such systems depend not only on the elastic properties of the shell but also on how adhesive tractions and interfacial friction are distributed across the contact region. In many soft structures—such as polymeric capsules, hydrogel lenses, and biological membranes—the interfacial contact dictates mechanical performance, energy dissipation, and failure modes. Therefore, understanding the role of the interface in controlling deformation, frictional resistance, and buckling is essential for predictive modeling of adhesive shells.

When two deformable surfaces come into proximity, the contact is not purely mechanical but strongly influenced by surface forces acting over nanometer-scale separations. These forces determine the equilibrium gap profile, the true contact area, and the interfacial stiffness. In thin shells, the interplay between curvature, bending rigidity, and surface energy allows large contact zones to form even under minimal external load. Such compliant interfaces are crucial in biological adhesion, flexible electronics, and soft robotic systems [135–137].

The interface contact governs not only adhesion strength but also the onset and nature of mechanical instabilities such as buckling. Adhesive tractions can either suppress or promote buckling, depending on their magnitude and spatial distribution. A uniform attractive force may stabilize the shell by constraining out-of-plane displacements, whereas localized tensile stresses near the contact edge can trigger early wrinkling or delamination. The coupling between interface traction and shell curvature alters the effective stiffness and affects the critical buckling load [138–140]. Thus, the interface must be treated as an active mechanical participant rather than a passive boundary condition when analyzing shell stability.

The mechanical response of thin adhesive shells is governed by a competition between bending rigidity and in-plane stretching. For small deformations, bending dominates, while at larger displacements the in-plane stretching of the shell becomes significant. The total elastic energy can therefore be viewed as the sum of bending and stretching contributions. The ratio of bending to stretching energy defines the shell's compliance and dictates its preferred mode of deformation.

The presence of adhesion introduces an additional energy term associated with the

work of adhesion per unit area, γ, which may be expressed as

$$U_\gamma = -\int_A \gamma \, dA. \tag{2.30}$$

The total potential energy of the system can therefore be written as

$$\Pi = U_B + U_S - U_\gamma - W_{\text{ext}}, \tag{2.31}$$

where U_B denotes the bending energy of the shell, U_S corresponds to the stretching energy, U_γ represents the adhesion energy, and W_{ext} is the external work performed by applied mechanical actions (e.g., pressure or prescribed displacement).

Buckling occurs when the stored elastic energy exceeds the stabilizing effects of adhesion and boundary constraints. The competition between stretching and adhesion determines the critical adhesion level required to suppress buckling. In particular, a representative scaling of the stretching contribution can be written as $U_S \sim Eh \left(\frac{du}{dx}\right)^2$, highlighting its significance in governing the onset of instability.

In summary, the deformation and stability of adhesive shells are governed by the balance between bending and stretching energies together with the adhesive work at the interface. The appropriate formulation and scaling of the stretching contribution are crucial for predicting the transition from smooth deformation to buckling instability.

2.7.1 Effect of Friction at the Interface

While adhesion governs normal tractions, friction acts tangentially and plays a complementary role in determining the interfacial response. Friction resists relative sliding between the shell and the substrate, effectively constraining in-plane motion and redistributing stresses in the contact region. The presence of interfacial friction enhances resistance to delamination and may delay local buckling by providing additional in-plane constraint [141, 142].

However, friction can also promote shear-induced instabilities, particularly when the contact involves cyclic or asymmetric loading. During progressive deformation, static friction transitions to kinetic friction, introducing hysteresis and energy dissipation. These effects are particularly significant in viscoelastic shells, where frictional dissipation and adhesion hysteresis jointly control the overall mechanical response [140, 143].

Therefore, realistic modeling of soft-shell interfaces requires simultaneous consideration of both adhesion and friction. Neglecting either mechanism may lead to inaccurate predictions of load-bearing capacity, critical buckling conditions, and detachment behavior.

Summary and Outlook

In this chapter, a comprehensive review of the theoretical and experimental foundations underpinning adhesion, friction, and viscoelastic contact mechanics was presented. Beginning from the fundamental van der Waals interactions between atoms and surfaces, the discussion extended to classical adhesive contact theories such as the Hertz, JKR, DMT, and Maugis models, highlighting their respective regimes of validity and limitations. The constitutive behavior of viscoelastic materials was also reviewed in detail, with emphasis on the time-dependent nature of stress and strain, as well as theoretical models such as the Maxwell, Kelvin–Voigt, and Standard Linear Solid (SLS) frameworks. Furthermore, analytical and numerical approaches to viscoelastic contact, including indentation, sliding, and rolling, were summarized.

The final sections focused on the importance of interfacial interactions in the mechanics of thin shells, emphasizing how adhesion and friction can influence local stress distributions, stretching, bending, and the onset of buckling. These mechanisms form the basis for understanding how adhesion and friction may stabilize or destabilize thin structures in contact with rigid substrates.

This literature review thus establishes the theoretical context for the subsequent chapters of the thesis. Chapter 3 presents a finite element and experimental investigation of *adhesion- and friction-induced suppression of buckling in thin spherical shells*, where the concepts of bending and stretching energy balance are applied to predict critical adhesion thresholds. Chapter 4 extends the study to the *sliding friction of viscoelastic cylinders with adhesion*, quantifying the influence of the Maugis–Tabor parameter on the transition between adhesive and viscoelastic dissipation regimes. Chapter 5 explores *rolling friction in viscoelastic media*, drawing inspiration from the classical experiments of Barquins and Roberts and validating the numerical results against the Persson–Brener analytical framework.

Together, these chapters form a coherent narrative linking surface adhesion, frictional dissipation, and viscoelastic deformation across structural and tribological scales. The understanding gained from the literature review serves as the conceptual bridge between classical contact mechanics and the new results developed in the following chapters.

Chapter 3

Adhesion and Friction Effects on Buckling Suppression in Thin Spherical Shells

Preface

This chapter presents the first original research contribution of this thesis, focusing on the effect of adhesion and friction at the contact interface of thin shells. A theoretical and numerical framework is developed and compared to experiments to analyze the mechanical response of shell structures interacting with adhesive and frictional surfaces. The study investigates how interfacial forces influence deformation patterns, stress distribution, and overall stability. The findings contribute to a deeper understanding of the coupled effects of adhesion and friction in shell contact mechanics [144].

3.1 Introduction and Problem Definition

Soft shell structures are widely found in both natural and engineered systems, known for their ability to sustain large deformations under relatively small external forces. In biological contexts, such structures play essential functional roles [145–147]. In engineering applications, they are utilized in a wide range of systems, including sports equipment, capsules, flexible electronic devices, and soft robotic mechanisms [148–151] where accurate control of their form and stability is crucial. A characteristic nonlinear mechanical response observed in these systems is the snap-back instability, which involves a sudden and discontinuous shift to a new equilibrium configuration after a critical load or displacement is exceeded [152–154]. This behavior, identified by a negative slope in the force–displacement curve, underlies the operation of many bistable systems, MEMS devices, and semiconductor junctions during breakdown. In this work, such instability in thin shells interacting with a rigid surface is referred to simply as "buckling."

The intrinsic tendency of thin shells to experience snap-back and other nonlinear

deformation modes introduces significant complexity to their design and control. Consequently, numerous studies have sought to elucidate the buckling mechanisms of shell structures [6, 155, 156]. Hutchinson and Thompson [7] explored the nonlinear post-buckling behavior of ideal spherical shells under external pressure, while Paulose and Nelson [8] demonstrated the influence of soft caps on their stability. The impact of thermal environments on reinforced cylindrical shells has also been extensively examined [157–159]. Other investigations have emphasized the significance of loading conditions, revealing that local indentation induces stronger nonlinear responses compared to uniform or global loading [160, 161]. Experimental and computational analyses by Nasto et al. [162] characterized the localized deformation of spherical elastic shells under indentation, and Tseng et al. [163] studied the post-buckling responses of elastoplastic double-curved shells, such as ping-pong balls, when compressed by different indenter geometries. More recently, Abe and Sano [9] investigated the snap-buckling behavior of hemispherical shells in contact with rigid cylindrical supports of varying diameters, emphasizing the critical role of boundary constraints in dynamic shell responses. Analytical models linking indentation load, displacement, and structural parameters have also been proposed to better describe the indentation mechanics of shells [164, 165].

Despite these advancements, the influence of interfacial effects—particularly adhesion and friction, which depend on surface roughness—on shell buckling remains insufficiently understood. While recent studies [166–168] have begun addressing friction and surface texturing, the role of adhesion has received comparatively little attention. Existing work on adhesion has primarily focused on small deflections and pre-buckling regimes [169–173], leaving fundamental questions unresolved—such as how adhesion influences the initiation of buckling and whether it can mitigate instability under large deformations. To bridge this gap, the present study systematically investigates the evolution of contact in elastic thin shells by incorporating both adhesive and frictional interactions, using finite element simulations complemented by experimental validation.

3.2 Finite element method with friction and adhesion

Numerical simulations were conducted using the Ansys APDL mechanical package. The hemispherical shell was modeled with an internal radius R and thickness h, and was assigned a linear elastic material with a Young's modulus $E = 1.3\,\mathrm{N/mm^2}$ and Poisson's ratio $\nu = 0.45$. The stiff plates were treated as rigid bodies in the simulation.

The shell was represented by a 2D axisymmetric, 8-node element with quadratic displacement behavior (PLANE183). It is known that shells may, in general, undergo asymmetric deformation modes under certain loading and imperfection conditions [174].

In the present work, we first performed physical indentation tests on hemispherical elastic shells, and the measured deformed configurations remained axisymmetric both before and after instability. These experimental observations motivated the adoption of an axisymmetric numerical formulation. Consequently, the shell was modeled using a quarter domain under axisymmetric boundary conditions, which ensures computational efficiency while accurately reproducing the observed deformation patterns, as also supported by similar studies in the literature [175, 176].

For contact modeling, surface-to-surface contact was implemented using a mortar-based master– slave interpolation, while the contact constraint was enforced through the penalty formulation associated with CONTA172 and TARGE169 elements. To ensure numerical accuracy, a mesh sensitivity study was conducted, confirming that the results were insensitive to further mesh refinement.

An iterative scheme was employed to incorporate adhesion into the numerical simulations, as implemented in Ref. [177].

The interactions between the rigid plate and the elastic shell are described by the Lennard-Jones (LJ) force-separation law, which defines the stress between the two interacting surfaces $p(g)$ as:

$$p(g) = -\frac{8\Delta\gamma}{3g_0}\left[\left(\frac{g_0}{g}\right)^3 - \left(\frac{g_0}{g}\right)^9\right] \tag{3.1}$$

where g is the local gap between the two interacting surfaces, g_0 is the equilibrium separation distance and was set to 0.1 mm, $\Delta\gamma = g_0\alpha\sigma_0$ is the surface energy, and

$$\alpha = \frac{9\sqrt{3}}{16} \approx 0.9743. \tag{3.2}$$

The use of an LJ-3-9 law is commonly adopted in adhesive contact mechanics because the attractive g^{-3} term approximates long-range van der Waals forces, while the repulsive g^{-9} contribution provides a numerically stable penalty-like behaviour near contact.

Since the compressive interaction is already accounted for by the contact elements in ANSYS APDL, we focus only on the adhesive interaction. To isolate the adhesive component, we introduce a shifted gap $g' = g - g_0$ and substitute it into Eq. (3.1):

$$p(g') = -\frac{8\Delta\gamma}{3g_0}\left[\left(\frac{g_0}{g'+g_0}\right)^3 - \left(\frac{g_0}{g'+g_0}\right)^9\right]. \tag{3.3}$$

where Eq. (3.3) is used to model only the adhesive interactions, hence only for $g' > 0$.

The simulation procedure is as follows: first, a prescribed displacement δ is applied to the top nodes without considering adhesion. Next, the gap between the nodes of the interface and the rigid surface is calculated. Then, using the adhesive stress given by Eq. (3.3), the adhesive force is calculated as:

$$F_{\text{adhesive}} = p(g') \cdot A \tag{3.4}$$

where $A_i = \pi\left(x_{i+1}^2 - x_i^2\right)$ is the area of the annulus at which the adhesive force is applied, with x_{i+1} and x_i being the x-coordinates of two consecutive nodes. This adhesive force is then applied to the interface nodes. Finally, the problem is iteratively solved for the specified displacement δ with the adhesive force included. Further details on this approach can be found in Ref. [177]. Moreover, friction was incorporated into the numerical model using a Coulomb friction formulation. This allowed simulation of interfacial behavior under both adhesive and frictional interactions. The schematic of applying adhesion and the problem model can be seen in Figure 3.1(a-b).

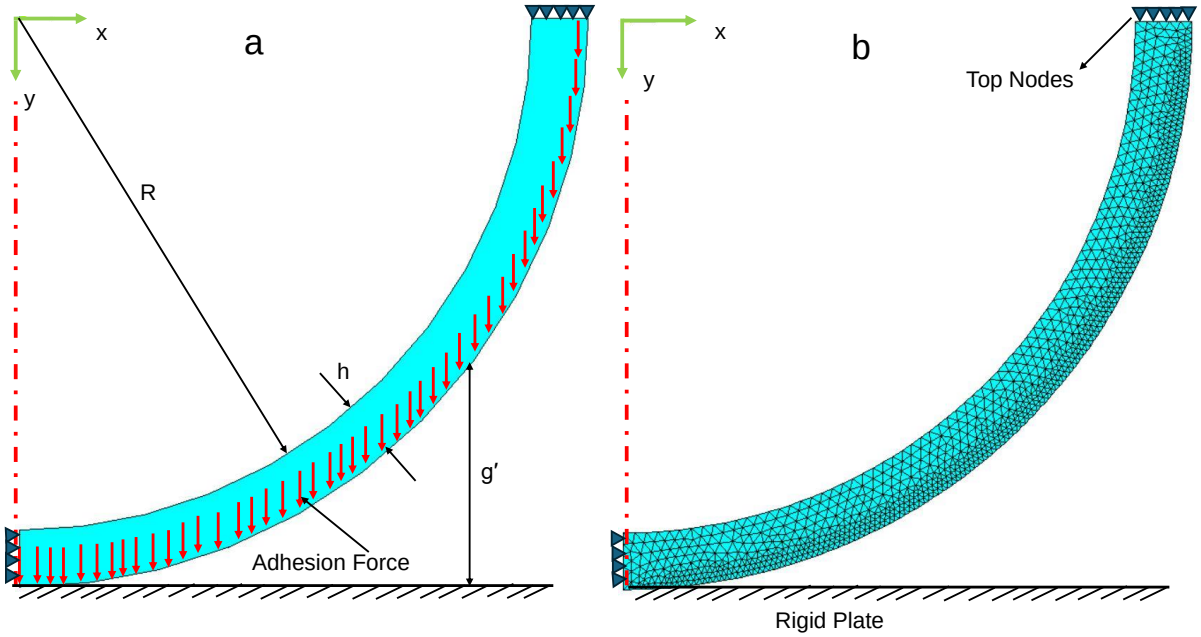

Figure 3.1: (a) Schematic representation of adhesion implemented in the finite element model (b) The mesh of the axisymmetric shell model.

In a study by Audoly et al. [6], the flattening of a spherical shell under a pushing plate was modeled under frictionless and adhesionless conditions. The authors defined a critical force $F_c = \frac{Eh^3}{R}$ as a benchmark for the applied force. For small loads ($F < F_c$), the shell undergoes minimal deformation, displaying Hertz-like contact with a circular shape contact area. As the force increases ($F \geq F_c$), the contact area expands into a disk shape, with equilibrium determined by a balance of bending and stretching. At larger forces ($F \gg F_c$), the accumulated stretching energy is released, causing the shell to invert.

In a previous study [167] investigating the effect of friction on the buckling behavior of thin shells, three distinct deformation regimes were identified based on the critical force F_c. In this work, we extend the analysis by incorporating adhesion γ into our numerical

model. We then compute F_c to assess whether these three deformation regimes remain distinguishable in the presence of adhesion.

Figure 3.2 illustrates the variation of F as a function of δ for both the adhesionless case and the case with adhesion. By comparing F with the critical force $F_c = 0.086$ N, we observe that the three previously identified deformation regimes remain clearly distinguishable. This demonstrates that, even in the presence of adhesion, the critical force criterion remains valid. The buckling force F_{buckling} (i.e., the maximum force before instability occurs) is of the order of the critical force F_c so we can write $F_{\text{buckling}} = kF_c$, where k is a constant prefactor: in the case under investigation, considering adhesion, $k \approx 7.5$, as shown in Figure 3.2.

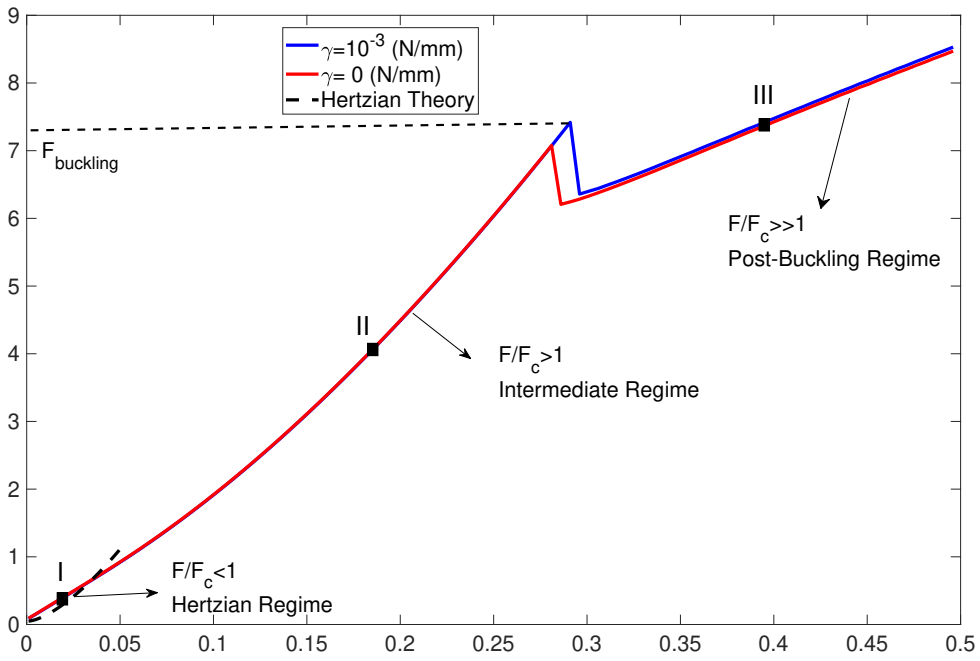

Figure 3.2: Evolution of the normalized load, $\bar{F} = \frac{FR}{Eh^3}$, as a function of the normalized approach distance, $\bar{\delta} = \delta/R$, for the adhesionless and $\gamma = 10^{-3}$ N/mm cases, $\mu = 0$, $R = 15$ mm, $h = 1$ mm and $E = 1.3\,\text{N/mm}^2$

Additionally, the shell profile, contact area, and pressure distribution corresponding to three points (I, II, III) located in different contact regimes, as shown in the previous figure, are depicted in Figure 3.3.

In the Hertzian regime (point I), which marks the onset of contact, the contact area is very small and circular, while the pressure distribution exhibits a characteristic elliptical shape. As the load increases, the system transitions into the intermediate regime (point II), where the shell profile flattens, approaching intimate contact with the rigid plane. The contact area expands into a disk-like shape, and the pressure distribution deviates from the Hertzian profile, becoming asymmetrical. In the post-buckling regime (point III),

the shell profile inverts, forming a concave shape. The contact area contracts, adopting a ridge-like geometry, while the pressure distribution returns to a elliptical form with magnitudes higher than those observed in the earlier regimes [178, 179].

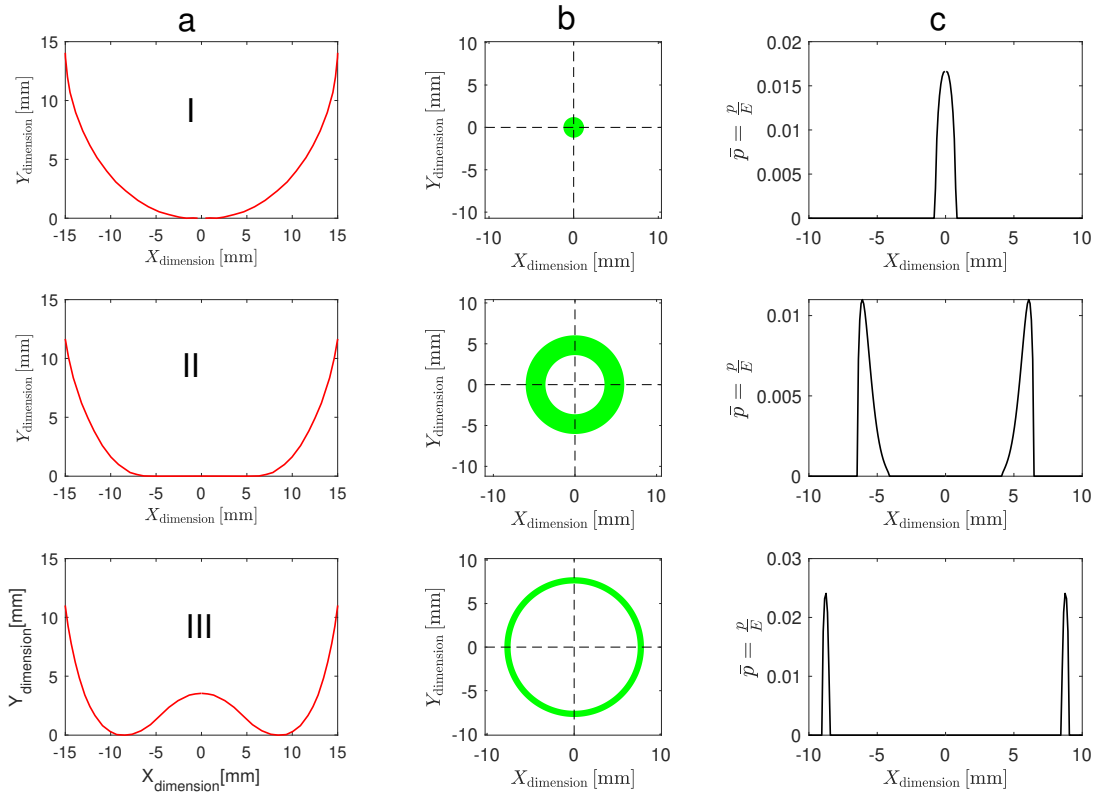

Figure 3.3: Shell profile (a), contact morphology (b), and pressure distribution (c) of the shell indented on a rigid plate across three distinct regimes: Hertzian (I), intermediate (II), and post-buckling (III) for the blue curve in the Figure 3.2 .

The evolution of the contact mechanism of a thin elastic shell can be described using the parameters E, h, R, γ, and μ. Two dimensionless parameters are derived: $\frac{\gamma}{Eh}$, which represents the effect of adhesion, and $\frac{h}{R}$, which captures the geometric influence. Additionally, μ, the coefficient of friction, is considered. The results are presented in terms of these parameters.

To investigate the role of adhesion, simulations were conducted at constant $h/R = 0.06$ with varying adhesion strength γ, $E = 1.3\,\mathrm{N/mm^2}$ and zero friction ($\mu = 0$). Figure 3.4(a) shows that the contact force increases with indentation until a buckling instability occurs, after which the force continues to rise with a lower slope. As γ increases, instability is progressively delayed until a critical threshold γ_c is reached, beyond which instability is completely suppressed. In this case, for $\gamma > \gamma_c = 5.4\,\mathrm{N/mm}$ (red curve), the shell remains stable even at high indentation levels. Moreover, in the post-buckling regime, the curves converge, indicating a diminished role of adhesion beyond the instability.

Figure 3.4(b) presents the normalized contact pressure $\bar{p}_{\max} = p_{\max}/E$, clearly high-

lighting three regimes: Hertzian, intermediate, and post-buckling. For $\gamma > \gamma_c$, the pressure increases smoothly without an instability-induced jump.

Figure 3.4(c) shows the evolution of normalized contact area $\bar{A}$. A sharp drop at instability is followed by a a mild and gradual decrease in the post-buckling regime, in contrast to the monotonic area growth seen in bulk spheres [30].

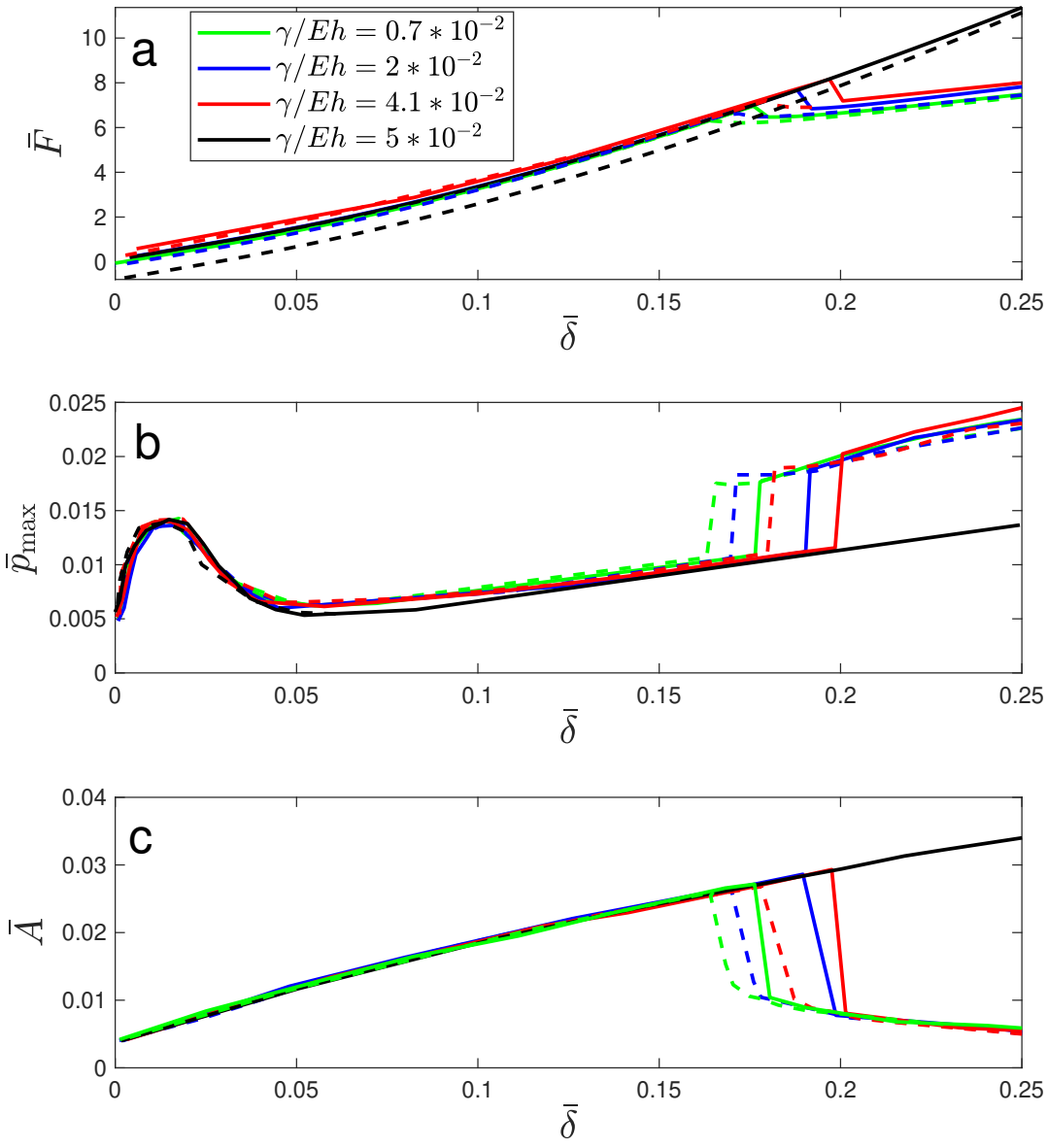

Figure 3.4: The evolution of (a) the normalized force, $\bar{F} = \frac{FR}{Eh^3}$, (b) the normalized maximum contact pressure, $\bar{p}_{\max} = \frac{p_{\max}}{E}$, and (c) the normalized contact area, $\bar{A} = \frac{2A}{\pi R^2}$, as a function of the normalized indentation, $\bar{\delta} = \frac{\delta}{R}$, for different values of γ/Eh, $\mu = 0$, $E = 1.3\,\mathrm{N/mm^2}$, and $h/R = 0.06$. Solid lines represent loading, while dashed lines represent unloading paths.

To investigate the effect of friction on the buckling behavior of thin shells, Figure 3.5(a–c) presents the variation of force, pressure, and contact area during a loading-unloading process across a friction coefficient range of $\mu = 0$ to $\mu = 1.5$. In this range, buckling is completely suppressed at high friction values.

From Figure 3.5-(a), the buckling (instability) load increases with increasing μ, reaching a point where, for $\mu = 1.5$, instability is entirely suppressed.

The post-buckling force evolution is strongly influenced by friction. As the coefficient of friction increases, it opposes compressive stresses within the shell, thereby raising the critical force required to initiate instability. This finding underscores the crucial role of frictional mechanics in governing the structural stability of thin shells. Figure 3.5(b - c) illustrates the relationship between maximum pressure, contact area, and indentation for different values of μ. Similar trends are observed for friction. For high friction ($\mu = 1.5$), where buckling is absent, both contact area and pressure continue to increase with indentation monotically. In contrast, for lower μ, where buckling occurs, a sudden drop in contact area is accompanied by a sharp increase in pressure. Interestingly, in the post-buckling regime, the contact area remains constant despite the continued increase in indentation force.

Although the external load acts predominantly in the normal direction, the indentation process induces in-plane stretching and sliding of the shell along the contact interface. In the absence of friction, this tangential reconfiguration can occur freely, facilitating the development of the unstable snap-through mode. When friction is present, the interface resists relative sliding and therefore constrains the in-plane deformation field. This generates additional membrane stresses that stiffen the pre-buckling configuration, increasing the load required to trigger instability. The net result is a strong stabilizing effect arising solely from the geometric coupling between normal indentation and tangential displacement.

Figure 3.6(a-d) illustrates how the buckling force F_{buckling}(the maximum value before instability begins) and the dissipation energy $W = \oint F\,dx$ vary with adhesion and friction.

From Figure 3.6(a-b), increasing adhesion elevates F_{buckling}, thereby delaying buckling. At high adhesion ($4.5 \times 10^{-2}\,\text{N/mm}$), instability is fully suppressed even at low friction. In contrast, increasing friction also raises F_{buckling}, but with a steeper trend. This is because higher friction (μ) increases resistance to tangential motion, allowing greater accumulation of elastic strain energy, which in turn enhances the shell's resistance to deformation. Additionally, in Figure 3.6(a), a linear trend in the buckling (instability) load with increasing friction can be observed. Although this trend is apparent, we cannot confirm its validity near the threshold of instability disappearance, due to numerical resolution and convergence limitations.

Regarding energy dissipation, Figure 3.6(c-d) show that dissipation energy follows a parabolic trend with increasing friction. It initially rises with μ, peaks around $\mu = 1$, and

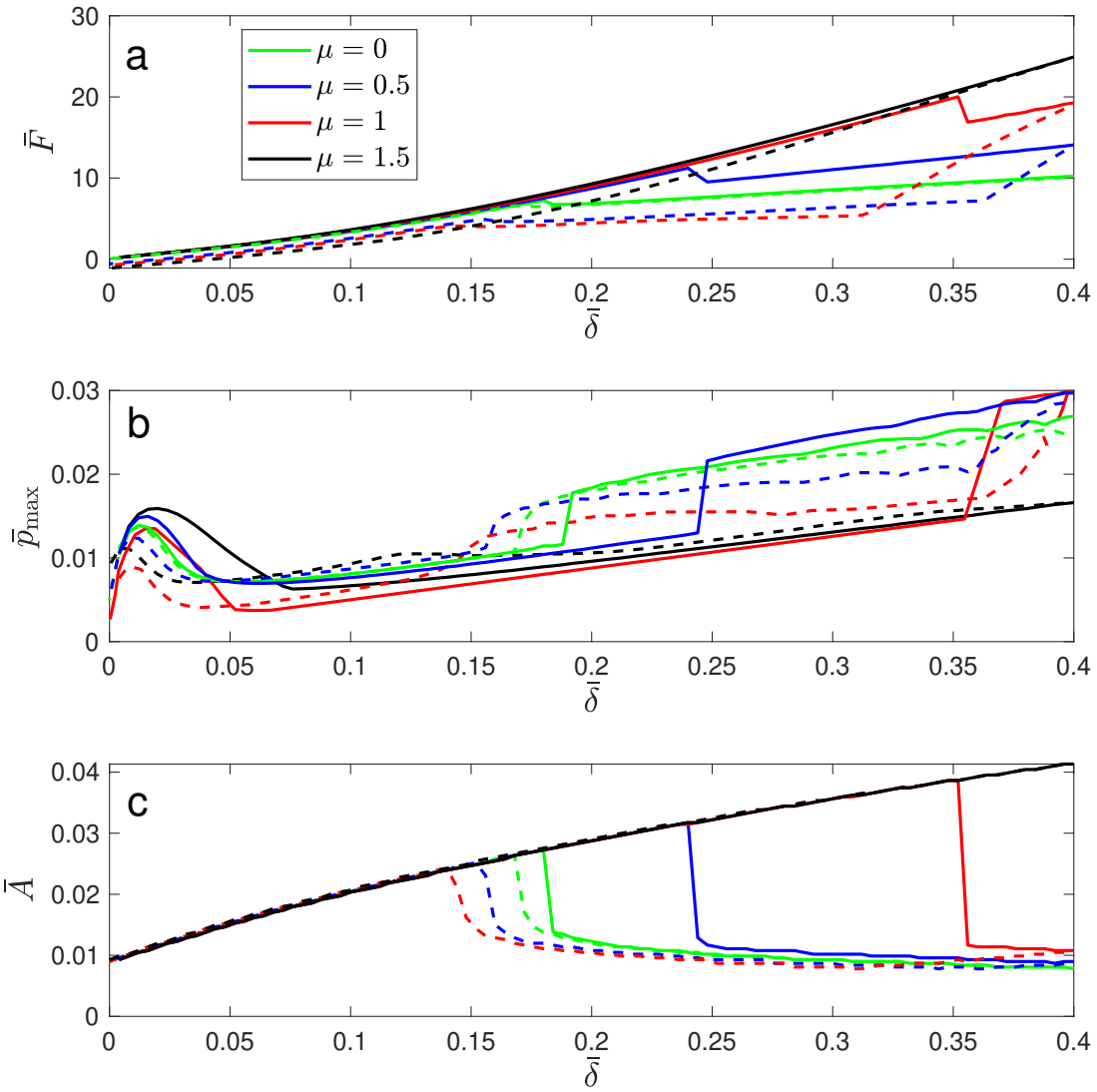

Figure 3.5: The evolution of (a) the normalized force, $\bar{F} = \frac{FR}{Eh^3}$, (b) the normalized maximum contact pressure, $\bar{p}_{\max} = \frac{P_{\max}}{E}$, and (c) the normalized contact area, $\bar{A} = \frac{2A}{\pi R^2}$, as a function of the normalized indentation, $\bar{\delta} = \frac{\delta}{R}$, for different values of μ. Here, $E = 1.3\,\mathrm{N/mm^2}$, $h/R = 0.06$, and $\gamma = 2 \times 10^{-3}\,\mathrm{N/mm}$. Solid lines represent loading, while dashed lines represent unloading paths.

then decreases as buckling is suppressed at higher friction levels ($\mu = 1.5$). For the case with high adhesion ($4.5 \times 10^{-2}\,\mathrm{N/mm}$), shown by the black curve in Figure 3.6(c), where buckling is suppressed at lower friction levels, the dissipation energy initially follows a parabolic trend up to approximately $\mu \approx 1$. Beyond this point, instability is fully suppressed, and the energy increases gradually due to the continued rise in μ.

In contrast, dissipation energy due to adhesion increases slowly and monotonically with adhesion, regardless of whether buckling is suppressed. However, this increase re-

mains modest compared to that caused by friction. This distinction is attributed to post-buckling behavior: after the buckling, the contact area is significantly reduced, minimizing the influence of adhesion. Meanwhile, friction continues to resist tangential motion during unloading, leading to greater energy loss.

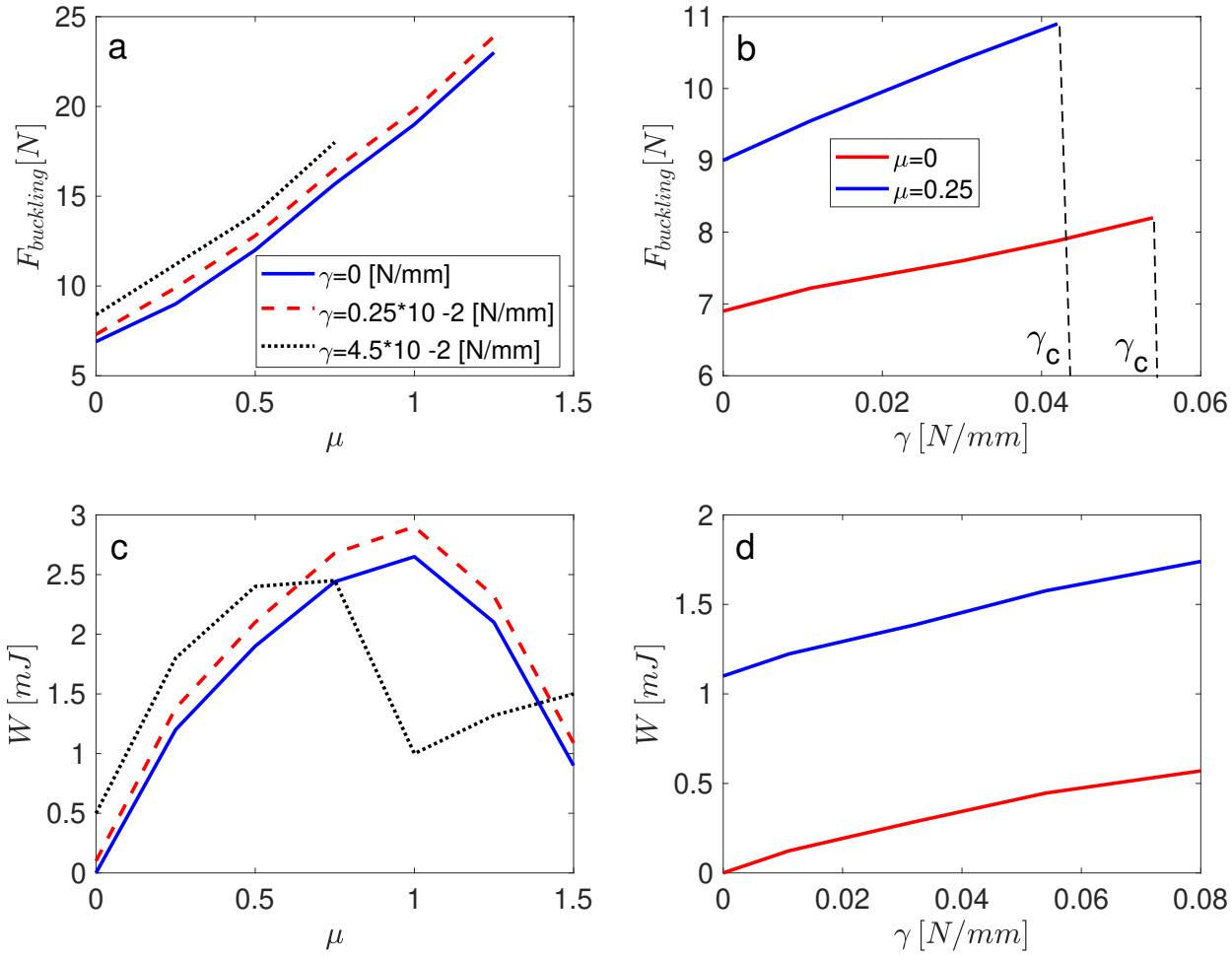

Figure 3.6: Variation of buckling force F_{buckling} as a function of μ and γ (a, b) and variation of dissipation energy W as a function of μ and γ (c, d) for $E = 1.3\,\text{N/mm}^2$, and and $h/R = 0.06$

3.3 Experiments

3.3.1 Fabrication and Experimental Setup

The polymer shells were fabricated using a cross-linked mixture of polydimethylsiloxane (PDMS), a commercially available elastomer chosen for its excellent mechanical properties. The base and curing agent were mixed in a 10:1 ratio, and then degassed in a

desiccator for 10 min before sample manufacturing. The mixture was then cured at 25°C for 48 hours to ensure proper cross-linking [180]. PLA plates with various surface treatments served as the rigid substrates, providing consistent and stable surfaces for the soft polymer shells. A steel ball bearing was used as a smooth spherical mold for pouring the liquid PDMS mixture to create thin shells. During fabrication, the silicone-based liquid PDMS solution was poured onto the spherical mold (supplier WILHELMSEN A/S, steel ball 50 mm, ref. KU 50G500), where it drained under the effect of gravity to achieve uniform coverage across the surface. The shell thickness was monitored for uniformity using a Keyence VR-3000 series profilometer, yielding shells with a small thickness variation as noted in Ref [181]. The hemispherical shells are mounted on base plates that feature a circular slit with a depth of 1.75 mm. Each base plate includes a central hole and slits on the opposite side to alleviate the effects of internal pressure within the hemispherical shell during loading and unloading.

The test setup includes a commercial ZwickRoell testing machine (serial number 182378/2008) with a nominal load capacity of 500 N. A ZwickRoell Xforce HP 50N load cell (serial number 775181/2018) is attached to this machine, with the base plate secured onto a compression tool connected to the load cell.

In each test, the shell is initially brought into adhesive contact with the substrate by applying displacement at a rate of 10 mm/min until a preset distance is reached. As compression continues, the contact area expands, causing the contact radius, a, to increase. The shell is subsequently retracted from the substrate at an unloading rate of 10 mm/min. The fabrication process and experimental setup are illustrated in Figure 3.7.

3.3.2 Experimental results and comparison with FEM

To experimentally validate the numerical findings regarding the influence of friction and adhesion on shell buckling, we conducted loading and unloading tests with controlled surface roughness. The experiments aimed to establish a correlation between surface roughness, adhesion/friction characteristics, and the buckling behavior of thin shells. Three distinct surface finishes were prepared: low (3 μm), moderate (15 μm), and high roughness (27 μm).

Figure 3.8 presents the experimentally derived contact force versus indentation curves (solid lines) for each surface roughness condition. The tested shells possessed a radius $R =$ 25 mm, a thickness $h = 0.9$ mm, and an elastic modulus $E = 1.3$ N/mm^2. Using these material parameters, numerical simulations were conducted to compute the contact force versus indentation curves (dashed lines), which are also shown in Fig. 3.8 for comparison and verification purposes.

To determine the surface energy (γ) of PDMS shells in each experiment, we used the JKR pull-off formulation:

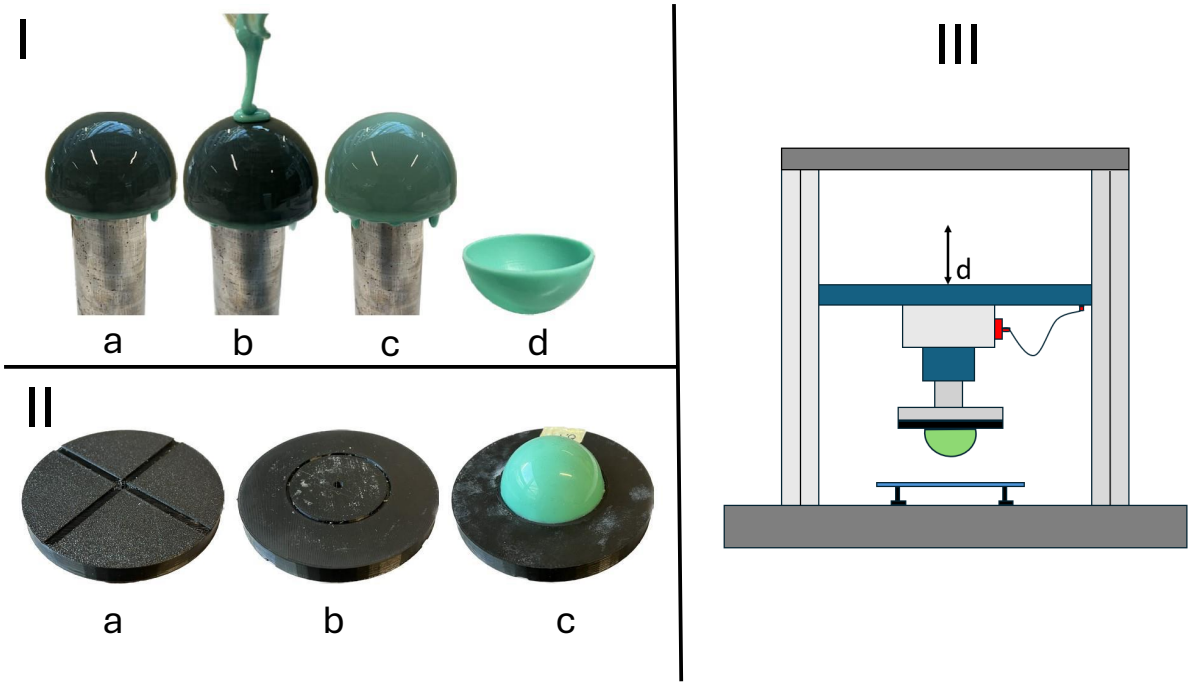

Figure 3.7: Fabrication process and experimental setup. (I) Fabrication process of the shells: (a) the shell with the initial layer, (b) the pouring process, (c) the shell after the pouring and curing process, and (d) the final result. (II) Base plate setup used for the experiments: (a) top view of the base plate showing the four air-slits, (b) bottom view of the base plate with a circular cutout used for fixing the hemispherical shell and a central hole to avoid internal pressure, and (c) the hemispherical shell fixed to the base plate. (III) Schematic of the experimental setup.

$$F_{\text{pull-off}} = \frac{3}{2}\pi R\gamma \tag{3.5}$$

Based on the pull-off forces measured during the experiments, γ was calculated for different tests corresponding to the highest (0.11×10^{-3} N/mm), moderate (0.145×10^{-3} N/mm), and lowest (0.185×10^{-3} N/mm) roughness, respectively. The obtained values of γ were then incorporated into the simulations accordingly. Moreover, to define the coefficient of friction of surfaces, we know it is highly dependent on roughness, but also on normal load[13, 115, 182, 183] and therefore we did not repeat direct measurements which in the previous study [167] found friction under dry conditions as 1±0.2 and under lubricated conditions as 0.5, whereas simulations reported the coefficient of friction required to suppress buckling was as high as 2. or 2.2.

It is important to note that in real experiments the roles of adhesion and friction are not completely separable, since tangential resistance may influence normal detachment and vice versa. Nevertheless, in numerical simulations these two effects can be varied independently, making it possible to isolate the influence of adhesion energy γ from that of friction coefficient μ. Therefore, although the calibration process remains approximate in practice, numerical parametric studies enable us to identify which portion of the response

is predominantly governed by interfacial adhesion and which is associated with frictional constraint.

Here, the experimental results demonstrate a good agreement with the numerical simulations if we selected friction coefficients (μ) of 0.75, 1, and 2, as evidenced by the comparable trends in the contact force versus indentation curves. Specifically, the surfaces with high and moderate roughness, characterized by $\mu = 0.75$ and $\mu = 1$, and $\gamma = 0.11 \times 10^{-3}$ and $\gamma = 0.145 \times 10^{-3}$ N/mm, respectively, experienced buckling and demonstrably higher energy dissipation. In contrast, the smooth surface, possessing higher adhesion and friction (0.185×10^{-3} and $\mu = 2$), did not undergo buckling; the applied load increased continuously with indentation. Notice therefore that the main experimental novelty with respect to the previous study [167] is that we did succed in suppressing instability experimentally, although we are not completely sure if this is due to obtaining higher coefficient of friction, or because of the effect of adhesion — see Discussion paragraph to explore the full map of the two effects.

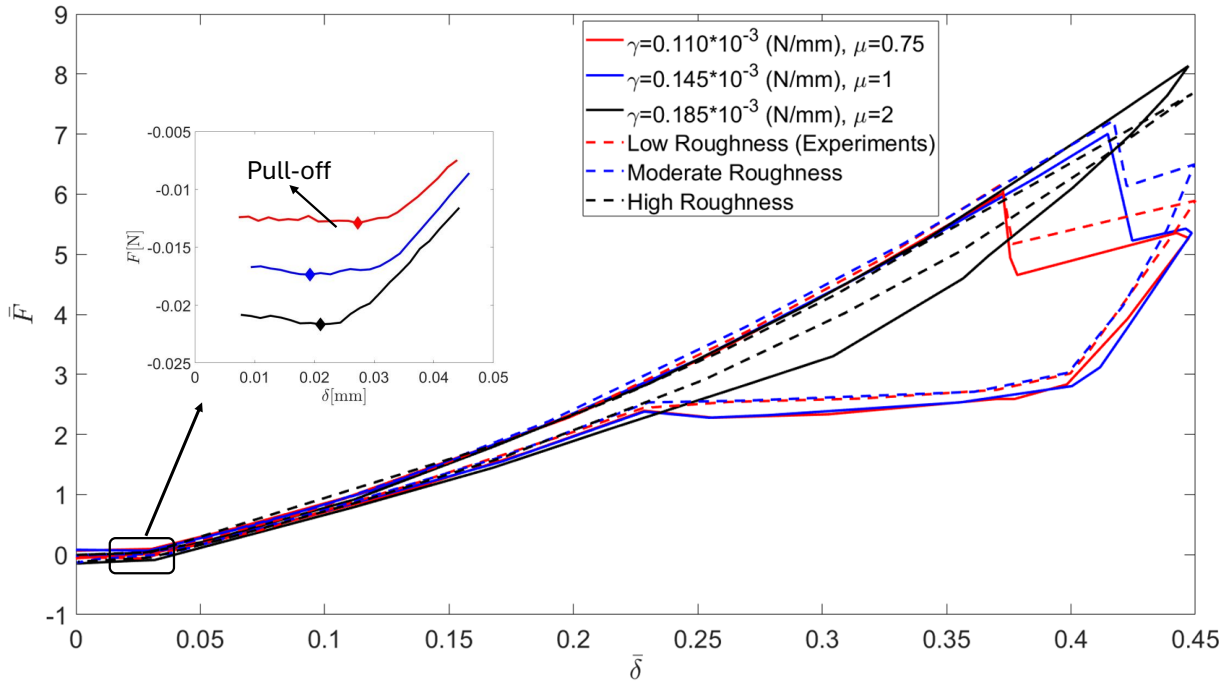

Figure 3.8: Normalized load $\bar{F} = FR/Eh^3$ as a function of normalized indentation $\bar{\delta} = \delta/R$ for different surface roughness conditions. Solid lines represent experimental data, while dashed lines correspond to numerical simulations for a radius $R = 25$ mm, a thickness $h = 0.9$ mm, and an elastic modulus $E = 1.3$ N/mm^2. An inset highlights the pull-off event used to estimate the adhesion energy γ for experimental cases.

3.4 Discussion

3.4.1 Analytical estimate of critical adhesion under frictionless conditions

It is possible to estimate analytically the magnitude of γ_c, for frictionless conditions, i.e. the critical adhesion strength above which buckling is entirely suppressed. As the shell undergoes indentation, the elastic strain energy gradually increases. The system resists deformation by storing energy in both bending and membrane (stretching) stresses, but stretching is prevalent because of the shell change of curvature. As indentation increases and the shell flattens, the stretching energy rapidly increases with the contact radius (r), where r represents the radius of the midplane of the disk-like contact area. At a critical indentation depth, the elastic strain energy reaches a threshold, leading to a sudden instability .

Upon buckling, the system undergoes a transition that involves the formation of an inverted cap and a release of stretching energy. Within the inverted cap, stretching energy becomes minimal (as in the original undeformed configuration), and instead, a localized ridge forms at the contact boundary. The size of this ridge plays a crucial role in the energy balance, where bending energy is inversely proportional to the ridge size (δ^{-2}), meaning that a smaller ridge leads to higher bending energy, while stretching energy is proportional to the ridge size (δ^2), meaning that a larger ridge increases stretching energy [178, 179].

Following [6], the stretching energy per unit area is:

$$U_{\text{stretch}} \sim Eh \left(\frac{du}{dx}\right)^2 \sim Eh \left(\frac{r}{R}\right)^4 \tag{3.6}$$

where $\frac{du}{dx}$ gives the magnitude of the strains.

Assuming stretching energy dominance, suppressing buckling requires the released stretching energy to overcome the adhesion energy. Using Eq.(3.6) the critical adhesion strength can be defined as:

$$\gamma_c \simeq Eh \left(\frac{r}{R}\right)^4 \tag{3.7}$$

From our analysis, we found that $\frac{r}{R}$ is consistently close to 0.4.

For $\gamma > \gamma_c$, adhesion provides sufficient energy to maintain a stable, unbuckled state, preventing stretching energy release. Conversely, if $\gamma < \gamma_c$ instability occurs. This theory provides an explanation for the order of magnitude of γ_c (ranging from 1 to 9×10^{-2} N/mm) observed in our simulations for frictionless cases, as we shall describe more in details in the next paragraph.

3.4.2 A general map of buckling suppression

Figure 3.9 presents a comprehensive summary of the FEM results in terms of variation of critical adhesion γ_c as a function of h/R for different values of μ. Several key observations can be drawn from this figure. Firstly, for $h/R > 0.235$, buckling is completely suppressed, irrespective of the adhesion and friction values at the interface. This can be attributed to the increased bending stiffness of thicker shells, which makes them more resistant to buckling. As a result, the mechanical response of these shells closely resembles that of bulk materials, where deformation occurs primarily through compression rather than localized buckling [6, 184, 185]. More in general, for $h/R < 0.235$, for each μ value, the critical adhesion parameter γ_c initially rises with h/R, following the increase of stretching energy implied by our estimate of Eq.(3.7), but then bending energy comes into play (which is difficult to estimate), so that γ_c reaches a peak before decreasing. The extent of the buckling zone is largest in the frictionless case ($\mu = 0$), and as μ increases, this zone contracts, highlighting the combined influence of adhesion and friction in stabilizing the shell and delaying buckling.

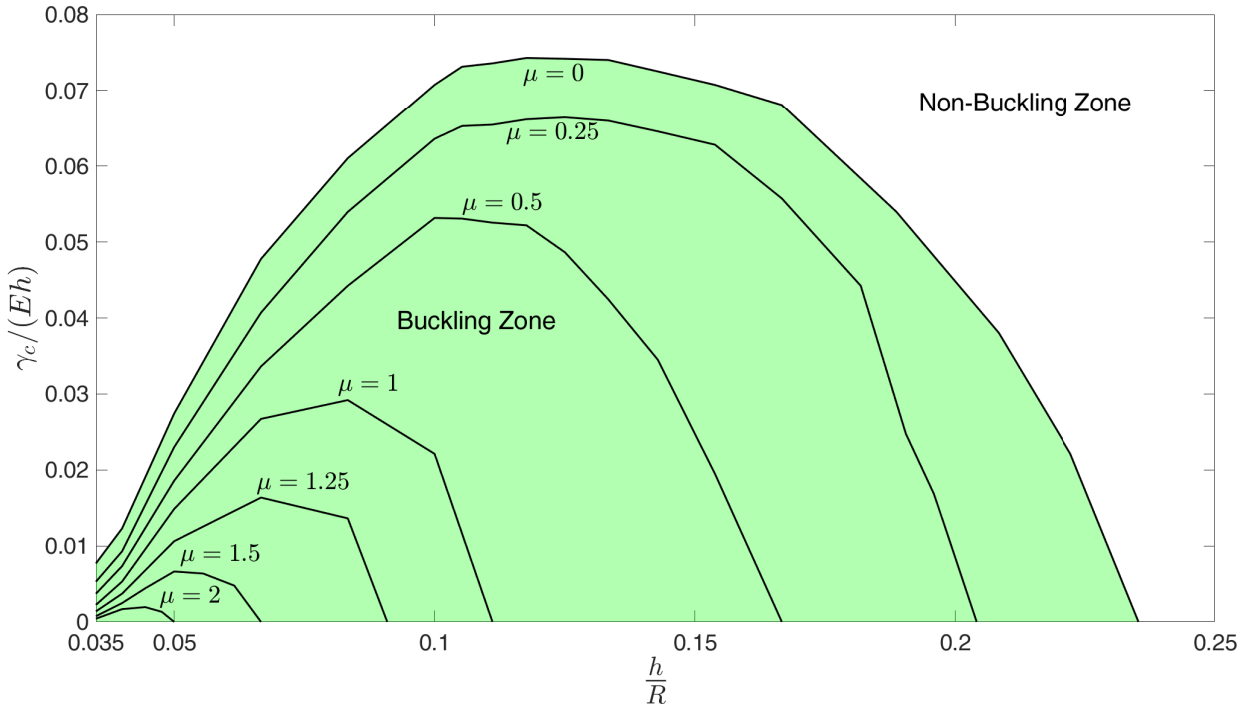

Figure 3.9: Critical adhesion γ_c/Eh versus h/R for different friction coefficients μ and $E = 1.3\,\mathrm{N/mm^2}$. The curves separate the *buckling* (below) and *non-buckling* (above) zones.

3.5 Conclusion

This study examined the combined effects of adhesion and friction on the buckling behavior of spherical shells. The results showed that the presence of adhesion and friction significantly delays buckling, ultimately leading to a critical adhesion and friction threshold, beyond which buckling is completely suppressed. Furthermore, friction had a more pronounced effect in the post-buckling regime.

By mapping the boundary between buckling and non-buckling regimes, this study highlighted the complex interplay between these factors. Additionally, a theoretical framework was introduced to define the order of magnitude of critical adhesion strength, γ_c, under frictionless conditions providing when stretching energy dominates. According to this theory and the obtained full buckling map Figure 3.9, adhesion effects were most significant for softer (E low) and thinner (h low) shells, where lower γ_c values were sufficient to suppress buckling, potentially falling within realistic adhesion strength ranges. Large friction coefficients which are often found in smooth soft contacts have also a profound influence on buckling suppression.

Experimental results exhibited agreement with numerical simulations, validating the proposed model. This work advances the understanding of how adhesion and friction influence buckling in thin shells, offering practical guidelines for designing systems in which controlling or suppressing buckling is essential.

Chapter 4

Frictional Behaviour of a Sliding Viscoelastic Cylinder with Adhesion: Influence of the Maugis–Tabor Parameter

Preface

Frictional phenomena in soft viscoelastic materials remain among the most challenging and actively investigated topics in contact mechanics and tribology. Despite decades of theoretical work and experimental research, a comprehensive understanding of the mechanisms governing friction—particularly in the presence of adhesion—is still incomplete. This is especially true for materials such as elastomers and rubbers, where the interplay between viscoelastic energy dissipation and interfacial adhesion leads to complex frictional behaviour.

In this chapter, we present a detailed investigation of the frictional response of a rigid cylindrical indenter sliding over a viscoelastic substrate in the presence of adhesive forces. The study combines a theoretical and numerical framework to capture the effects of adhesion, viscoelasticity, sliding velocity, and applied load on the overall frictional resistance. Adhesion is described using the Lennard–Jones force–separation law, while the viscoelastic substrate is modelled as a standard linear solid. By solving the resulting boundary-value problem numerically, we examine the evolution of contact pressure, surface deformation, and the friction coefficient under various conditions.

A central focus of this chapter is the role of the Maugis–Tabor parameter (λ), a dimensionless quantity that characterises the transition between short-range and long-range adhesion regimes. By systematically varying λ, together with the dimensionless normal load, sliding speed, and the ratio of relaxed to instantaneous elastic moduli, we

explore how these parameters govern the generation of friction and the relative importance of adhesive and viscoelastic contributions.

The findings presented here provide new insights into the fundamental mechanisms responsible for friction in adhesive viscoelastic contacts. They also offer guidance for interpreting experimental data and form a theoretical foundation for future investigations into more complex contact scenarios, such as those involving multiscale roughness, heterogeneous materials, or dynamic loading conditions[186].

4.1 Problem definition

Friction between two bodies in relative motion is a fundamental topic in tribology and contact mechanics, with wide-ranging implications for engineering applications such as tires, seals, soft robotics, and biomedical devices. Despite decades of theoretical studies and experimental investigations, the mechanisms that govern the frictional response of soft viscoelastic materials such as rubbers and elastomers remain incompletely understood. The complexity of the problem arises from the simultaneous contributions of multiple dissipative processes, which interact in ways that are highly dependent on material properties, loading conditions, and surface characteristics.

Early experimental work demonstrated that the coefficient of friction for rubber depends strongly on sliding velocity, applied load, and surface roughness. Schallamach [187] showed that the friction coefficient tends to increase with sliding speed and surface smoothness, but decreases with increasing load, and proposed that the frictional force is proportional to the Hertzian contact area. Subsequent studies suggested that interfacial adhesion plays a crucial role: molecular bonds at the interface continuously attach and detach during sliding, producing discontinuous motion and complex shear stress behavior [11]. Later, Schallamach [188] observed the emergence of so-called "Schallamach waves"—localized instabilities at the interface that can lead to very high frictional forces, largely independent of sliding velocity, load, or viscoelastic material properties [189].

A key advancement in the understanding of rubber friction came from the work of Grosch [190], who demonstrated a strong correlation between the viscoelastic properties of rubber and its frictional behavior. By applying the Williams–Landel–Ferry (WLF) time–temperature superposition principle [191], Grosch was able to collapse friction data into a single master curve. The shape of the friction–velocity curve was found to depend on surface conditions: for smooth surfaces, it is typically symmetric with a single peak associated with adhesive effects, whereas for rough surfaces it is asymmetric and exhibits two peaks—one attributed to adhesion at low velocity and the other to viscoelastic losses at higher speeds.

Neglecting mechanisms such as interfacial bonding–debonding or Schallamach wave propagation—which can produce friction largely independent of viscoelastic properties—

two main processes are generally recognized as dominant in soft-material friction:

I. **Bulk viscoelastic dissipation:** Hunter [83] showed that viscoelastic dissipation within the bulk of a material, for the case of a rolling cylinder, leads to a frictional response that follows a bell-shaped dependence on the logarithm of the rolling velocity v. The velocity is normalized as $v\tau/a_0$, where τ denotes the characteristic relaxation time of the viscoelastic material. The relationship can be expressed as

$$\frac{\mu_{\text{noadh}}R}{a_0} = f\left(\frac{v\tau}{a_0}, \frac{E_0}{E_\infty}\right), \tag{4.1}$$

and the maximum value occurs, for $k = E_0/E_\infty < 0.1$, at approximately (See Appendix)

$$\frac{\mu_{\text{noadh,max}}R}{a_0} \simeq 0.5. \tag{4.2}$$

Here, a_0 is the half-width of the Hertzian contact region and R is the cylinder radius. Consequently, the friction is load-dependent—it starts from zero at very low loads, increases with load, but remains relatively small since even for large deformations the ratio $a_0/R \ll 1$. Persson [87] further demonstrated that, although the pressure distribution in a viscoelastic contact may become asymmetric, Hunter's assumption of symmetrical pressure provides a valid and useful simplification.

II. **Adhesive hysteresis:** Asymmetric adhesion at the opening (trailing) and closing (leading) edges of the contact generates additional shear resistance. This asymmetry, closely linked to viscoelastic crack propagation, was first analyzed in detail by Schapery [12], Greenwood and Johnson [14], and Greenwood [192].

Adhesive effects are themselves controlled by the dimensionless Maugis–Tabor parameter λ [1, 193], which distinguishes between short-range and long-range adhesion regimes. Large values of λ (typically $\lambda > 3$) correspond to conditions where linear elastic fracture mechanics approaches are valid, whereas small λ values require cohesive zone models. Previous work on normal contact has shown that the interaction between adhesion and viscoelasticity significantly affects detachment forces, with adhesion enhancement factors approaching $1/k = E_\infty/E_0$ at high λ during rapid unloading [16, 65, 194, 195]. However, the influence of λ under sliding conditions remains largely unexplored, despite its importance in understanding frictional behavior in multiscale rough contacts.

The primary aim of this chapter is to investigate the combined effects of viscoelastic dissipation and adhesion in a controlled sliding contact configuration. Specifically, we examine how the friction coefficient depends on four key dimensionless parameters: the Maugis–Tabor parameter λ, the dimensionless normal load W, the dimensionless sliding velocity V, and the ratio of relaxed to instantaneous moduli $k = E_0/E_\infty$. By analyzing

the role of each parameter, we aim to provide deeper physical insight into the mechanisms governing friction in adhesive viscoelastic contacts and to offer theoretical tools for interpreting experimental results.

4.2 Problem Statement and Model Definition

4.2.1 System Configuration and Assumptions

To investigate the combined influence of adhesion and viscoelasticity on friction, we consider a canonical contact problem: a rigid cylindrical indenter of radius R slides at a constant velocity v over a flat, frictionless half-space composed of a linear viscoelastic material. Adhesive interactions at the interface are described using a Lennard–Jones (LJ) force–separation law, and the viscoelastic substrate is modeled as a standard linear solid. The contact configuration is illustrated schematically in Figure 4.1.

The static version of this contact problem (i.e., without sliding) has been solved previously by Wu [196]. In this work, the formulation is extended to include steady-state sliding motion and adhesive interactions. The solution is obtained numerically using a boundary element method (BEM), which enables the computation of interfacial pressures and displacements while accounting for both viscoelastic material behavior and adhesion.

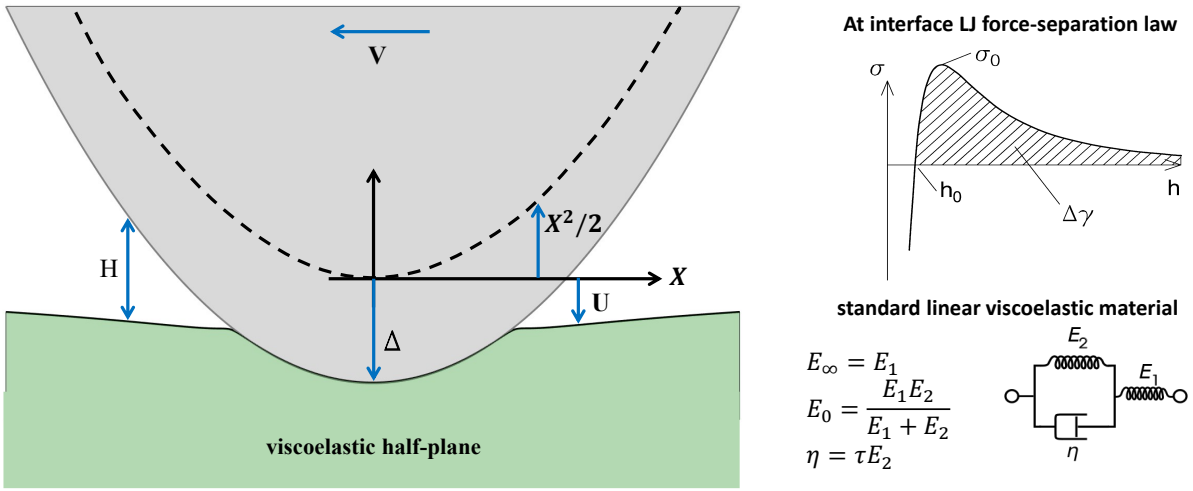

Figure 4.1: Schematicrepresentationof theproblemconsidered.

4.2.2 Adhesive Interaction and Gap Function

The adhesive pressure $p(h)$ as a function of the local separation h between the two surfaces follows the Lennard–Jones law:

$$p(h) = -\frac{8\Delta\gamma}{3\varepsilon}\left[\left(\frac{\varepsilon}{h}\right)^3 - \left(\frac{\varepsilon}{h}\right)^9\right] \tag{4.3}$$

where ε is the equilibrium separation distance, and $\Delta\gamma = \alpha\sigma_0\varepsilon$ is the surface energy. Here, σ_0 is the cohesive (theoretical) strength, and $\alpha = \dfrac{9\sqrt{3}}{16} \approx 0.9743$.

The local gap function between the rigid cylinder and the viscoelastic substrate is written as:

$$h(x) = -\delta + \varepsilon + \frac{x^2}{2R} + u_z(x, v) \tag{4.4}$$

where δ is the indentation depth (positive when the indenter approaches the surface) and $u_z(x, v)$ is the vertical displacement of the viscoelastic substrate, which depends on both position x and sliding velocity v.

It is convenient to define an adhesive length scale β as:

$$\beta = \left(\frac{R^2\Delta\gamma}{E_0^*}\right)^{1/3} \tag{4.5}$$

where $E_0^* = \dfrac{E_0}{1-\nu^2}$ is the relaxed plane-strain modulus of the viscoelastic substrate, E_0 is the relaxed modulus, and ν is Poisson's ratio.

4.2.3 Non-Dimensional Formulation

To simplify the governing equations and improve numerical stability, we express them in dimensionless form by introducing the following normalized variables:

$$\Delta = \frac{\delta R}{\beta^2}, \quad H = \frac{\dfrac{h}{\varepsilon} - 1}{\dfrac{\beta^2}{R\varepsilon}}, \quad X = \frac{x}{\beta}, \quad P = \frac{p}{\sigma_0}, \quad U = \frac{u_z R}{\beta^2}, \quad W = \frac{w}{(E_0^* R\Delta\gamma^2)^{1/3}} \tag{4.6}$$

With these definitions, the gap function becomes:

$$H = -\Delta + \frac{X^2}{2} + U(X, V) \tag{4.7}$$

and the dimensionless adhesive pressure is written as:

$$P(H) = -\frac{3\sqrt{3}}{2}\left[\frac{1}{(\alpha H\lambda + 1)^3} - \frac{1}{(\alpha H\lambda + 1)^9}\right] \tag{4.8}$$

Here, λ is the Maugis–Tabor parameter, defined as:

$$\lambda = \sigma_0\left(\frac{R}{\Delta\gamma E_0^{*2}}\right)^{1/3} \tag{4.9}$$

This dimensionless parameter characterizes the transition between short-range and long-range adhesion regimes [32, 33].

4.2.4 Numerical Solution Method

To determine the solution of the contact problem, the boundary element method (BEM) is employed, following the implementation of Papangelo and Ciavarella [197, 198], but suitably modified for the present analysis. The domain, of total length L, is discretized into M equally spaced elements of size $2a = L/M$, corresponding to $N = M$ interfacial nodes.

To compute the nodal deflections, the analytical solution derived by Afferrante and Carbone [199] for a constant-pressure element of width $2a$ moving steadily at velocity V over a viscoelastic half–plane is adopted:

$$\begin{aligned} U(X,V) = -\frac{2\lambda P}{\pi}\Bigg\{ & \frac{\pi}{2}D - \frac{k}{2}\Big[(X+A)\ln\left(\frac{X+A}{A}\right)^2 - (X-A)\ln\left(\frac{X-A}{A}\right)^2\Big] \\ & + \frac{(1-k)}{2}\Big[2V\exp\left(\frac{X+A}{V}\right)\mathrm{Ei}\left(-\frac{X+A}{V}\right) - (X+V+A)\ln\left(\frac{X+A}{A}\right)^2\Big] \\ & - \frac{(1-k)}{2}\Big[2V\exp\left(\frac{X-A}{V}\right)\mathrm{Ei}\left(-\frac{X-A}{V}\right) - (X+V-A)\ln\left(\frac{X-A}{A}\right)^2\Big]\Bigg\}, \end{aligned} \tag{4.10}$$

where $A = a/\beta$, $V = V\tau/\beta$, $k = E_0/E_\infty$, $\mathrm{Ei}(\cdot)$ denotes the exponential integral function, and $D = d/\beta$ is an arbitrary constant used to set the datum of the displacement field. This constant arises from the well–known logarithmic singularity at infinity in the displacement produced by a point load acting on a half–plane. If one wishes the displacement field to vanish at a particular coordinate $X = X_0$, then D is determined as

$$\begin{aligned} D = {} & \frac{2(1-k)}{\pi}V\exp\left(\frac{X_0-A}{V}\right)\left[\mathrm{Ei}\left(\frac{A-X_0}{V}\right) - \exp\left(\frac{2A}{V}\right)\mathrm{Ei}\left(-\frac{A-X_0}{V}\right)\right] \\ & + \frac{1}{\pi}\big(A-(1-k)V-X_0\big)\ln\left(\frac{X_0-A}{A}\right)^2 + \frac{1}{\pi}\big(A+(1-k)V+X_0\big)\ln\left(\frac{X_0+A}{A}\right)^2. \end{aligned} \tag{4.11}$$

The fundamental solution used to derive the influence matrix depends on the choice of this datum point. As a consequence, the load–displacement curves may shift if the datum point is changed. Alternatively, one may plot the relation between the total load W and the gap at $H(X = 0)$, which remains independent of the chosen constant D. In the present work, without loss of generality, we set $D = 0$, which corresponds to selecting the datum such that the displacement field vanishes at $X = X_0$. Therefore, X_0 becomes the reference coordinate at which $U(X_0, V) = 0$, and all remaining displacement values are expressed relative to this point.

By applying the superposition principle, Eq. (4.10) is used to build the influence matrix $[G]_{N\times N}$, whose j-th column represents the displacement field generated by a unit

element pressure moving steadily over a viscoelastic half–plane and applied at node j, while all other nodes remain unloaded. Accordingly, the vector of nodal deflections can be expressed as

$$\{U\}_{N\times 1} = \left(\frac{2\lambda}{\pi}\right)[G]_{N\times N}\{P\}_{N\times 1}. \tag{4.12}$$

The overall contact problem is nonlinear because the interfacial tractions P depend on the separation H through the Lennard–Jones potential. The coupled equations (4.12), (8), and (9) are solved numerically using a Newton–Raphson iterative scheme implemented in MATLAB. For low values of λ, convergence was achieved with $N = 401$ nodes. However, for higher values ($\lambda > 3$), the number of nodes was increased up to $N = 1201$ to ensure adequate resolution of the pressure peaks occurring near the leading and trailing edges of the contact zone.

4.2.5 Calculation of the Friction Coefficient

The evaluation of the friction coefficient is a fundamental step in the analysis of sliding adhesive viscoelastic contacts. In the absence of adhesion, the classical solution for the frictional response of a rigid cylinder sliding over a viscoelastic half-space was derived by Hunter [200] and later simplified by Persson [87]. Their results provide a useful reference for validating the present approach and for quantifying the additional contribution due to adhesion. In their formulation, the friction coefficient for the adhesiveless case is expressed as:

$$\mu_{\text{noadh}} = \frac{a_0}{R} f\left(\frac{v\tau}{a_0}, k\right) = \sqrt{\frac{4W}{\pi}}\left(\frac{\sigma_0}{\lambda E_0^*}\right) f\left(\frac{v\tau}{a_0}, k\right) \tag{4.13}$$

where $f(v\tau/a_0, k)$ is a function derived from the Hunter–Persson solution, a_0 is the Hertzian contact half-width in the absence of adhesion, and E_0^* is the relaxed plane-strain modulus.

In the limit of large loads (where adhesive effects are negligible), the solution approaches a "bell-shaped" response governed by the function $f(v\tau/a_0, k)$. For this reason, it is convenient to define the scaled friction coefficient:

$$\mu^* = \mu\frac{R}{a_0} = \frac{\mu}{\sqrt{\frac{4W}{\pi}}\left(\frac{\sigma_0}{\lambda E_0^*}\right)} \tag{4.14}$$

which, under adhesiveless conditions and for $k < 0.1$, has a typical maximum value of approximately 0.5.

In the numerical solution of the adhesive contact problem, once the pressure $p(x)$ and displacement fields $u(x)$ are obtained for a given load, the friction coefficient is computed

as:

$$\mu = -\frac{1}{w}\int p(x)\frac{du}{dx}\,dx = -\frac{1}{W}\sqrt{\frac{\lambda^3}{\alpha}\frac{\varepsilon}{R}}\int P(X)\frac{dU}{dX}\,dX \tag{4.15}$$

and the dimensionless friction coefficient becomes:

$$\mu^* = \mu\frac{R}{a_0} = -\sqrt{\frac{\pi}{2}}\frac{\lambda}{W^{3/2}}\int P(X)\frac{dU}{dX}\,dX \tag{4.16}$$

This form depends only on the four governing dimensionless parameters:

- Maugis parameter λ,
- Dimensionless load W,
- Dimensionless sliding speed V_0,
- Modulus ratio $k = E_0/E_\infty$.

Thus, the friction coefficient can be expressed as a general function:

$$\mu^* = g(V_0, \lambda, W, k) \tag{4.17}$$

where the dimensionless sliding speed is given by:

$$V_0 = \frac{v\tau}{a_0} = \frac{1}{2}\sqrt{\frac{\pi}{W}}\frac{v\tau}{\beta} \tag{4.18}$$

We begin our analysis with a representative case of $k = 0.1$, which fixes the elastic contrast. Accordingly, the problem can be conveniently parameterized in terms of three dimensionless quantities, namely V_0, λ, and W, noting that V_0 is itself a function of W through Eq. (4.18).

4.3 Results

4.3.1 Dependence on the Normal Load, Maugis Parameter, and Sliding Velocity

We begin by examining the influence of sliding velocity on the interfacial pressure distribution and its implications for adhesive viscoelastic contact. Figure 4.2 (a-b) show the dimensionless pressure distribution $P(X)$ for a fixed load $W = 1$ and two representative values of the Maugis–Tabor parameter: $\lambda = 4$ (short-range adhesion) and $\lambda = 0.1$ (long-range adhesion), respectively. In each case, the results are presented for a range of dimensionless sliding velocities V_0.

The results reveal that the pressure distribution remains essentially symmetric at both very low and very high sliding velocities. These two limits correspond, respectively, to the adhesive contact solutions under relaxed and instantaneous elastic moduli, where viscoelastic energy dissipation is negligible. In contrast, at intermediate velocities, the pressure distribution becomes distinctly asymmetric, reflecting the combined effects of viscoelasticity and adhesion.

This asymmetric behavior is more pronounced for larger values of λ, i.e., when adhesion is stronger and acts over shorter ranges. In the case of low λ (long-range adhesion), the adhesive pressure spikes at the leading and trailing edges ($P < 0$) are relatively mild, corresponding to weaker interfacial forces. However, for high λ, the interfacial behavior is significantly richer. In particular, around $V_0 \approx 1$ — a velocity range corresponding to the characteristic relaxation time of the viscoelastic substrate — the pressure profile becomes highly asymmetric, featuring two distinct adhesive spikes and an additional compressive peak near the leading edge induced by viscoelastic effects.

A key observation in this transitional regime is that the adhesive spike at the trailing edge (on the right-hand side, where the interface is opening) is considerably larger than the corresponding spike at the leading edge (on the left, where the interface is closing). This asymmetry is consistent with theoretical predictions for viscoelastic crack propagation, in which crack opening and closing events are governed by markedly different energy dissipation mechanisms. The enhanced adhesive stress at the trailing edge plays a crucial role in the overall frictional response and is a direct manifestation of the coupling between adhesion and viscoelastic dissipation.

4.3.2 Effect of the Maugis Parameter on Adhesive Regimes, Pressure Response, and Deformation

The influence of the Maugis–Tabor parameter λ on the interfacial contact mechanics is illustrated in Figure 4.3, where three representative cases are shown: $\lambda = 0.1$, $\lambda = 1$, and $\lambda = 3$, all at a constant dimensionless load $W = 0.1$. The rigid cylindrical indenter slides from right to left across the viscoelastic substrate at dimensionless velocities $V_0 =$ 13.73, 4.28, and 2.73, respectively. In each case, the upper row of the figure presents the deformed configuration of the viscoelastic surface, while the lower row shows the corresponding dimensionless pressure distribution $P(X)$.

The results demonstrate that the magnitude of λ strongly influences both the pressure distribution and the deformation profile of the viscoelastic substrate:

- **Low adhesion ($\lambda = 0.1$):** At low values of λ, corresponding to relatively stiff materials with weak adhesive interactions, the contact is dominated by compressive tractions. The pressure distribution exhibits only mild asymmetry, and the adhesive contributions are relatively small compared to the compressive stresses

(Figures 4.3(a-d)). The deformation remains nearly symmetric, and the adhesive spikes at the edges are broad and shallow.

- **Intermediate adhesion ($\lambda = 1$):** At intermediate values of λ, both the pressure distribution and the deformation become markedly asymmetric (Figures 4.3(b-e)). The contact line shifts noticeably towards the leading edge, indicating a pronounced eccentricity ($|a_l| > |a_t|$). A distinct compressive spike emerges near the leading edge, caused by enhanced viscoelastic resistance in this region. Adhesive tractions are significantly stronger than in the low-λ case, leading to a more complex interplay between compression and adhesion.

- **High adhesion ($\lambda = 3$):** When adhesion is strong (large λ), compressive and tensile tractions become comparable in magnitude (Figures 4.3(c-f)). The adhesive spikes become sharp and intense, with the trailing-edge peak being broader than that at the leading edge. Despite the presence of a compressive peak that maintains the pressure asymmetry, the contact eccentricity now shifts towards the trailing edge ($|a_t| > |a_l|$). This shift highlights the increased contribution of adhesive tractions to the total frictional resistance at higher λ values.

Overall, these results show that increasing the Maugis parameter not only enhances the magnitude of adhesive forces but also affects the size and distribution of the contact zone.. The transition from compression-dominated to adhesion-dominated behavior is accompanied by significant changes in contact asymmetry, pressure distribution, and surface deformation, all of which play a crucial role in determining the overall frictional response.

4.3.3 Spatial Distribution of Frictional Resistance

It is insightful to examine how the frictional resistance is distributed along the contact interface. To this end, Figure 4.4 shows the variation of the quantity

$$-\frac{\sqrt{\pi\lambda}}{2W^{3/2}}P(X)\frac{dU}{dX},$$

which, when integrated over the entire interface, gives the dimensionless friction coefficient μ^* (see Eq.4.16). The results are presented for a load of $W = 0.1$ and for different values of $\lambda = [0.1, 1, 2, 3]$.

Several observations can be made:

(i) The primary contribution to the frictional resistance originates near the contact edges.

(ii) For small λ, the leading edge provides a larger contribution than the trailing edge, whereas for $\lambda > 1$, the dominant contribution arises from the trailing edge.

(iii) A slight negative contribution appears just ahead of the leading edge due to adhesive interactions, which tend to reduce the overall frictional resistance; however, this effect is negligible for the geometry considered.

(iv) The contribution from the central region of the contact area remains relatively small and only weakly sensitive to λ. Due to reverse sliding in this zone, the local shear traction contributes negatively to the net friction force; however, its magnitude is noticeably smaller than the positive contributions arising at the leading and trailing edges, so that the overall friction remains dominated by edge effects.

These findings confirm that the dominant contribution to the total frictional resistance in adhesive viscoelastic contacts arises from localized processes at the contact edges, particularly near the trailing edge under conditions of strong adhesion. The asymmetry of these contributions, and their dependence on λ, is a direct manifestation of the interplay between viscoelastic dissipation and adhesive crack dynamics.

4.3.4 Velocity Dependence of the Friction Coefficient and Contributions from Adhesive and Compressive Stresses

The dependence of the dimensionless friction coefficient $\mu^* = \mu R/a_0$ on the sliding velocity V_0 is shown in Figure 4.5 (panels a–h) for three representative values of the Maugis–Tabor parameter: $\lambda = 0.1$ (panels a–c), $\lambda = 1$ (panels d–f), and $\lambda = 3$ (panels g–h). Results are presented for different dimensionless loads $W = 0.1$, 1, 10. In each plot, the black curve represents the total friction coefficient calculated from Eq.4.16, while the red and blue curves represent the adhesive (μ_{adh}) and compressive (μ_{comp}) contributions, respectively. These contributions are obtained by integrating Eq.4.16 considering only the tensile or compressive stress components.

Across all cases, the total friction coefficient exhibits a characteristic bell-shaped dependence on sliding velocity. It reaches a maximum at intermediate velocities around $V_0 \approx 1$, where viscoelastic dissipation is most significant. This behavior is consistent with classical viscoelastic friction models and highlights the dominant role of time-dependent energy dissipation in determining the frictional response.

Several important trends emerge from the results:

(i) **Dominance of compressive stresses at high load:** At large loads, the compressive component μ_{comp} dominates the total frictional response, and the overall friction magnitude is significantly reduced. In this regime, the solution converges

to the classical Persson model (see Appendix), thereby validating the present numerical approach.

(ii) **Adhesive contribution and dependence on λ:** For a given load, the total friction coefficient μ^* increases strongly with the Maugis parameter. At low loads, adhesive effects tend to dominate the frictional response, particularly for $\lambda > 1$. In contrast, for low λ, the adhesive contribution remains relatively small compared to the compressive component. Interestingly, the adhesive contribution can become negative over certain high-velocity ranges, meaning that the adhesive tractions act in the direction of motion rather than opposing it, as typically observed in classical friction.

(iii) **Load dependence of peak position:** The velocity corresponding to the peak friction coefficient, as well as those of its individual components, shifts to higher V_0 values at lower loads. This phenomenon can be explained by the fact that the actual adhesive contact area is significantly larger than the Hertzian prediction. As previously noted by Wu [196] for the static case, using the actual contact area in the definition of V_0 would bring the location of the peak much closer to unity.

(iv) **Combined influence of load and adhesion:** Overall, the maximum value of the friction coefficient is highly sensitive to both the Maugis parameter and the applied load. Adhesion enhances the total friction level, especially at low loads, while compressive forces become dominant under heavy loading conditions.

These results emphasize that the observed frictional behavior arises from the complex interplay between viscoelastic dissipation, adhesive forces, and normal loading conditions. The relative magnitude and velocity dependence of the adhesive and compressive contributions provide valuable insights into the mechanisms controlling friction in adhesive viscoelastic contacts.

4.3.5 Convergence of the Friction Coefficient with the Maugis–Tabor Parameter

To explore how the friction coefficient converges with the Maugis–Tabor parameter λ, we plot in Figure 4.3.5-a the maximum value of μ^*_{tot} (black line) as a function of λ for a fixed load $W = 0.1$ and $k = 0.1$. The convergence of the maxima of μ^*_{adh} and μ^*_{comp} is also shown as red and blue lines, respectively.

It is evident that the convergence with respect to the Maugis parameter is very slow — much slower than what is typically observed in standard studies on pull-off in normal adhesion. Therefore, careful consideration of the Maugis–Tabor parameter is essential in friction calculations. For low λ, the primary contribution to friction is due to compressive

pressure. Around $\lambda \approx 1$, a crossover occurs where the adhesive contribution becomes dominant over the compressive part.

By increasing the number of interfacial elements up to $M = 1201$, we traced the evolution of $\max(\mu^*)$ up to $\lambda = 24$, where we found $\mu^*_{\text{tot}} \gtrsim 215$, slowly approaching its theoretical maximum value

$$\mu^* = \frac{\pi^{1/2}}{2W^{3/2}k} \approx 280$$

(see the discussion paragraph on the JKR theoretical limit for large λ). In the low-λ regime, the friction coefficient scales as $\mu^* \propto \lambda^{5/4}$, as shown by the grey dashed line.

Since Figure 4.3.5-a refers to a given normal load ($W = 0.1$), Figure 4.3.5-b explores the dependence of $\max(\mu^*_{\text{tot}})$ on the normal load for several Maugis parameters ($\lambda = [0.1, 0.5, 1, 3]$). We observe that $\max(\mu^*_{\text{tot}})$ increases with λ; however, up to a dimensionless load of approximately $W \approx 1$, it scales as $\mu^* \propto W^{-4/3}$, regardless of λ.

At higher loads, all curves converge to the adhesionless solution, which, based on the Persson–Hunter solution (see Appendix) and $k = 0.1$, is approximately $\mu^*_{\text{tot}} \approx 0.48$. This limit is achieved only at very high loads ($W \approx 100$), corresponding to a very large contact semi-width in extremely soft materials — a condition that also limits our ability to explore large normal loads for high λ.

Interestingly, for $\lambda = 0.1$, we observe a non-monotonic behaviour.

Finally, we examine how the maximum dimensionless friction coefficient, $\max(\mu^*_{\text{tot}})$, depends on the material parameter

$$k = \frac{E_0}{E_\infty}$$

which represents the ratio of the relaxed modulus E_0 to the instantaneous modulus E_∞ of the viscoelastic substrate. This analysis is performed for a fixed Maugis parameter $\lambda = 3$ and dimensionless load $W = 0.1$. The results are presented in Figure 4.7.

The results reveal a clear and physically intuitive trend. In the purely elastic limit ($k = 1$), where no viscoelastic relaxation occurs, the maximum friction coefficient approaches zero. As k decreases from unity, $\max(\mu^*_{\text{tot}})$ rises sharply, indicating a strong enhancement of friction due to viscoelastic energy dissipation. This increase reflects the growing capacity of the material to dissipate energy through internal relaxation mechanisms as the contrast between E_0 and E_∞ becomes more pronounced.

For $k \approx 10^{-3}$, the maximum friction coefficient saturates and becomes nearly independent of further decreases in k. This behavior suggests that for typical elastomeric materials — which often exhibit k values on the order of 10^{-3} — the friction coefficient is effectively insensitive to the precise ratio of relaxed to instantaneous modulus. In other words, once the viscoelastic contrast exceeds a certain threshold, the dissipation processes governing friction reach a limiting state, and additional softening has little effect on the maximum attainable friction.

This result has important implications for the design and selection of soft materials in

tribological applications. It indicates that beyond a certain level of viscoelasticity, further reductions in k do not yield significant frictional enhancement, implying that other factors (such as adhesion range or surface energy) become more critical in controlling frictional behavior.

4.4 Discussion

As discussed in the introduction, rubber friction is a highly complex problem, and most current models rely on semi-empirical equations, particularly to account for the role of adhesion. Experimental findings are not always straightforward to interpret. For example, [190] reported two friction peaks: one attributed to adhesion and the other to viscoelastic losses. However, this observation was made for a silicon carbide rough surface, not for a smooth one. Indeed, for a smooth interface, [190] measured a rather symmetric bell-shaped friction curve with a single peak, which is in qualitative agreement with our results.

For a sliding smooth sinusoidal surface, Carbone et al. [132] reported two friction peaks and suggested that this could explain Grosch's observations on rough surfaces. However, in our numerical simulations, we never observed two peaks in the friction curve for the smooth-surface model. It would be useful to understand why an adhesion-related peak appears in Grosch's rough-surface experiments. Our model predicts that, at the asperity level, the Maugis–Tabor parameter is likely very low, resulting in negligible adhesion effects. Conversely, for a wavy smooth surface, where the Maugis–Tabor parameter is likely much larger, adhesion dominates, leading to a single adhesion-related peak since dissipation due to viscoelastic losses is relatively small compared to the adhesive component. On rough surfaces, adhesion contributions become comparable to viscoelastic losses, but our model does not currently include sufficient mechanisms to accurately describe rough contact.

It is instructive to compare our results with those of Carbone et al. [132] and Mandriota et al. [201]. These authors separate the symmetric and antisymmetric terms in the Green's function, recognizing that the symmetric terms correspond to elastic energy, while the antisymmetric terms lead to dissipation. This dissipation increases the effective work of adhesion at the trailing edge and decreases it at the leading edge. Their theory solves the contact problem using a fully energetic approach reminiscent of the JKR limit, which is typically applied in elastic adhesive problems for large values of the Maugis–Tabor parameter λ. One might therefore expect that our model approaches this same limit for large λ, even though it applies across all λ.For increasing values of λ, the cohesive zone progressively shrinks and the adhesive interaction approaches the classical JKR asymptotic regime. In this limit, the model is theoretically expected to converge toward the viscoelastic JKR scaling obtained by Carbone and Mandriota. Although our

numerical simulations do not reach a sufficiently large λ to observe full saturation of this limit—due to the rapidly narrowing cohesive zone and the associated numerical resolution requirements—the trend observed in Fig. 4.6(a) is fully consistent with the approach to this asymptotic behavior.

However, a viscoelastic adhesive contact problem is essentially a viscoelastic crack problem. The seminal work of Graham [202] suggested that any energy balance approach must include some description of coupling, over a finite length scale, with microscale separation processes [203]. In other words, a finite length scale associated with a cutoff adhesive stress σ_c is required, as in the Persson and Brener [131] theory for a semi-infinite crack, or a representative cohesive stress as in the model of Schapery [204]. Indeed, in the next chapter, our numerical solution will be fully validated against the Persson and Brener theory in the low sliding speed regime. It can be shown that the friction force due to adhesion increases with the Maugis–Tabor parameter , until it reaches the limiting value:

$$\frac{f_T(v)}{\Delta\gamma} \approx \frac{E_\infty}{E_0}, \tag{4.19}$$

When the sliding speed is very high, the characteristic length scale that resolves the Graham [202] paradox becomes the size of the contact area itself, and the friction coefficient assumes the well-known decaying bell shape. At such high speeds, the loading frequency is so high that the rubber is in a glassy state near the crack tips.

In Fig. 4-6(a), the maximum friction coefficient as a function of the Maugis parameter numerically approaches the limit given by Eq.4.19 for very large λ, with only small discrepancies due to numerical difficulties associated with sharp pressure spikes. For this reason, we cannot fully compare our results with those of Carbone et al. [132] and Mandriota et al. [201], since it is unclear which value of λ in our model would correspond to theirs. Regarding Fig. 11a in Mandriota et al., in our notation these results correspond to $W = 4.93$–28.2. In terms of maximum friction coefficient, this range is located at the far right of our Fig. 4-6(b), where the friction coefficient is of the same order as the adhesionless value, consistent with Mandriota et al. However, we do not expect our full curves at low speed to match theirs due to the reasons discussed above.

The experiments of Barquins and Roberts [13], which focused on smooth large spheres (rather than cylinders) sliding on smooth surfaces, reported significantly higher friction for larger sphere sizes. However, rate effects were relatively small compared to predictions based purely on the increase of Hertzian contact area. This may be due to the presence of adhesive shear stresses at the interface arising from the Schallamach mechanism described in the introduction, rather than viscoelastic dissipation, which produces much smaller friction coefficients.

In industrially relevant cases, such as rubber sliding on rough surfaces, earlier studies [205] often neglected the role of adhesion, preventing the appearance of the adhesion-

related "peak." On rough surfaces, where Grosch clearly measured two friction peaks, modeling approaches remain largely semi-empirical. These are typically based on the Schallamach mechanism or on the attaching–detaching of rubber chains, which leads to a velocity-dependent shear stress . These approaches add an adhesive contribution to the viscoelastic one, both of which depend on the challenging task of defining asperity size. Lang and Klüppel [206] also used a semi-empirical model for the adhesive contribution, while Hentschke and Plagge [207] proposed a completely different approach based on scaling laws. To our knowledge, the work of Plagge and Hentschke [17] represents one of the few published attempts to model rubber friction on rough surfaces while accounting for both viscoelasticity and adhesion. Their model captures an adhesion-related friction peak at low velocities, where viscoelastic losses are typically dominant. It is also worth noting that the doctoral work of Bugnicourt [208], together with related studies by Sainsot and co-authors, developed a numerical framework for simulating rough-surface contact in viscoelastic materials with frictional dissipation. While their formulation primarily focuses on roughness-induced viscoelastic losses and does not explicitly incorporate the adhesive mechanisms considered in our approach, it represents another significant contribution toward the broader goal of integrating adhesion, viscoelasticity, and surface roughness in friction models.

4.5 Conclusion

In this chapter, we have presented a comprehensive study of sliding friction between a rigid cylinder and a viscoelastic half-plane, incorporating the effects of adhesion via a Lennard-Jones potential. Using a boundary element method and a dimensionless formulation, we systematically investigated how friction evolves with sliding speed, load, material rheology, and adhesive interaction strength.

A key outcome of this work is the identification of the pivotal role played by the Maugis parameter λ, which governs the range and intensity of adhesive forces. We demonstrated that λ critically controls both the asymmetry in pressure distribution and the frictional response of the interface. At low λ, the system behaves more like a purely elastic contact with negligible adhesive contributions. In contrast, high λ induces strong edge-localized adhesion, leading to significant energy dissipation and highly asymmetric stress profiles.

Our results further reveal that: The friction coefficient exhibits a non-monotonic, bell-shaped dependence on the dimensionless sliding speed V_0, in qualitative agreement with experimental observations such as those by Grosch and Barquins. The frictional force is primarily generated at the edges of the contact zone, with the trailing edge becoming dominant at high λ due to viscoelastic crack propagation dynamics. The transition from bulk dissipation to edge-dominated friction can be tuned by modifying the viscoelastic contrast k, the applied load W, and the adhesive parameter λ. In the limiting case of high

λ, the solution converges toward a JKR-like regime, highlighting the model's consistency with classical adhesive contact mechanics.

The novelty of this study lies in quantitatively linking the adhesive length scale λ to frictional asymmetry and viscoelastic dissipation in sliding contacts, offering a more unified view of frictional behavior across short- and long-range adhesive regimes.

This framework not only deepens our understanding of viscoelastic adhesive friction but also provides a predictive tool for analyzing complex soft contact interfaces in applications ranging from biomimetics to soft robotics and medical devices.

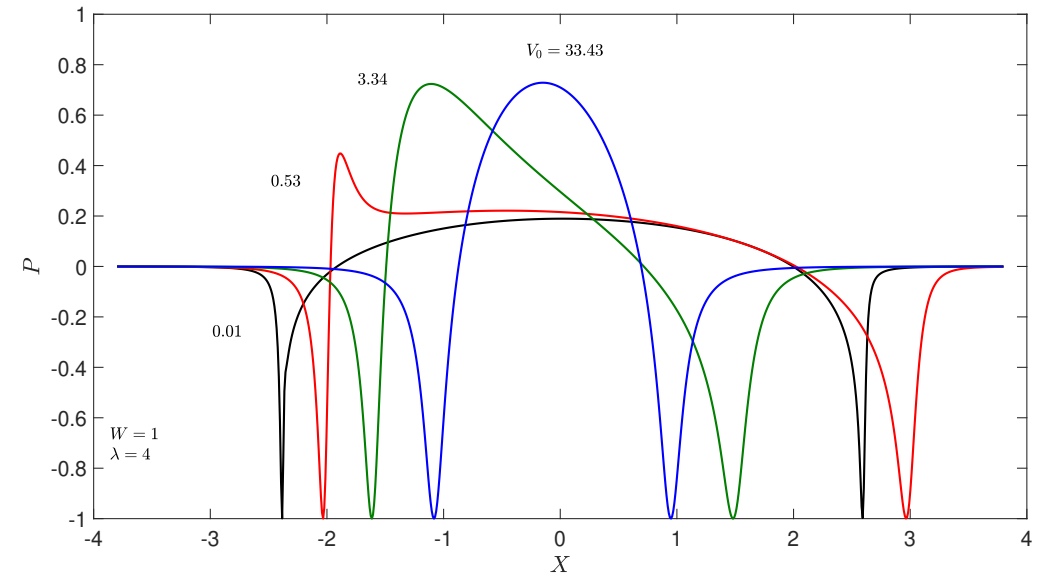

(a)

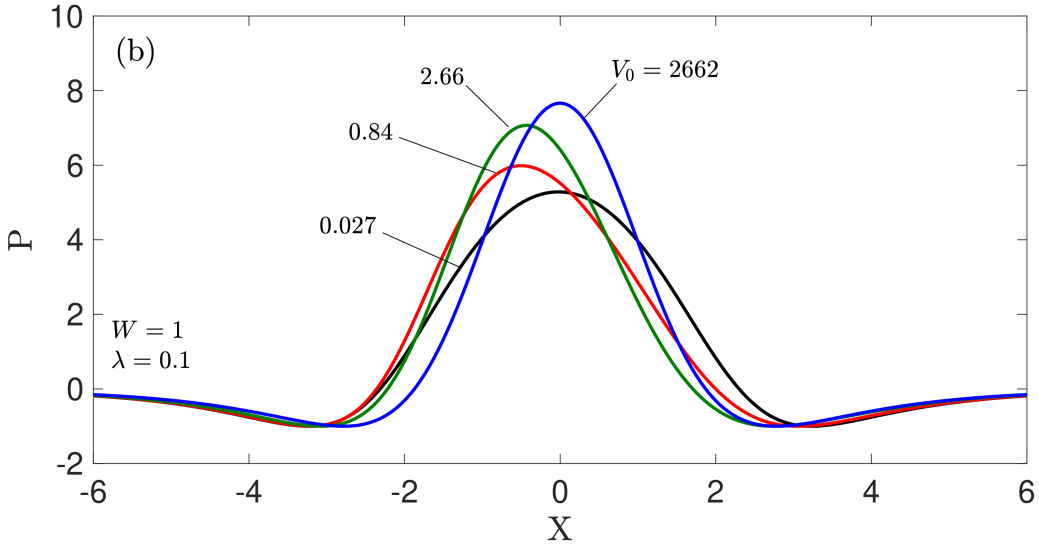

(b)

Figure 4.2: Pressure distribution at the interface for (a) $\lambda = 4$ and $V_0 = [4.21 \times 10^{-4}, 0.53, 3.34, 420.87]$, and (b) $\lambda = 0.1$ and $V_0 = [0.027, 0.84, 2.66, 2662]$. In both panels, $W = 1$ and $k = 0.1$.

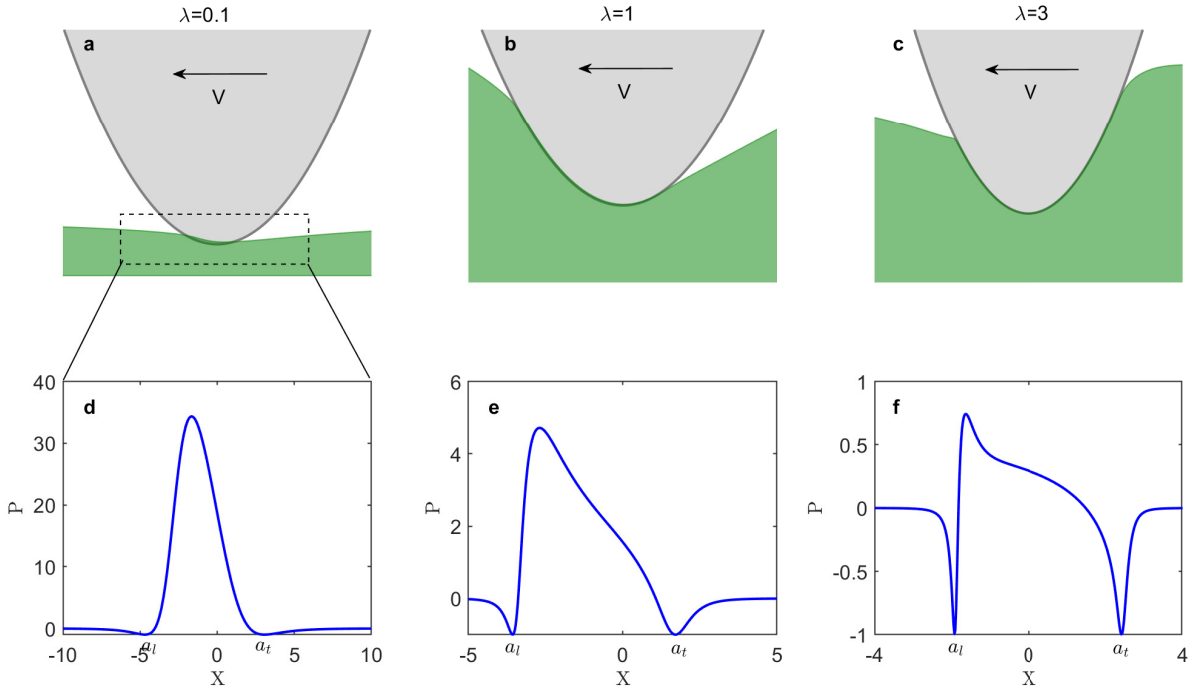

Figure 4.3: Effect of the Maugis–Tabor parameter λ on contact deformation and pressure distribution. Three representative cases are shown: $\lambda = 0.1$ (a,d), $\lambda = 1$ (b,e), and $\lambda = 3$ (c,f) for a constant load $W = 0.1$ and sliding from right to left. The top row shows the deformed configuration, while the bottom row shows the corresponding pressure profiles.

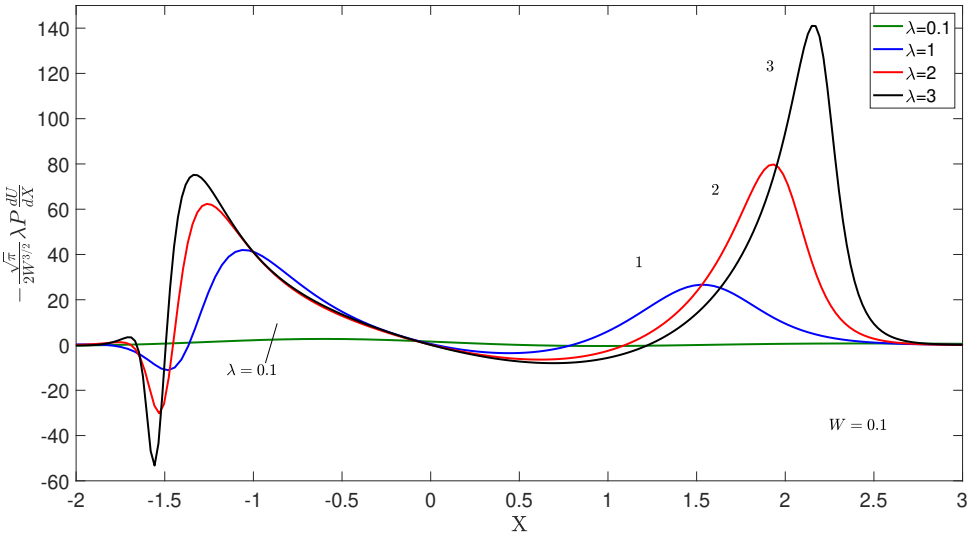

Figure 4.4: The quantity $-\frac{\sqrt{\pi}\lambda}{2W\sqrt{2}}\,P(X)\,\frac{dU}{dX}$, which represents the local contribution to the frictional resistance (see Eq. (4.16)), is shown along the interface for $W = 0.1$, $\lambda = [0.1, 1, 2, 3]$, and $k = 0.1$. The curves refer to the sliding velocity $V_0 \simeq 4$, which maximizes μ^*_{tot}.

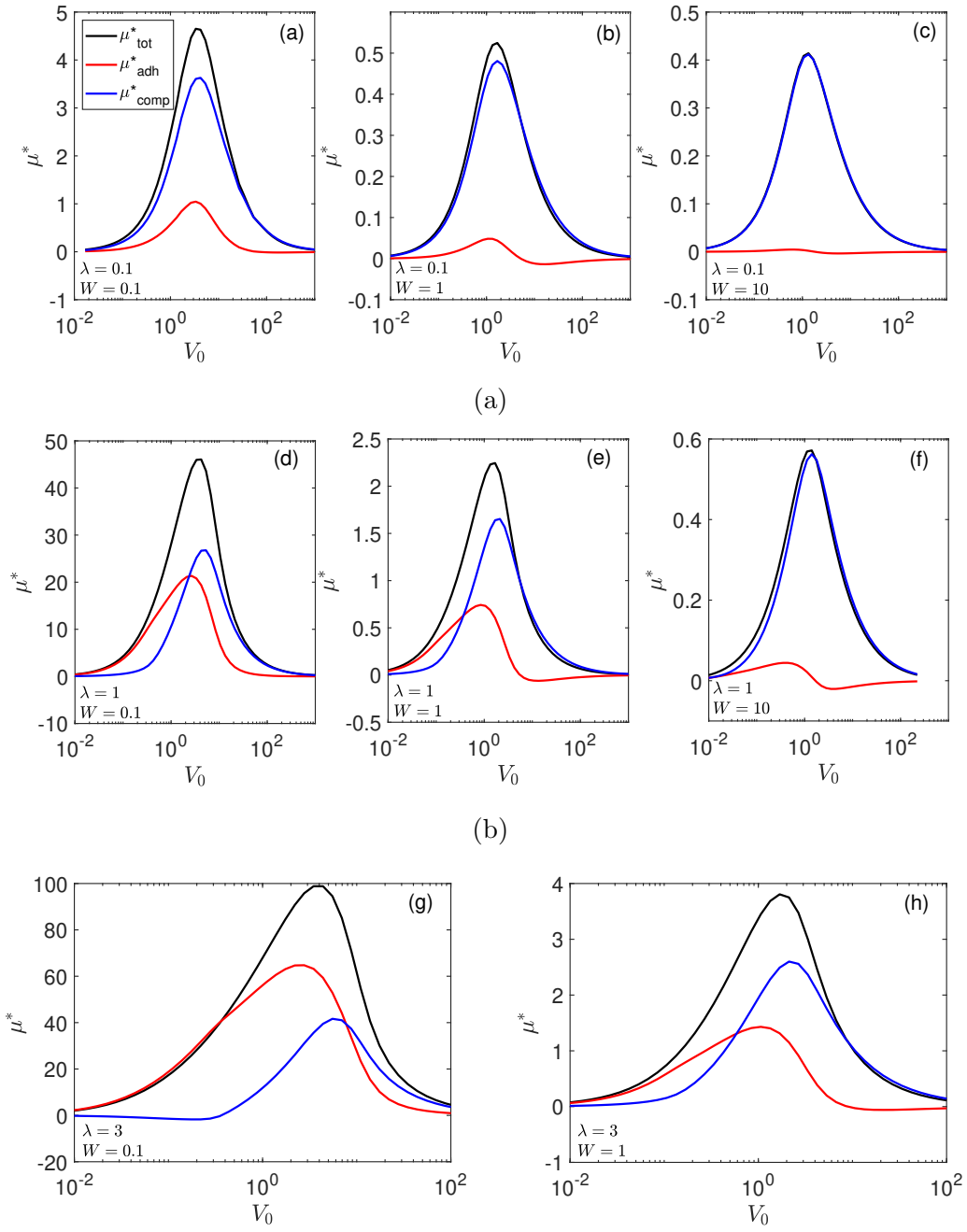

Figure 4.5: The friction coefficient $\mu^* = \mu_R/a_0$ is plotted as a function of the dimensionless speed V_0 for $\lambda = 0.1$ (panels a–c), $\lambda = 1$ (panels d–f), and $\lambda = 3$ (panels g–h), for various dimensionless loads $W = [0.1,\ 1,\ 10]$ and $k = 0.1$. The black lines represent the total friction coefficient obtained from Eq. (16), the red lines indicate the adhesive friction coefficient μ_{adh} computed by including only the tensile tractions in Eq. (4.16), and the blue lines denote the compressive friction coefficient μ_{comp} computed by including only the compressive tractions in Eq. (4.16).

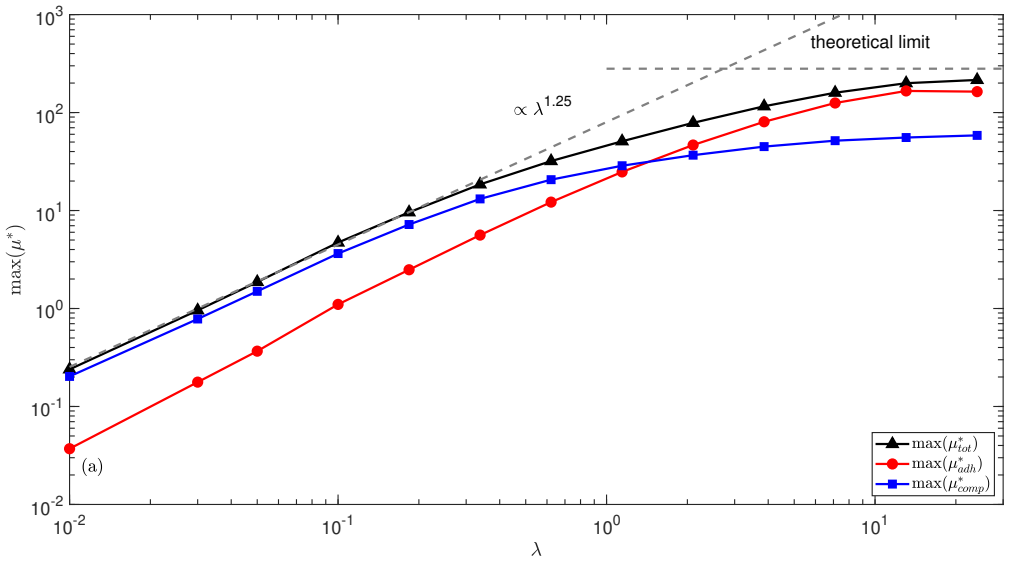

(a)

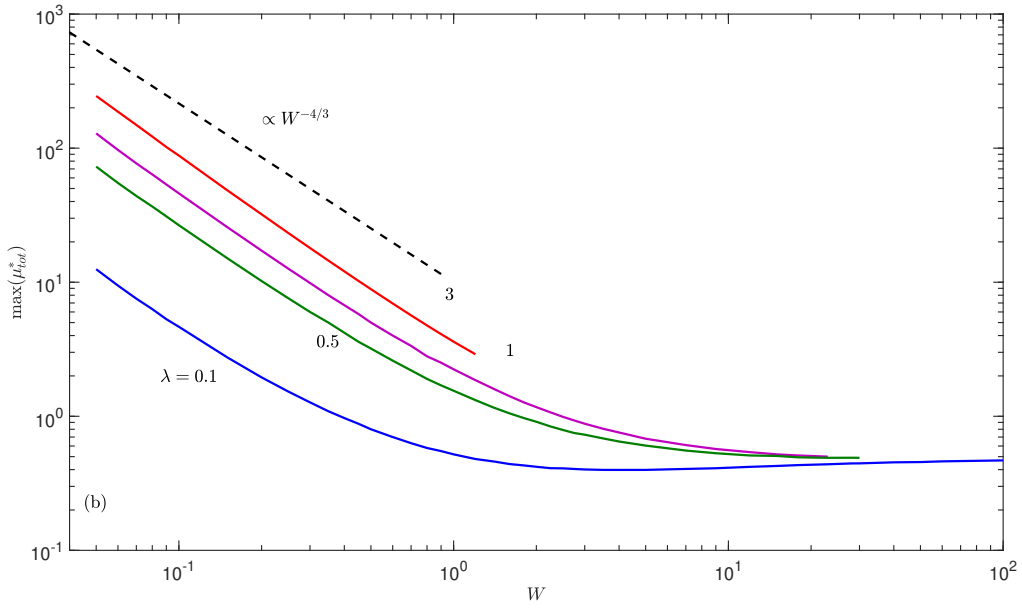

(b)

Figure 4.6: (a) Maximum μ^*_{tot} (black line), μ^*_{adh} (red line), and μ^*_{comp} (blue line) as a function of λ for a fixed value of the normal load $W = 0.1$ and $k = 0.1$. The dashed grey line is a guide to the eye showing $\max(\mu^*) \propto \lambda^{5/4}$. (b) Maximum μ^*_{tot} as a function of W for the Maugis parameters $\lambda = \{0.1, 0.5, 1, 3\}$. The black dashed line is a guide to the eye showing $\max(\mu^*_{\text{tot}}) \propto W^{-4/3}$.

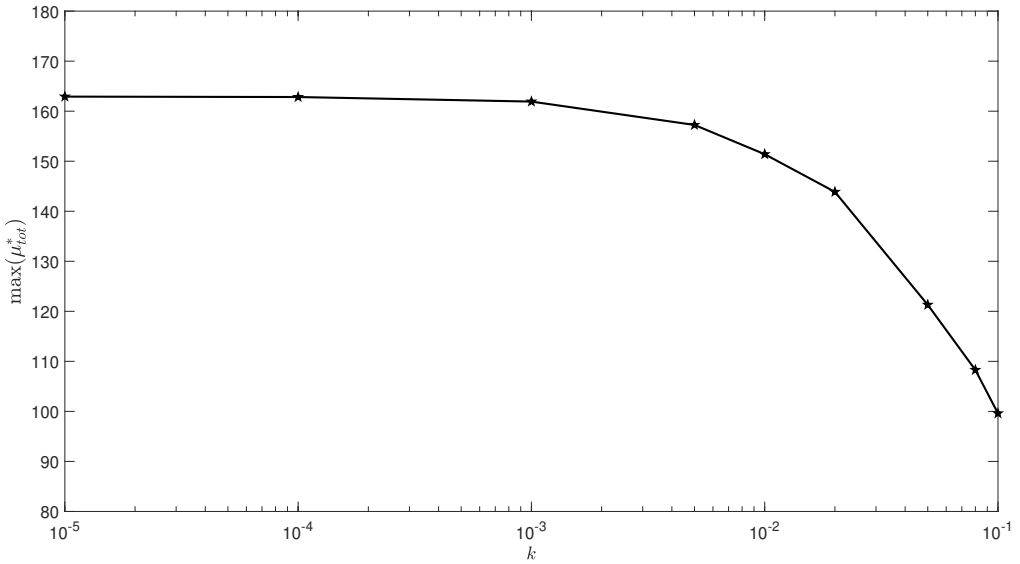

Figure 4.7: Dependence of the maximum dimensionless friction coefficient $\max(\mu^*_{\mathrm{tot}})$ on the material parameter $k = E_0/E_\infty$ for $\lambda = 3$ and $W = 0.1$.

Chapter 5

Rolling Friction with Adhesion in Viscoelastic Media: A Numerical Study Inspired by Barquins' Experiments

Preface

The third part of this thesis is inspired by the classical experiments of Barquins and Roberts on the rolling friction of viscoelastic materials. These pioneering works demonstrated that the resistance to rolling on rubber-like substrates arises from the combined effects of bulk viscoelastic energy dissipation and interfacial adhesive hysteresis. Motivated by these findings, the present study develops a numerical framework to revisit Barquins' observations within a cohesive-zone formulation that explicitly accounts for adhesion through a Lennard–Jones interaction law and viscoelastic response through the Standard Linear Solid model.

The model adopts the Persson–Brener theory as a theoretical benchmark, providing a means to validate and interpret the numerical predictions. Particular attention is given to identifying the interplay between adhesive and viscoelastic contributions to the overall frictional resistance, and to clarifying the velocity-dependent transition between regimes of dominant bulk dissipation and adhesive hysteresis. The study thereby connects experimental insights with modern computational mechanics, offering a unified view of rolling friction in soft viscoelastic systems [209].

Here, a two-dimensional model of a rigid cylinder rolling over a viscoelastic half-space is developed, incorporating adhesive interactions via a Lennard–Jones potential and viscoelastic response through a Standard Linear Solid (SLS) model. The rolling resistance is calculated using a boundary element method, and results are interpreted using the Persson–Brener theory of viscoelastic crack propagation.

5.1 Problem definition

In a series of pioneering experiments, Barquins [210] investigated the rolling behavior of a long rigid cylinder both on top of and beneath inclined viscoelastic rubber substrates. He observed that a velocity-dependent friction force developed during rolling motion, which followed a power-law relationship with the rolling speed. The main findings from his work were that: (i) the friction force exhibited approximately the same magnitude for both positive and negative normal loads, and (ii) the friction force varied with velocity according to a power law similar to that observed in peeling experiments.

These observations suggested that rolling resistance in such systems originates from strong adhesive interactions, giving rise to a peeling-type force at the trailing edge of the contact region. At this edge, the contact behaves as an opening crack, while at the leading edge the crack closes with a much smaller amount of energy release. In his setup, Barquins measured the steady rolling velocity as a function of the inclination angle β of the viscoelastic substrate (see Figure. 5.1). By neglecting bulk dissipation (which becomes dominant only at very high normal loads), the difference between the energy release rates at the trailing and leading edges could be directly related to the measured tangential force as

$$G_{\text{trailing}} - G_{\text{leading}} = f \sin\beta = f_T, \tag{5.1}$$

where m is the cylinder's mass per unit length, $f = mg$ represents the corresponding vertical load per unit length, f_t is its tangential component, and the normal load is given by $w = f\cos\beta$.

From these measurements, Barquins determined that the crack propagation energy scales with velocity as

$$G = kv^n, \tag{5.2}$$

where the exponent $n \simeq 0.55$ was close to the value $n \approx 0.6$ previously obtained in peeling and detachment experiments involving the same transparent polyurethane rubber in contact with glass. The resulting G–v relationship appeared to be largely independent of contact geometry.

Subsequent studies by Charmet and Barquins [211] revealed additional features of this rolling system, namely that: (iii) rolling could occur even under negative loads (i.e., when the cylinder was partially pulled off the substrate), and (iv) the frictional force increased by nearly fifty times between the slowest and fastest velocities tested, with the rolling velocity varying over four orders of magnitude and the friction force over two orders of magnitude, while still maintaining the same power-law dependence. They also observed that the half-width of the contact area followed the scaling law

$$a = k_2 v^{n/3}. \tag{5.3}$$

Unfortunately, Barquins did not report a complete characterization of the viscoelastic modulus of his polyurethane materials, which makes quantitative comparison with theoretical predictions difficult. For this reason, the present study primarily considers a standard linear solid model to represent the viscoelastic behavior, while also discussing the implications of a possible power-law viscoelastic model.

To the best of my knowledge, the experimental observations summarized above (points i–iv) have not been directly compared with theoretical or numerical results in a systematic way. Therefore, in this Chapter,we investigate the adhesive rolling contact between a rigid cylinder and a viscoelastic half-plane using a Boundary Element Method (BEM) formulation coupled with a Lennard–Jones traction–separation law. The analysis demonstrates that the total rolling friction arises from two distinct mechanisms: (i) viscoelastic energy dissipation within the bulk material (which dominates in the absence of adhesion and for which analytical solutions already exist [87]), and (ii) adhesive hysteresis associated with the asymmetry between the opening (trailing) and closing (leading) edges of the contact region.

The different behaviors of opening and closing viscoelastic cracks are well documented in the literature [131], particularly for semi-infinite cracks where the cohesive zone size is much smaller than any other characteristic length in the system. In this work, the Persson–Brener theoretical framework [212] is used to interpret the numerical findings and to provide a deeper understanding of the mechanisms governing rolling friction in viscoelastic adhesive contacts.

5.2 Numerical Model

The numerical framework employed in this chapter is identical to that described in detail in Chapter 4. It is based on a boundary element formulation that couples the viscoelastic response of the substrate, modeled through a Standard Linear Solid (SLS) law, with adhesive interactions represented by the Lennard–Jones traction–separation relation. The governing parameters and equations, discretization strategy, and iterative solution procedure using the Newton–Raphson method follow exactly the same implementation discussed in Sections 4.2–4.4.

For completeness, a brief summary of the main features of the numerical approach is provided below:

- The contact interface is discretized into N uniformly spaced nodes, and the influence matrix is constructed using the fundamental solution for a viscoelastic half–space.
- Adhesive tractions are computed through the Lennard–Jones potential, which introduces nonlinearity in the contact problem.

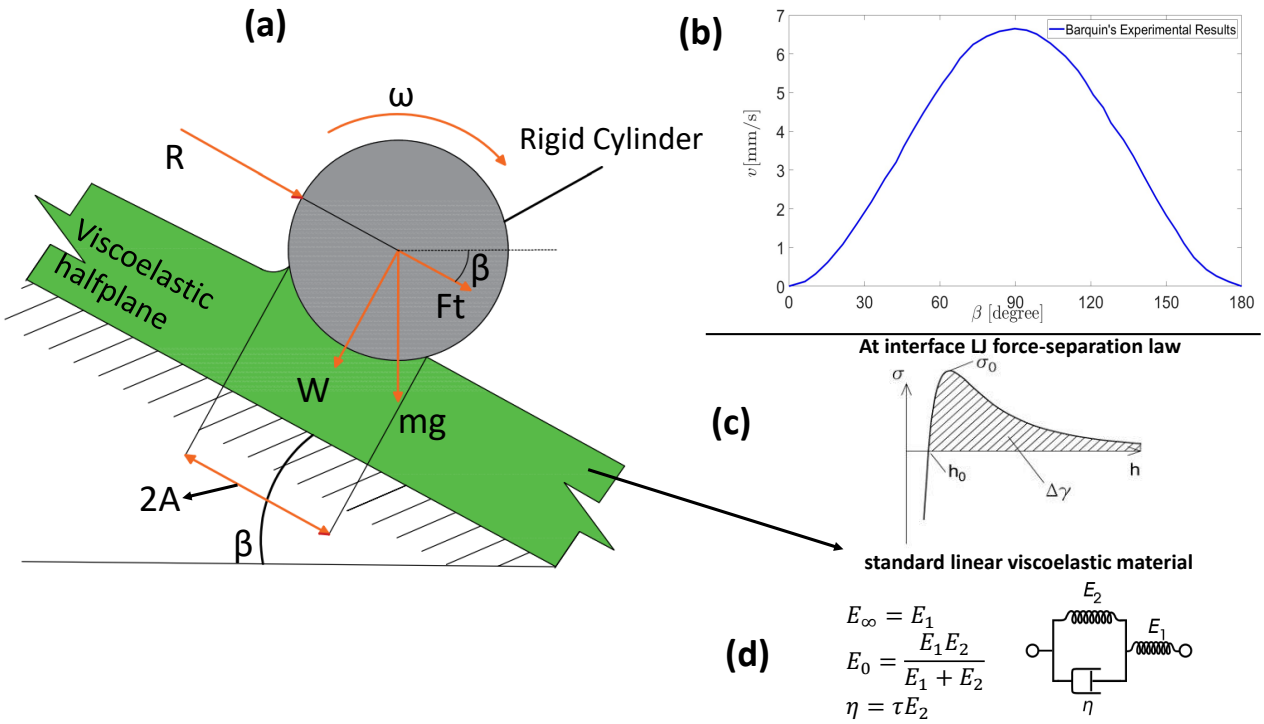

Figure 5.1: Barquins' experiments: (a) the rigid cylinder rolling above or below an inclined viscoelastic rubber substrate; (b) schematic representation of the experimental rolling velocities as a function of the inclination angle; (c) the Lennard–Jones adhesion force–separation law adopted in the present numerical study; and (d) the standard linear solid model representing the viscoelastic behavior of the material.

- The equilibrium equations are solved iteratively using a Newton–Raphson scheme implemented in MATLAB.

Further details of the formulation, validation, and convergence analysis can be found in Chapter 4. Only the results and specific observations related to the rolling contact problem are presented and discussed in the following sections.

5.2.1 Computation of the Friction Force

The total tangential (friction) force is computed by integrating the product of the interfacial pressure and the surface displacement gradient along the entire contact domain. Assuming that rolling occurs from left to right and that the trailing edge lies on the left side, the tangential force is expressed as

$$f_T = -\int p(x)\,\frac{du}{dx}\,dx. \tag{5.4}$$

In dimensionless form, this can be written as

$$F_T = \frac{f_T}{(E_R^* R \Delta\gamma^2)^{1/3}} = -\sqrt{\frac{3a\,\varepsilon}{R}} \int P(X)\,\frac{dU}{dX}\,dX. \tag{5.5}$$

Similarly, for the adhesive case, the dimensionless tangential force can be expressed as

$$F_T^* \frac{R}{a_0} = -\frac{\sqrt{\pi}}{2}\frac{\lambda}{W^{1/2}} \int P(X)\,\frac{dU}{dX}\,dX, \tag{5.6}$$

which depends only on four key dimensionless parameters of the problem: the characteristic velocity, the Maugis parameter λ, the dimensionless load W, and the ratio between the relaxed and instantaneous elastic moduli, $k = E_0/E_\infty$.

$$F_T^* = F_T^*(V_0, \lambda, W, k). \tag{5.7}$$

The dimensionless velocity is defined as

$$V_0 = \frac{v\tau}{a_0} = \frac{1}{2}\sqrt{\frac{\pi}{W}}\frac{v\tau}{\beta}, \tag{5.8}$$

where a_0 represents the Hertzian (adhesiveless) half-width of the contact area. At low velocities, especially in the range where the semi-infinite crack theory of Persson and Brener applies, the dependence of the friction force simplifies further, confirming the validity of the proposed dimensionless formulation.

5.3 Results and Disscution

5.3.1 Pressure Distribution and Energy Dissipation Mechanisms

Figure 5.2 shows the influence of the Maugis–Tabor parameter λ on the pressure distribution within the contact region (Figures. 5.2 a-b) and on the quantity $-P(X)\,\dfrac{dU}{dX}$, which must be integrated in Eq. 5.6 to obtain the dimensionless friction force F_T^* (Figures. 5.2 c-d). Several important trends emerge from these results.

The pressure distribution exhibits significantly sharper tensile peaks in the case of large λ (short-range adhesion) (Figure. 5.2-a) compared to the low-λ case (long-range adhesion) (Figure. 5.2-b). This behaviour reflects the stronger adhesive interactions and localized stress concentrations typical of short-range adhesion. Furthermore, for large λ, the pressure distribution is almost independent of the sign of the normal load, while for small λ, the load sign has a more pronounced effect on the pressure profile. A distinct compressive peak near the leading edge is also observed, which is characteristic of viscoelastic rolling contacts [4, 212].

At high rolling velocities, the pressure distribution becomes nearly symmetric. This behaviour arises because the viscoelastic substrate behaves more elastically at high frequencies (approaching the instantaneous modulus E_∞), leading to similar energy release rates at the leading and trailing edges of the contact. As a result, the overall friction force becomes very small in this regime.

The spatial distribution of the energy dissipation term $-P(X)\,\dfrac{dU}{dX}$ provides further insight into the origins of friction. As shown in Figure. 5.2-c, at intermediate velocities ($V_0 = 1$) the largest contributions to the friction force arise from the trailing edge of the contact, where adhesion-related energy dissipation is dominant. In contrast, the leading-edge contribution is smaller and includes both positive and negative components. At high velocities ($V_0 = 100$), the integrand becomes highly oscillatory with small amplitude, confirming that the net friction force decreases substantially in this regime.

In the case of small λ (Figures. 5.2 b-d, the situation is markedly different. Here, adhesion plays a minor role, and the main contribution to friction arises from bulk viscoelastic dissipation in the central part of the contact region rather than from the edges. Additionally, the friction force becomes significantly more sensitive to the sign of the applied normal load in this regime.

5.3.2 Friction Force Results and Comparison with the Persson–Brener Theory

Figure 5.3 presents the dimensionless friction force F_T^* as a function of the dimensionless rolling velocity $V_0 = \dfrac{v\tau}{a_0}$ for a standard viscoelastic material with $k = E_0/E_\infty = 0.001$. Results are shown for four values of the Maugis–Tabor parameter ($\lambda = 0.1, 1, 2, 3$), covering the transition from the long-range to the short-range adhesion regimes.

The numerical results display a characteristic non-monotonic dependence of F_T^* on V_0. At low velocities, the friction force increases with velocity, reaching a maximum near $V_0 \approx 1$, and then decreases as the velocity continues to rise. This bell-shaped behaviour is consistent with experimental observations [213] and previous theoretical predictions [4, 212].

Two distinct power-law regimes can be identified from the simulations:

- **Low-velocity regime:**

$$F_T^* \propto V_0$$

  where the friction force increases linearly with velocity. This is in excellent agreement with the classical adhesiveless theory of Persson [3], which attributes friction at low speeds to bulk viscoelastic losses.

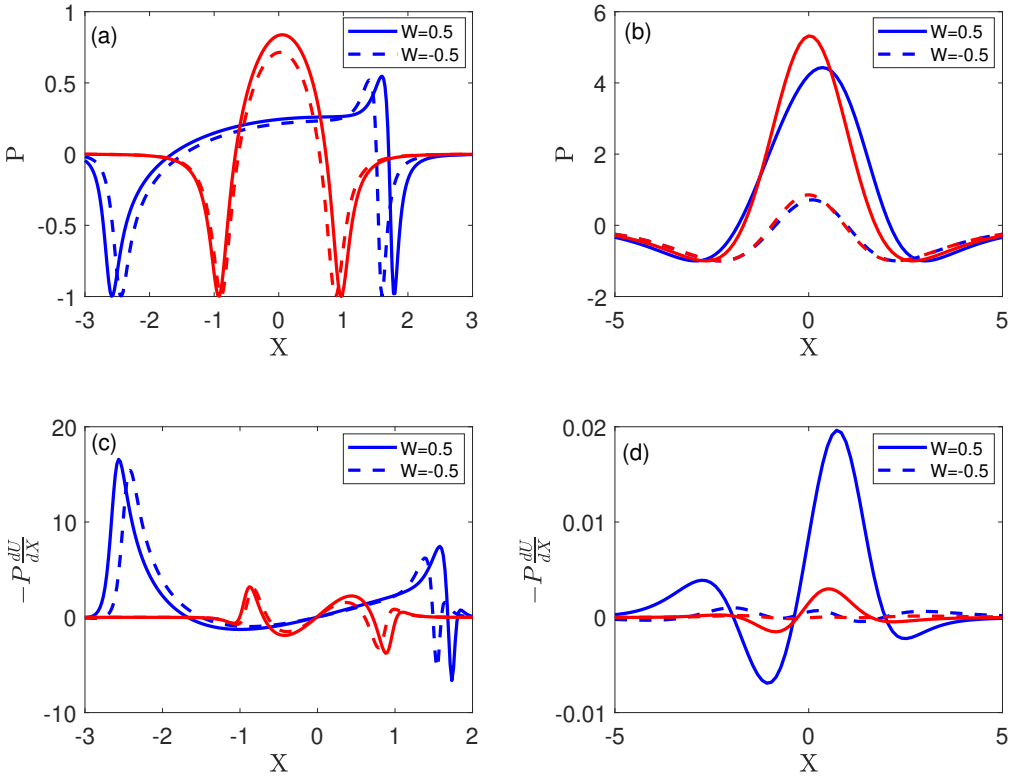

Figure 5.2: The pressure distribution (**a**, **b**) and the quantity $-P(X)\,\dfrac{dU}{dX}$, which must be integrated in Eq. (5.6) to obtain the dimensionless friction force F_T^*. The trailing edge is on the right side. The material parameters are $k = E_0/E_\infty = 0.001$ and the Maugis–Tabor parameter is $\lambda = 3$ in (**a**, **c**) and $\lambda = 0.1$ in (**b**, **d**). Dashed lines indicate negative normal loads, while solid lines represent positive normal loads. The blue line corresponds to $V_0 = 1$ and the red line to $V_0 = 100$.

- **Intermediate-velocity regime:**

$$F_T^* \propto V_0^{0.5}$$

  where the dependence of friction on velocity becomes sub-linear. This scaling reflects the increasing importance of adhesive hysteresis and crack dynamics in this regime.

The results in Figure 5.3 are shown for a fixed normal load $|W| = 0.1$. The solid and dashed black curves correspond to positive ($W > 0$) and negative ($W < 0$) loads, respectively. These results confirm the experimental observation of Barquins [213] that the friction force remains approximately the same whether the cylinder rolls above or beneath the inclined viscoelastic plane (for the same inclination angle θ), provided that the Maugis–Tabor parameter is sufficiently large ($\lambda \gtrsim 2$). For lower values of λ, which

are unlikely to correspond to the conditions in Barquins' experiments, the friction shows a more noticeable dependence on the sign of the normal load.

Moreover, the simulations demonstrate that the magnitude of the dimensionless friction force increases with the Maugis–Tabor parameter, reflecting the growing contribution of adhesive hysteresis as adhesion becomes more short-ranged. These findings motivate the development of a more general theoretical description, which we explore in the next section by extending the Persson–Brener model.

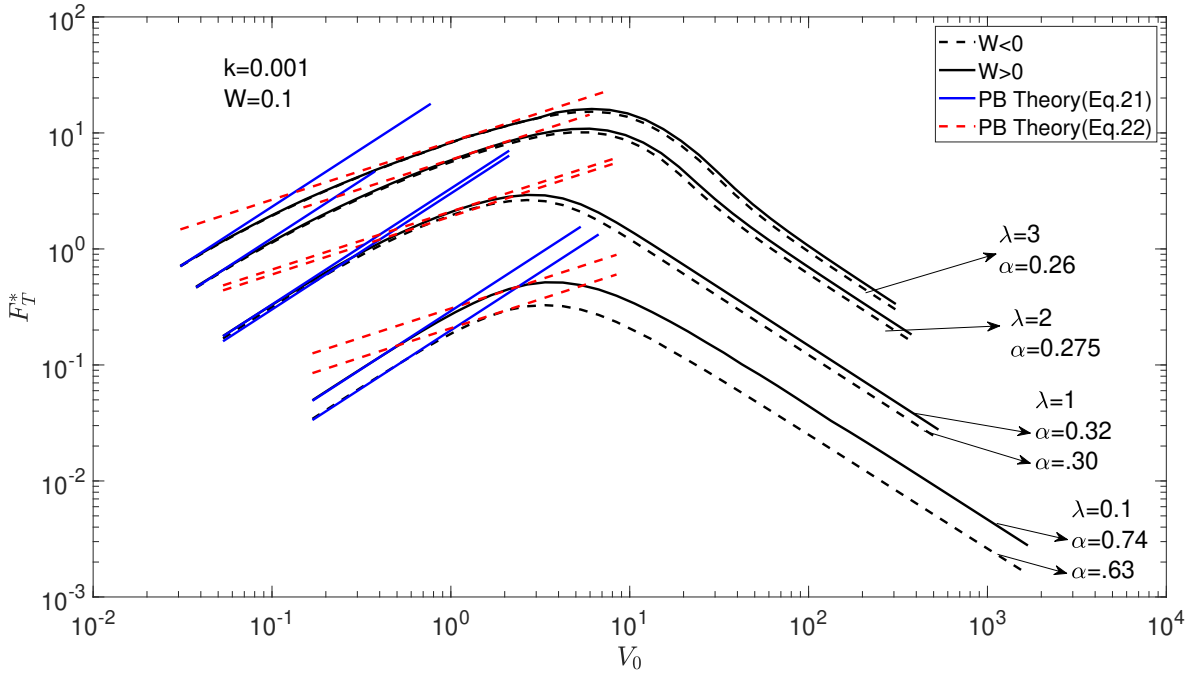

Figure 5.3: Dimensionless friction force F_T^* as a function of dimensionless velocity V_0 for a viscoelastic material with $k = 0.001$ and four values of the Maugis–Tabor parameter ($\lambda = 0.1, 1, 2, 3$). Two distinct power-law regimes can be observed: $F_T^* \propto V_0$ at low velocities (blue solid line) and $F_T^* \propto V_0^{0.5}$ at intermediate velocities (red dashed line). Results are shown for a normal load $|W| = 0.1$; solid and dashed black curves correspond to positive and negative loads, respectively.

5.3.3 Estimate from the Persson–Brener Model

Classical fracture mechanics theories can be applied to estimate the energy release rates at the leading and trailing edges of the contact, denoted by G_{leading} and G_{trailing}, respectively. As long as the cohesive zone remains relatively small (which is valid up to velocities near the maximum in the friction curve), it has been shown [212] that, to a very good approximation,

$$G_{\text{leading}}(v) \approx \frac{1}{G_{\text{trailing}}(v)}. \tag{5.9}$$

The Persson–Brener (PB) theory provides a way to compute $G_{\text{trailing}}(v)$ by relating it to the size of the so-called cut-off region $c(v)$, within which the stresses are approximately constant and equal to a cut-off stress σ_c. It should be noted that this cut-off stress does not correspond directly to the cohesive strength in the Lennard–Jones model used in our numerical simulations. Cohesive-zone models typically depend on the specific shape of the cohesive law, which primarily introduces a shift in the velocity scale [204, 214]. Thus, a full numerical investigation is necessary to relate our results to the PB framework.

According to the PB model, the trailing-edge energy release rate can be expressed as

$$\frac{G_{\text{trailing}}(v)}{\Delta\gamma} = \frac{c(v)}{c_0}, \tag{5.10}$$

where $\Delta\gamma$ is the work of adhesion and c_0 is the size of the fracture process zone at zero velocity, defined as

$$c_0 = \frac{E_0 \Delta\gamma}{2\pi\sigma_c^2}. \tag{5.11}$$

The size of the cut-off region satisfies the following implicit equation [212]:

$$\frac{c(v)}{c_0} = \left[1 - \left(1 - \frac{E_0}{E_\infty}\right)\left(\sqrt{1 + \left(\frac{c_0 v}{c(v) v_0}\right)^{-2}} - \left(\frac{c_0 v}{c(v) v_0}\right)^{-1}\right)\right]^{-1}. \tag{5.12}$$

The difference between the trailing and leading energy release rates gives the total friction force per unit width (Figure 5.4). This can be approximated as

$$\frac{f_T(v)}{\Delta\gamma} \simeq \frac{G_{\text{trailing}}(v) - 1/G_{\text{trailing}}(v)}{\Delta\gamma}. \tag{5.13}$$

From the PB model, the above expression leads to the following approximate scaling relations for the friction force:

$$\frac{f_T(v)}{\Delta\gamma} \approx \begin{cases} \dfrac{v}{v_0}, & v < v_0 \\ \left(\dfrac{v}{v_0}\right)^{1/2}, & v > v_0 \end{cases} \tag{5.14}$$

where the characteristic velocity v_0 is defined as

$$v_0 = \frac{c_0}{2\pi\tau}. \tag{5.15}$$

Equation (5.11) indicates that the fracture process zone c_0 is typically extremely small (often less than a nanometre), which raises questions about the physical validity of the PB theory at very small scales [215]. Nevertheless, the PB framework provides useful scaling laws that capture the main features of the friction behaviour observed in both

experiments and numerical simulations.

It is convenient to define a new dimensionless friction force in terms of the fracture energy:

$$F_{T,\mathrm{PB}} = \frac{f_T(v)}{\Delta\gamma} = F_{T,\mathrm{PB}}(V_{\mathrm{PB}}) \tag{5.16}$$

which depends only on the dimensionless velocity as:

$$V_{\mathrm{PB}} = \frac{v}{v_0} \tag{5.17}$$

Therefore, we have interest to investigate where it is possible to simply adopt PB's theory in view of the simplicity of the results.

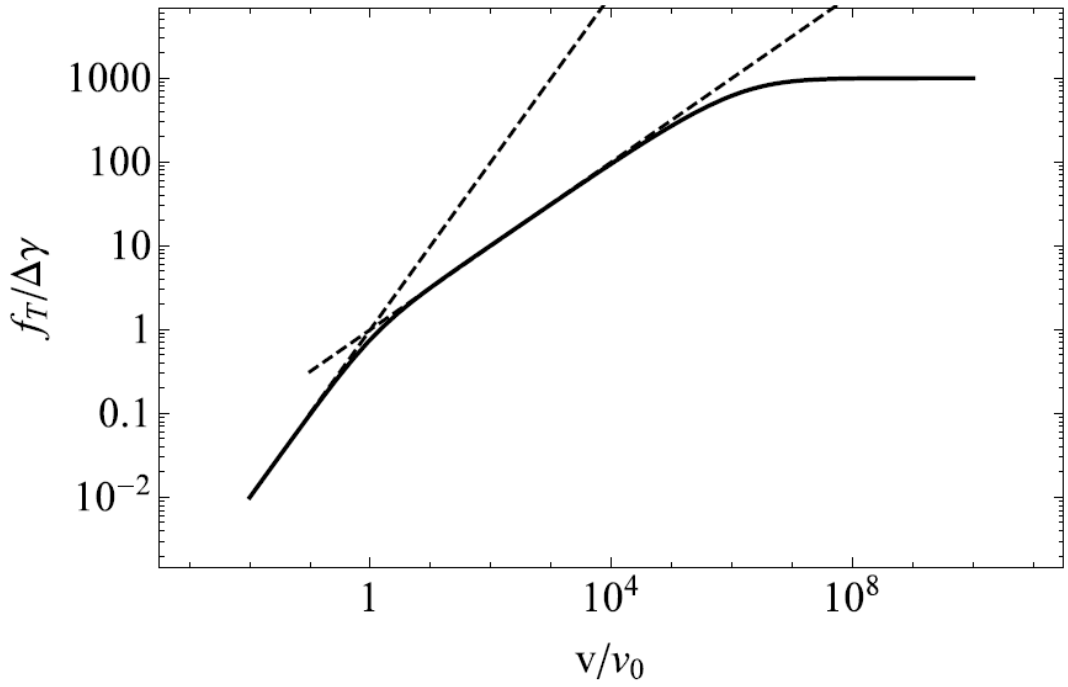

Figure 5.4: Predicted dimensionless friction force from Persson–Brener theory (Eq. 5.14), showing linear scaling at low velocities and a square-root dependence at intermediate velocities. These results closely resemble the numerical results shown in Figure. 5.3.

To this scope, we need to investigate the relationship between σ_c and the cohesive stress of our cohesive model σ_0, so let us write it in terms of an unknown prefactor

$$\sigma_c = \alpha\sigma_0. \tag{5.18}$$

The results presented in Figure 5.4 closely resemble the numerical outcomes shown in Figure 5.3 . Using the dimensionless notation and Eq. 5.8, the Persson–Brener (PB)

prediction in the low-velocity regime can be expressed as

$$a_0 = \left(\frac{4wR}{\pi E_0^*}\right)^{1/2} = \frac{2\beta\sqrt{W}}{\pi}, \tag{5.19}$$

and accordingly,

$$F_{T1}^* = (2\pi)^2\alpha^2\lambda^2 V_0. \tag{5.20}$$

where $V_0 \propto \sqrt{\frac{1}{W}}$ (see Eq. 5.8). This indicates that while the dimensionless tangential force depends on the applied normal load, the dimensional force predicted by the PB theory does not.

In the intermediate velocity range, the model gives the following.

$$F_{T2}^* = \pi\sqrt{2\pi}\frac{\alpha\lambda}{W^{1/4}}(\frac{1}{\pi})^{1/4}V_0^{1/2}. \tag{5.21}$$

The predictions of Eqs. 5.20 and 5.21 are illustrated in Figure 5.3 , showing that for $k = E_0/E_\infty = 0.001$ and $\lambda = 0.1$, 1, 3, the PB equations accurately describe the behavior in both the low- and intermediate-velocity regimes. However, to fit the numerical data, different α values—varying approximately by a factor of three—are required. The linear regime is more extended for small λ and becomes narrower for larger λ. Since large λ values correspond more closely to experimental conditions, this may explain why the linear regime is rarely observed in experiments. Moreover, very high velocities are typically difficult to achieve experimentally, so only the intermediate power-law regime is usually captured.

Figure 5.5 further confirms that the prefactor α is nearly independent of the normal load for large Maugis–Tabor parameters, considering the realistic case $k = E_0/E_\infty = 0.001$. Similarly, Figure 5.6 shows that α decreases slightly with increasing normal load but remains approximately constant for $\lambda > 2$. Finally, Figure 5.7 indicates that α is almost insensitive to the modulus ratio $k = E_0/E_\infty$ for $k < 0.1$, which represents a realistic range for many viscoelastic materials, typically $k < 10^{-3}$.

Overall, these results demonstrate that the Persson–Brener estimate provides an excellent fit to the numerical data over a broad range of realistic conditions—namely, for low to intermediate normal loads, practical viscoelastic moduli, and relatively large Maugis–Tabor parameters.

5.4 Discussion: More Complex Material Models

Our numerical model shows qualitative agreement with several key experimental observations reported in the literature [4, 212, 213], particularly regarding the velocity dependence of the fracture energy. Specifically, the simulations predict that the fracture energy increases approximately as $V_0^{0.5}$, which is close to the $V_0^{0.55}$ dependence measured

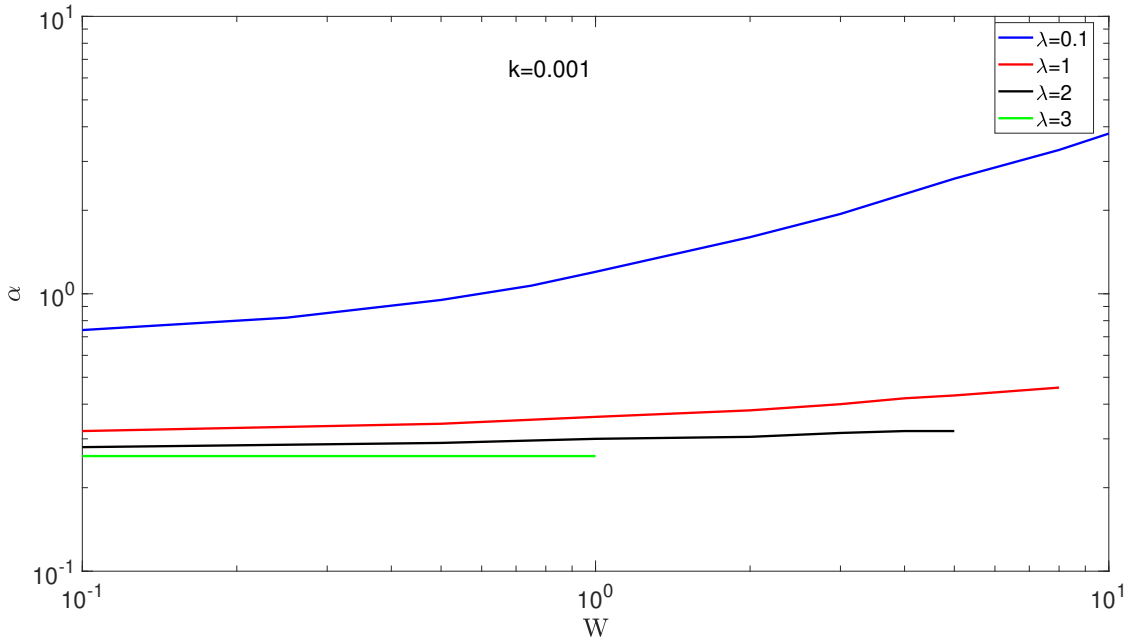

Figure 5.5: Dependence of the prefactor α on normal load for different Maugis–Tabor parameters. For large λ, α is nearly independent of load.

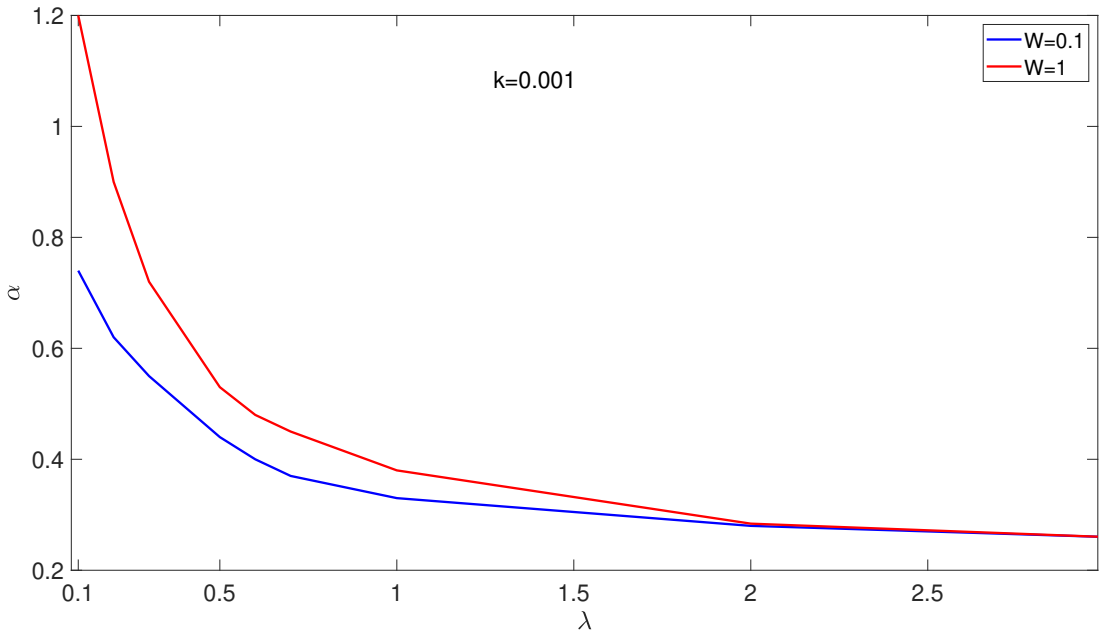

Figure 5.6: Variation of α with the Maugis–Tabor parameter. The prefactor decays with increasing λ but remains approximately constant for $\lambda > 2$.

experimentally in rolling friction tests [213]. However, this agreement may be partially coincidental, as it is unlikely that the rubber used by Barquins in those experiments could be accurately described as a single-relaxation-time viscoelastic material.

Further discrepancies emerge when comparing contact area predictions. Figure 5.8

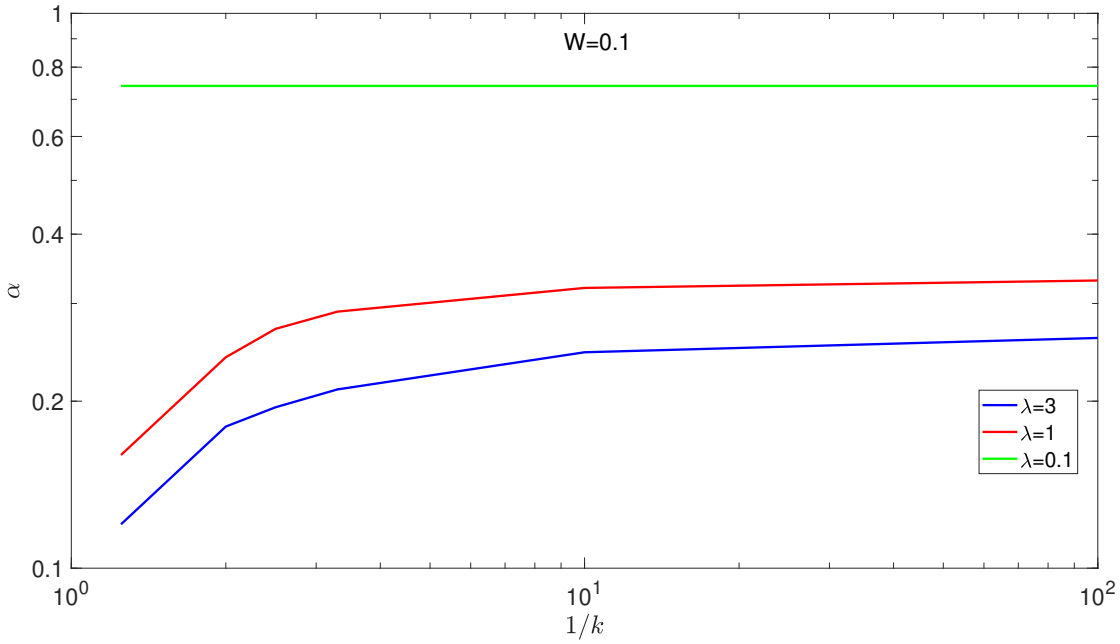

Figure 5.7: Dependence of α on the viscoelastic modulus ratio k. For $k < 0.1$, the prefactor is essentially independent of k, consistent with typical material behaviour.

shows the dimensionless contact area $2A$ as a function of dimensionless velocity V_0 for $k = 0.001$, with the normal load set to the pull-off value. Barquins reported a power-law scaling of the form

$$A \sim V_0^{0.55/3} \tag{5.22}$$

for the contact area, whereas our simulations predict a significantly weaker dependence:

$$A \sim V_0^{1/30} \tag{5.23}$$

in the velocity range where a power-law regime is observed. Importantly, the choice of setting the normal load equal to the pull-off load should not significantly affect the results for large λ, as the system is in a regime where the contact area is predominantly governed by adhesive forces. These forces are known to increase with decreasing velocity, particularly in the low to intermediate velocity range.

In view of these discrepancies and the limitations of our current model, it would not be overly difficult to extend the analysis to materials characterized by a broader distribution of relaxation times. Such a modification would more accurately represent the viscoelastic behaviour of real rubbers. However, because the full viscoelastic characterization of the transparent polyurethane rubber used in Barquins' experiments is not available, such an extension would have limited predictive power.

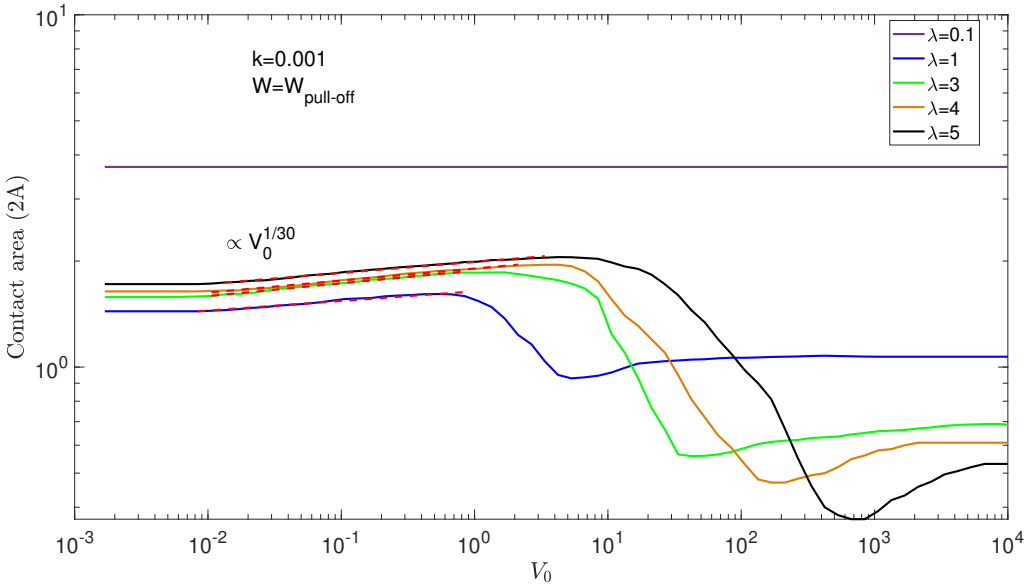

Figure 5.8: Dimensionless contact area $2A$ as a function of the dimensionless velocity V_0 for $k = 0.001$ and normal load set to the pull-off value. The numerical results show a weaker dependence on velocity compared to the experimental scaling reported by Barquins [213].

Nevertheless, the discussion in this section highlights the importance of considering more complex rheological models when attempting to quantitatively reproduce experimental results. In the next section, we explore the potential implications of adopting a power-law viscoelastic model as an alternative approach.

5.4.1 Power Law Materials

To further explore the influence of material behavior on rolling friction, we considered the case of a power-law viscoelastic solid, as originally discussed by Persson and Brener. In such materials, the relaxation spectrum is described by a spectral density function

$$S(\tau) = S_0\, \tau^{-s}, \tag{5.24}$$

defined within the range $\tau_1 < \tau < \tau_2$ and zero elsewhere. This distribution results in a complex viscoelastic modulus $E(\omega)$ that increases with frequency approximately as ω^{1-s}, where $0 < s < 1$. Specifically, the relationship between the modulus and the spectrum is given by

$$\frac{1}{E(\omega)} = \frac{1}{E_\infty} + \int_{\tau_1}^{\tau_2} \frac{S(\tau)}{1 - i\omega\tau}\, d\tau = \frac{1}{E_\infty} + S_0 \int_{\tau_1}^{\tau_2} \frac{\tau^{-s}}{1 - i\omega\tau}\, d\tau, \tag{5.25}$$

which can also be expressed using the incomplete Beta function $B(z, s, 0)$ as

$$\frac{1}{E(\omega)} = \frac{1}{E_\infty} + S_0 (-i)^{1-s} \omega^{-(1-s)} \big[B(-i\omega\tau_2, s, 0) - B(-i\omega\tau_1, s, 0)\big]. \tag{5.26}$$

Within the Persson–Brener framework, this viscoelastic model yields a normalized fracture energy of the form

$$\frac{G(v)}{\Delta\gamma} = \frac{c(v)}{c_0} = \left[1 - E_0 \int_0^\infty S(\tau) \left(\sqrt{1 + b(\tau)^{-2}} - b(\tau)^{-1}\right) d\tau\right]^{-1}, \tag{5.27}$$

where $b(\tau) = 2\pi v\tau/c$ and c is the size of the process zone.

For a broad relaxation spectrum ($\tau_2/\tau_1 \gg 1$) and typical rubbers with $s \simeq 0.6$, the Persson–Brener theory predicts

$$\frac{G(v)}{\Delta\gamma} \sim v^n, \qquad n = \frac{1-s}{2-s}. \tag{5.28}$$

For $s = 0.6$, this gives $n \approx 0.29$. This exponent is notably smaller than that measured in Barquins' experiments, where $n \approx 0.55$–0.6 was reported for rolling and peeling tests. Therefore, reproducing the observed power law would require $s \approx 0$, corresponding to a nearly ideal standard linear solid.

Numerical results for various exponents $s = 0$, 0.25, 0.5, 0.75 (see Figure 5.9) show that while the overall magnitude of the frictional response changes with s, the qualitative trends and velocity scaling remain similar. In other words, the use of a power-law material mainly affects the prefactor of the friction law rather than the exponent itself, leaving the general agreement with experimental trends largely unchanged.

5.5 Conclusion

In this study, we have numerically investigated the rolling friction of a rigid cylinder on a viscoelastic substrate by using a boundary element formulation. The analysis extends previous models by incorporating both adhesive and viscoelastic effects over a broad range of normal loads, relaxation spectra, and Maugis–Tabor parameters.

The numerical results show excellent agreement with the Persson–Brener (PB) analytical predictions in the low- and intermediate-velocity regimes. In particular, the PB equations reproduce the linear and power-law dependencies of the tangential force on velocity observed in our simulations, confirming their physical validity over a wide range of realistic material parameters. For large Maugis–Tabor parameters and small modulus ratios ($k = E_0/E_\infty < 0.1$), the dimensionless force prefactor remains nearly independent of the applied normal load, which supports the general applicability of the PB approach.

The study further demonstrates that while the linear velocity regime is extended for small values of the viscoelastic parameter λ, it becomes narrower as λ increases, which may explain why it is rarely observed in experiments. The high-velocity regime, on the other hand, is difficult to reach experimentally, and thus most measurements correspond to the intermediate power-law range.

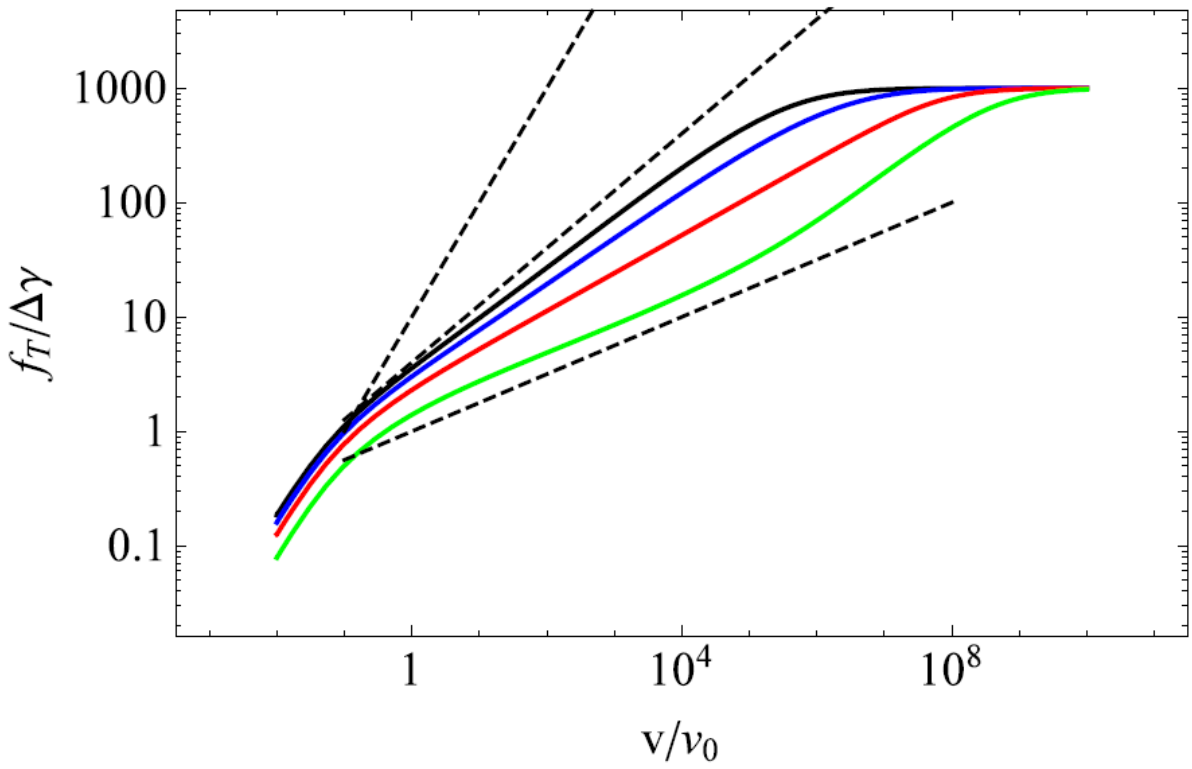

Figure 5.9: The friction force estimated from the Persson–Brener theory for a power-law material having $\tau_1 = 10^{-6}\,\mathrm{s}$ and $\tau_2 = 1\,\mathrm{s}$ (entanglement time), $E_0/E_\infty = 0.001$, and showing $s = 0$, 0.25, 0.5, and 0.75 (solid black, blue, red, and green lines, respectively). The three dashed black lines indicate the relations $f_T/\Delta\gamma = 10\,v/v_0$, $f_T/\Delta\gamma = 4\,(v/v_0)^{1/2}$, and $f_T/\Delta\gamma = (v/v_0)^{1/4}$, respectively.

For materials with a power-law relaxation spectrum, the numerical results confirm that the velocity dependence of the frictional force follows a similar scaling to the PB prediction. Although the exponent of the power-law dependence may vary slightly with the spectral parameter s, the overall qualitative behavior remains the same. This indicates that the Persson–Brener theory provides a robust approximation for a wide range of viscoelastic materials, from standard linear solids to power-law media.

In summary, our results validate the Persson–Brener framework as an effective predictive tool for rolling and sliding friction of viscoelastic materials under adhesive conditions. The approach successfully bridges the gap between analytical theory and numerical simulation and can be further extended to more complex geometries, surface roughness effects, and three-dimensional contact configurations.

Chapter 6

Conclusion

This thesis presented an integrated study of adhesion, friction, and viscoelasticity in soft contact mechanics, addressing three interrelated problems: (i) the suppression of buckling in thin spherical shells through interfacial adhesion and friction, (ii) the sliding friction of a viscoelastic cylinder in adhesive contact with a rigid surface, and (iii) the rolling friction of a rigid cylinder over viscoelastic substrates with adhesive interactions. Although distinct in geometry and configuration, these systems collectively reveal how surface forces, dissipative processes, and material viscoelasticity govern the mechanical stability and energy dissipation of soft interfaces.

6.1 Adhesion and Friction Effects on Buckling Suppression in Thin Shells

The first part of this study investigated how adhesion and friction act synergistically to suppress snap-through instability in thin spherical shells under compression. Using finite element simulations validated by controlled experiments on PDMS hemispherical shells, it was demonstrated that increasing adhesion energy and interfacial friction can substantially delay or even eliminate buckling. A critical adhesion strength, γ_c, was derived analytically for frictionless conditions, showing excellent agreement with numerical predictions. The results established a clear boundary between buckling and non-buckling regimes as a function of normalized thickness (h/R), adhesion (γ), and friction coefficient (μ).

The combined influence of adhesion and friction modifies the energy balance between bending and stretching, stabilizing the shell even under large deformations. These findings have broad implications for soft capsules, flexible electronics, and bio-inspired structures, where instability control is crucial. The study demonstrated, for the first time, that experimentally achievable adhesion and friction values can completely suppress buckling, validating the theoretical prediction and offering practical guidelines for designing robust

thin-shell systems.

6.2 Sliding Contact Between a Rigid Cylinder and a Viscoelastic Half-Space with Adhesion

The second study focused on the sliding interaction between a rigid cylinder and a viscoelastic half-space, incorporating adhesion through a Lennard–Jones potential. A boundary element formulation was used to compute pressure distribution, surface deformation, and frictional response under varying sliding velocity, load, and Maugis–Tabor parameter λ.

The results revealed a non-monotonic, bell-shaped dependence of the friction coefficient on sliding velocity, consistent with classical experimental observations by Grosch and Barquins. At low velocities, adhesive contributions dominate, while at higher velocities viscoelastic dissipation becomes significant. The Maugis–Tabor parameter was identified as a key dimensionless quantity governing the transition between short- and long-range adhesion regimes. Increasing λ enhances interfacial asymmetry and shifts frictional resistance toward the trailing edge of the contact zone, resembling viscoelastic crack propagation phenomena.

This work provided a quantitative framework linking adhesive length scales to frictional asymmetry, thereby bridging the gap between molecular adhesion and continuum viscoelastic mechanics. It advances predictive modeling of soft friction, particularly in applications such as elastomeric seals, tire–road interactions, and tactile sensors.

6.3 Rolling Friction with Adhesion in Viscoelastic Media

The third study was inspired by Barquins' classical experiments on the rolling of rigid cylinders over viscoelastic substrates, which revealed that rolling resistance in soft materials originates from both bulk viscoelastic losses and interfacial adhesive hysteresis. In this work, these mechanisms were examined using a numerical boundary element framework that couples a cohesive-zone adhesion law with the Standard Linear Solid viscoelastic model. The analysis reproduced the characteristic non-monotonic dependence of rolling friction on velocity reported experimentally, demonstrating low-velocity linear scaling and intermediate-velocity square-root scaling consistent with the Persson–Brener theoretical predictions.

The simulations confirmed that at low rolling velocities, adhesion dominates and the hysteretic losses at the contact edges control the resistance, whereas at higher velocities,

bulk viscoelastic dissipation becomes the main source of energy loss. The excellent agreement between the numerical results and the Persson–Brener analytical model validates the implemented approach and emphasizes the predictive capability of the framework.

This connection between Barquins' experimental findings and modern numerical modeling not only strengthens the theoretical understanding of soft contact friction but also establishes a validated methodology for analyzing adhesion-controlled energy dissipation in deformable interfaces.

Chapter 7

Future Work

7.1 Sliding Response of the Hemispherical Shell

To enable the use of the hemispherical shell as a soft robotic gripper, the structure must be capable of sustaining not only normal indentation loads but also tangential sliding. Initially, under mode I deformation, the contact region forms a disc-shaped area and can be expected to behave similarly to a solid sphere subjected to normal loading. According to previous studies [216, 217], such contact evolves from a circular to an elliptical shape during sliding, accompanied by a reduction in the overall contact area.

In the case of the hemispherical shell indented into the post-buckling regime, the response to superimposed sliding remains largely unexplored. To investigate this, the existing experimental setup was modified to include lateral motion of the PLA disc once indentation to the buckled configuration had been achieved. Sliding was manually applied in a smooth and controlled manner while continuously recording the reaction force in the normal direction. Because the PLA disc obstructed the bottom view, only the front perspective—consistent with prior observations—was captured during these tests. The direction of sliding is illustrated in Figure 7.1-a.

The measured data from the sliding experiments are presented in Figure 7.1-b and include results from three separate experimental runs. When the hemispherical shell was held at a constant indentation in the buckled state, a gradual decrease in the recorded normal force was observed over time, indicating a relaxation effect within the system. This behaviour, represented by the red curve in Figure 7.1-b, was not previously detected in experiments where indentation was continuously cycled without a relaxation period. During relaxation, neither visible changes in the shell's profile nor displacement of the apex were observed.

Subsequent sliding tests, represented by the green and blue curves, showed no such relaxation once sliding commenced, confirming that the observed changes were not due to sensor drift. In these tests, sliding was applied after allowing the shell to remain

at rest in its buckled configuration for a period of time. Upon initiation of sliding—at approximately 141 s for the green curve—a pronounced drop in the normal reaction force occurred, accompanied by a visible alteration in the deformation profile. Two representative frames from the recorded video are shown in Figure 7.2.

The experimental observations reveal that the onset of sliding causes the trailing edge (right-hand side) of the hemispherical shell to lift from the substrate, leading to a partial loss of contact area. This lifting effect is clearly visible in Figure 7.2-b. As a result, the deformation becomes non-axisymmetric, and the shell exhibits a local thinning of the contact zone toward the trailing edge. Although this thinning is not evident in the captured images, it was clearly observed during the experiments. Despite this reduction in contact area, the overall loss remains moderate, suggesting that the hemispherical shell retains sufficient contact to maintain functionality as a soft gripper. Nonetheless, further experimental and numerical studies are recommended to better understand the mechanisms driving this behaviour and to develop strategies for minimizing contact loss during combined normal and tangential loading.

7.2 Multilayer and Multi-material Hemispherical Shells

In multilayer and multi-material hemispherical shells, the interaction between individual layers leads to the development of internal stresses. These stresses are stored as residual stresses, which can be released when the shell is mechanically perturbed. This behaviour is of particular interest because it provides an opportunity to modify the structural response of the shell through controlled preloading or deformation cycles prior to operation.

By exploiting this mechanism, it may be possible to employ hemispherical shells with specific thicknesses and interfacial friction properties that would otherwise buckle prematurely under normal operating conditions. The release of residual stresses through a series of preloading cycles—referred to as preruns—could effectively delay the onset of buckling, thereby enhancing the shell's stability and load-bearing capacity.

Understanding how this mechanical tuning depends on the number of layers, material combinations, and the number of preruns would be a valuable extension of the present study. This concept could be particularly beneficial in the context of soft robotic grippers or adaptive contact systems, where precise control over buckling behaviour and stiffness is essential for reliable performance. Developing a predictive framework to relate these parameters to the onset of instability could thus open new avenues for the design of multilayered compliant structures with tailored mechanical responses.

7.3 Advanced Numerical Modelling of Viscoelastic Contact

Over the past six decades, extensive numerical research has provided fundamental insights into the contact mechanics of viscoelastic materials. These developments have significantly advanced the understanding of the mechanical and tribological behaviour of time-dependent materials under a wide range of operating conditions. Such progress enables the scientific community to exploit viscoelastic materials more effectively in engineering applications through predictive and physically consistent models.

By combining efficient computational techniques with comprehensive theoretical formulations that describe the viscoelastic contact response under dry, lubricated, or non-isothermal environments, numerous numerical frameworks have been developed to simulate complex contact phenomena. These models contribute to multiple disciplines, as viscoelastic contact problems are pervasive across mechanical, biomedical, and industrial systems.

Despite the substantial progress, several aspects remain insufficiently explored. In particular, the influence of surface roughness has been investigated primarily for dry contact involving linear viscoelastic materials, whereas its role in lubricated, thermoviscoelastic, and nonlinear viscoelastic contacts has received limited attention. The interaction between surface topography, lubrication, temperature variation, and viscoelastic time-dependence is expected to have a pronounced effect on the overall contact response.

Future numerical studies should therefore aim to incorporate the synergistic effects of surface roughness, thermal gradients, and nonlinear viscoelastic constitutive behaviour into fully coupled contact models. Such efforts would provide a more realistic and predictive description of interfacial phenomena and frictional energy dissipation in practical applications. Developing computationally efficient yet accurate frameworks to address these coupled effects remains an open and highly relevant research direction for the future.

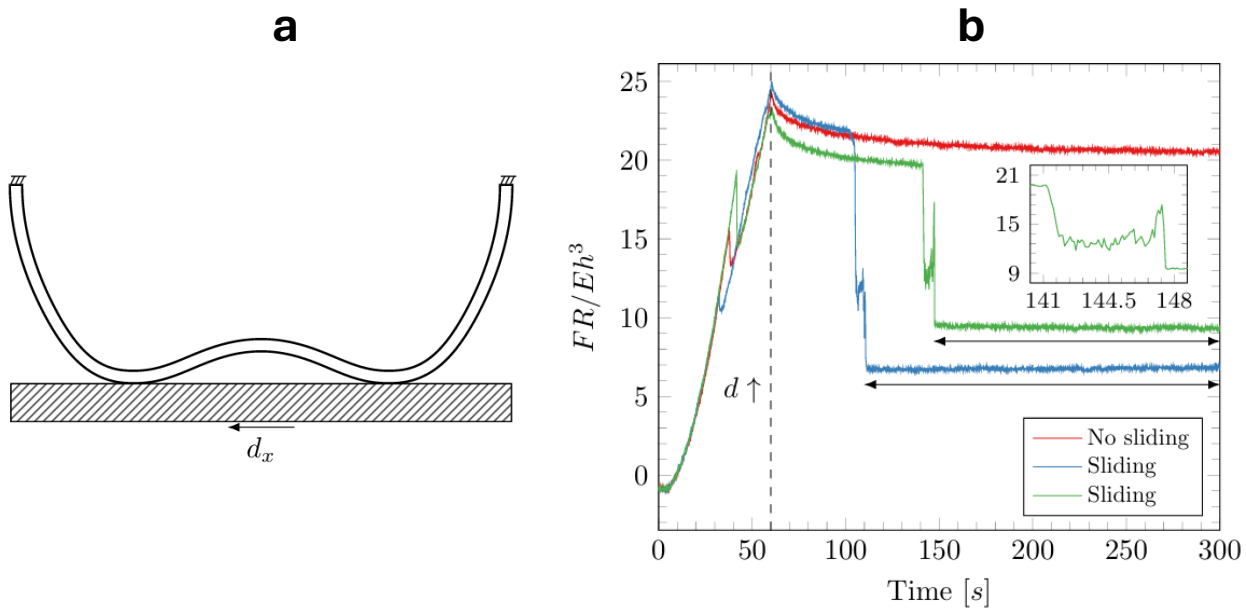

Figure 7.1: Force response observed during the sliding experiments. The hemispherical shell was subjected to an increasing indentation up to the level indicated by the dashed line in (b), after which the indentation depth was held constant. For the red curve, no sliding was applied, and a gradual relaxation in the normal force was observed. In contrast, the green and blue curves correspond to experiments where sliding was applied manually, followed by a rest period showing no relaxation or sensor drift, as indicated by the arrows. The inset provides a close-up view of the normal force as a function of time during the sliding phase.

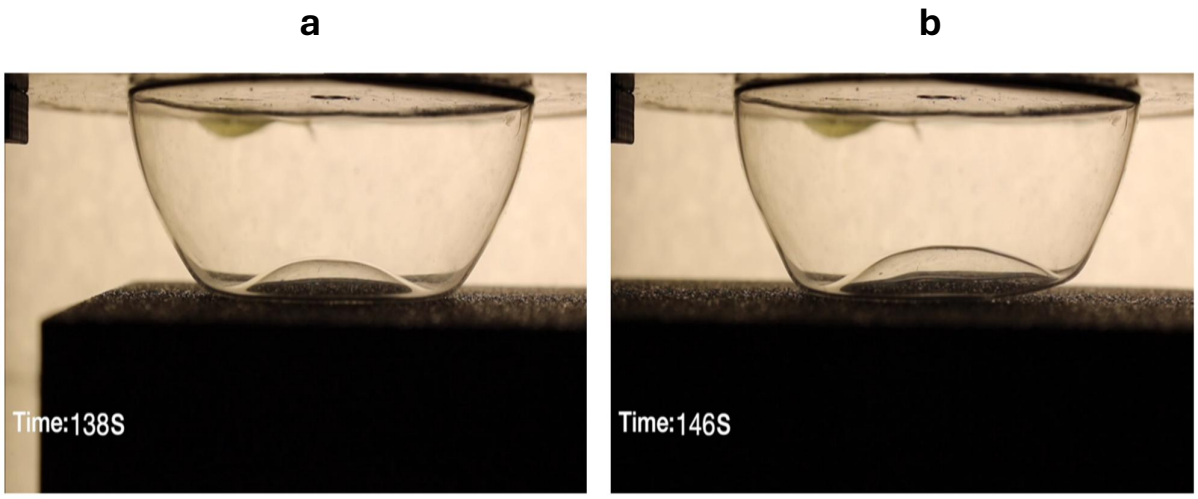

Figure 7.2: These snapshots correspond to the green curve on Figure 7.1-b. (a) Pre sliding (b) Post sliding

Appendix A. Persson's (2010) Solution for Friction in the Absence of Adhesion

Persson [87] proposed an analytical model to estimate the rolling or sliding friction of a viscoelastic solid in the absence of adhesion. In his formulation, the Hertzian pressure distribution is assumed to retain its shape during motion, although the actual pressure field becomes slightly asymmetric. Despite this simplification, the resulting prediction was shown to be in excellent agreement with the exact analytical solution previously derived by Hunter [200].

The dimensionless friction coefficient is given by

$$\mu_{\text{noadh}} = \frac{8W}{\pi R} \int_0^\infty dq_x \, \text{Im}\left[\frac{1}{E^*(q_x v)} \frac{1}{a q_x^2} J_1^2(q_x a) \right], \tag{7.1}$$

where $E^*(\omega)$ is the complex viscoelastic modulus evaluated at the frequency $\omega = q_x v$, a is the Hertzian half-width of the contact area at that frequency, expressed as

$$a = \sqrt{\frac{4WR}{\pi |E^*(q_x v)|}}, \tag{7.2}$$

and J_1 is the Bessel function of the first kind of order one.

Persson further analyzed the behavior of the normalized friction coefficient, defined as $\mu^* = \mu R / a_0$, with respect to the dimensionless rolling speed

$$V_0 = \frac{v\tau}{a_0},$$

for various values of the modulus ratio $1/k = E_\infty / E_0 = \{1.1, 2, 10, 100, 1000\}$ (Figure 7.3). The results show that the maximum normalized friction coefficient, $\max(\mu^*) = \max(\mu R / a_0)$, converges rapidly when $1/k \simeq 10$, indicating that the response becomes dominated by the high-frequency modulus E_∞ (Figure 7.4). This trend contrasts with the adhesive case analyzed in the main chapters of this thesis, where the frictional re-

sponse remains strongly influenced by the ratio E_∞/E_0.

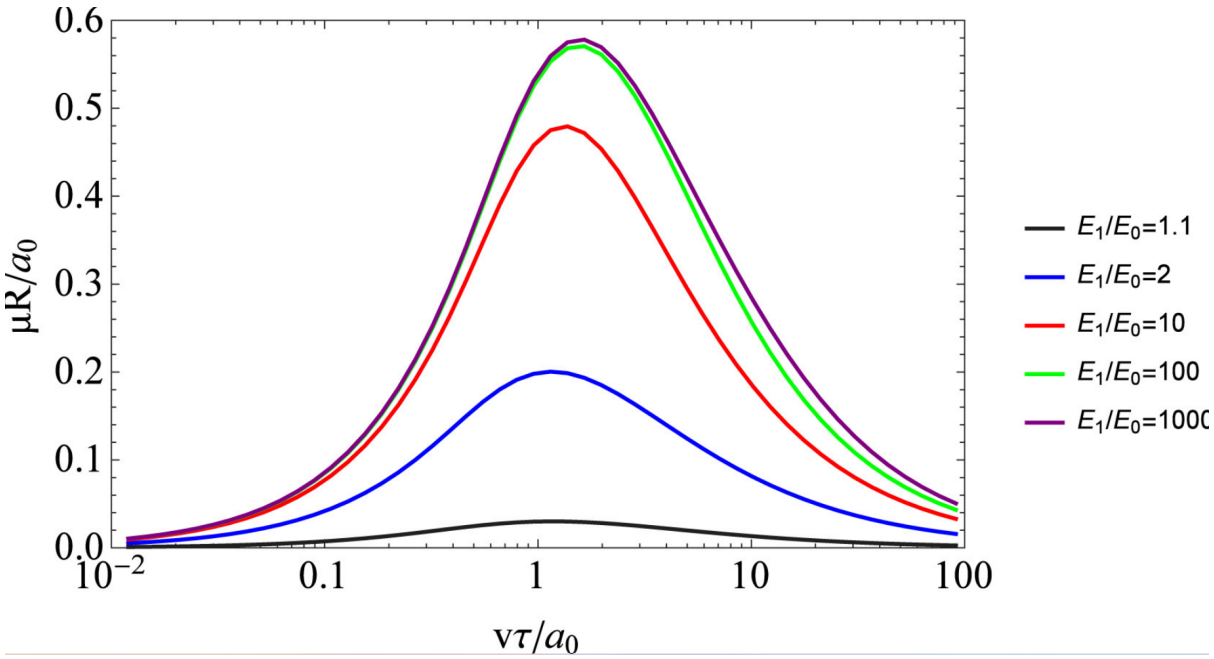

Figure 7.3: Dimensionless friction coefficient μ^* as a function of the dimensionless sliding speed, computed using the Persson solution (2010) for friction in the absence of adhesion.

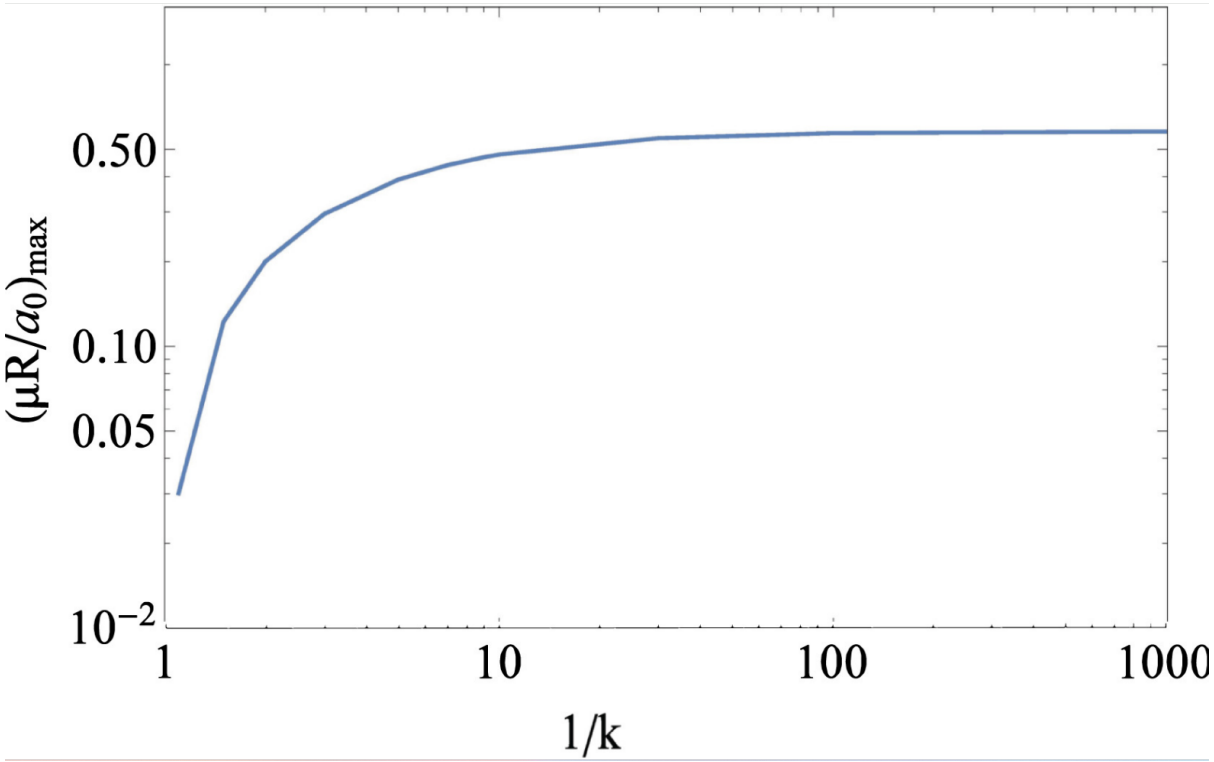

Figure 7.4: Maximum dimensionless friction coefficient $\mu^*_{\max}$ as a function of the inverse stiffness $1/k$, computed using the Persson solution (2010) for friction in the absence of adhesion.

List of Publications

During the course of this doctoral research, the following works have been published and presented:

Journal Articles

1. R. Nazari, R. Aghababaei, A. Papangelo, and M. Ciavarella, "Adhesion- and friction-induced suppression of buckling in thin spherical shells in contact with a rigid wall," *International Journal of Engineering Science*, Vol. 215, 104329, 2025.

2. A. Papangelo, R. Nazari, and M. Ciavarella, "Friction for a sliding adhesive viscoelastic cylinder: Effect of the Maugis parameter," *European Journal of Mechanics A/Solids*, Vol. 107, 105348, 2024.

3. R. Nazari, A. Papangelo, and M. Ciavarella, "Friction in rolling a cylinder on or under a viscoelastic substrate with adhesion," *Tribology Letters*, Vol. 72, Issue 2, 50, 2024.

Conference Presentation

1. R. Nazari, "The Role of Adhesion and Friction in the Buckling Behavior of Spherical Shells," presented at the *XVIII International Conference on Computational Plasticity (COMPLAS 2025)*, Barcelona, Spain, 2–5 September 2025.

Bibliography

[1] D. Maugis. Adhesion of spheres: the jkr–dmt transition using a dugdale model. *Journal of Colloid and Interface Science*, 150(1):243–269, 1992.

[2] K. L. Johnson and J. A. Greenwood. A maugis analysis of adhesive line contact. *Journal of Physics D: Applied Physics*, 41(15):155315, 2008.

[3] B. N. J. Persson. Theory of rubber friction and contact mechanics. *Journal of Chemical Physics*, 115(8):3840–3861, 2001.

[4] G. Carbone, C. Mandriota, and N. Menga. Theory of viscoelastic adhesion and friction. *Extreme Mechanics Letters*, 56:101877, 2022.

[5] S. P. Timoshenko and J. M. Gere. *Theory of Elastic Stability*. McGraw-Hill, 1961.

[6] B Audoly and Y Pomeau. *From hair curls to the non-linear response of shells*. Oxford University Press, ,UK, 2010.

[7] John W Hutchinson and J Michael T Thompson. Nonlinear buckling behaviour of spherical shells: barriers and symmetry-breaking dimples. *Philosophical Transactions of the Royal Society A: Mathematical, Physical and Engineering Sciences*, 375 (2093):20160154, 2017.

[8] Jayson Paulose and David R Nelson. Buckling pathways in spherical shells with soft spots. *Soft Matter*, 9(34):8227–8245, 2013.

[9] Takara Abe and Tomohiko G. Sano. (dis)continuous buckling transition in elastic shell mediated by contact. arXiv preprint arXiv:2503.20670, 2025.

[10] K. A. Grosch. The relation between the friction and visco-elastic properties of rubber. *Proceedings of the Royal Society of London A*, 274(1356):21–39, 1963.

[11] A. G. V. G. V. Schallamach. The velocity and temperature dependence of rubber friction. *Proceedings of the Physical Society B*, 66(5):386, 1953.

[12] R. A. Schapery. A theory of crack initiation and growth in viscoelastic media. *International Journal of Fracture*, 11(Part I):141–159, 1975.

[13] M Barquins and AD Roberts. Rubber friction variation with rate and temperature: some new observations. *Journal of Physics D: Applied Physics*, 19(4):547, 1986.

[14] J. A. Greenwood and K. L. Johnson. The mechanics of adhesion of viscoelastic solids. *Philosophical Magazine A*, 43:697–712, 1981.

[15] B. N. J. Persson. Rolling friction for hard cylinder and sphere on viscoelastic solid. *European Physical Journal E*, 33:327–333, 2010.

[16] G. Violano and L. Afferrante. Size effects in adhesive contacts of viscoelastic media. *European Journal of Mechanics A: Solids*, 96:104665, 2022.

[17] J. Plagge and R. Hentschke. Numerical solution of the adhesive rubber–solid contact problem and friction coefficients using a scale-splitting approach. *Tribology International*, 173:107622, 2022.

[18] R. Nazari, A. Papangelo, and M. Ciavarella. Friction in rolling a cylinder on or under a viscoelastic substrate with adhesion. *Tribology Letters*, 72(2):50, 2024.

[19] K. Kendall. *Molecular Adhesion and Its Applications: The Sticky Universe*. Springer, 2001.

[20] Lara J Martin and CP Wong. Chemical and mechanical adhesion mechanisms of sputter-deposited metal on epoxy dielectric for high density interconnect printed circuit boards. *IEEE Transactions on components and packaging technologies*, 24 (3):416–424, 2002.

[21] J. Shintake, V. Cacucciolo, D. Floreano, and H. Shea. Soft robotic grippers. *Advanced Materials*, 30(29):1707035, 2018. doi: 10.1002/adma.201707035.

[22] Kellar Autumn, Yiching A Liang, S Tonia Hsieh, Wolfgang Zesch, Wai Pang Chan, Thomas W Kenny, Ronald Fearing, and Robert J Full. Adhesive force of a single gecko foot-hair. *Nature*, 405(6787):681–685, 2000.

[23] Jacob N Israelachvili. *Intermolecular and surface forces*. Academic press, 2011.

[24] Wolfgang Pauli. Exclusion principle and quantum mechanics. In *Writings on physics and philosophy*, pages 165–181. Springer, 1946.

[25] JH De Boer. The influence of van der waals' forces and primary bonds on binding energy, strength and orientation, with special reference to some artificial resins. *Transactions of the Faraday Society*, 32:10–37, 1936.

[26] Roohollah Nazari and Mohammad Mahdi Hatami. A comparative study of the effect of various surface treatments on the fracture behavior of aluminum adhesive joints under mode i loading. *Discover Applied Sciences*, 6(1):8, 2024.

[27] Roohollah Nazari, Hadi Khoramishad, and Rashid Hakimi. The effect of abrading treatment method on the bonding surface characteristics and fracture behavior of glass fiber-epoxy composite adhesive joints. *Journal of Adhesion Science and Technology*, 38(13):2405–2424, 2024.

[28] Daniel Maugis. *Contact, adhesion and rupture of elastic solids*, volume 130. Springer Science & Business Media, 2000.

[29] H Hertz. English translation of miscellaneous papers (1881), 1896.

[30] Kenneth Langstreth Johnson, Kevin Kendall, and AAD Roberts. Surface energy and the contact of elastic solids. *Proceedings of the royal society of London. A. mathematical and physical sciences*, 324(1558):301–313, 1971.

[31] Boris V Derjaguin, Vladimir M Muller, and Yu P Toporov. Effect of contact deformations on the adhesion of particles. *Journal of Colloid and interface science*, 53 (2):314–326, 1975.

[32] D Tabor. Surface forces and surface interactions. In *Plenary and invited lectures*, pages 3–14. Elsevier, 1977.

[33] Daniel Maugis. Adhesion of spheres: the jkr-dmt transition using a dugdale model. *Journal of colloid and interface science*, 150(1):243–269, 1992.

[34] Maryam Kiumarsi, Ali Rafe, and Samira Yeganehzad. Effect of different bulk sweeteners on the dynamic oscillatory and shear rheology of chocolate. *Applied Rheology*, 27(6):11–19, 2017.

[35] Qiang Qiang Cheng, Peter X Liu, Pin Hua Lai, and Yan Ni Zou. An interactive meshless cutting model for nonlinear viscoelastic soft tissue in surgical simulators. *IEEE Access*, 5:16359–16371, 2017.

[36] BNJ Persson. Rubber friction and tire dynamics. *Journal of Physics: Condensed Matter*, 23(1):015003, 2010.

[37] MR James, N Bagdassarov, K Müller, and H Pinkerton. Viscoelastic behaviour of basaltic lavas. *Journal of Volcanology and Geothermal Research*, 132(2-3):99–113, 2004.

[38] Raelene M Cowie, Adam Briscoe, John Fisher, and Louise M Jennings. Wear and friction of uhmwpe-on-peek optima™. *Journal of the Mechanical Behavior of Biomedical Materials*, 89:65–71, 2019.

[39] Piaras Kelly. Solid mechanics part i: An introduction to solid mechanics. *A creative commons attributions, Mountain view, cA*, 94042, 2013.

[40] N Phan Thien and N Mai Duy. Understanding viscoelasticity: An introduction to rheology, 2017.

[41] Valentin L Popov, Markus Heß, and Emanuel Willert. *Handbook of contact mechanics: exact solutions of axisymmetric contact problems*. Springer Nature, 2019.

[42] Severino PC Marques and Guillermo J Creus. *Computational viscoelasticity*. Springer Science & Business Media, 2012.

[43] Dongze Wang, Gregory de Boer, Anne Neville, and Ali Ghanbarzadeh. A review on modelling of viscoelastic contact problems. *Lubricants*, 10(12):358, 2022.

[44] Gérard A Maugin. Viscoelasticity of solids (old and new). In *Continuum Mechanics through the Ages-From the Renaissance to the Twentieth Century: From Hydraulics to Plasticity*, pages 157–176. Springer, 2015.

[45] Albert Edward Green and Ronald S Rivlin. The mechanics of non-linear materials with memory. Technical report, 1956.

[46] Albert E Green and Ronald S Rivlin. The mechanics of non-linear materials with memory. *Archive for rational mechanics and analysis*, 4(1):387–404, 1959.

[47] Allen C Pipkin and Tryfan G Rogers. A non-linear integral representation for viscoelastic behaviour. *Journal of the Mechanics and Physics of Solids*, 16(1):59–72, 1968.

[48] Herbert Leaderman. Elastic and creep properties of filamentous materials and other high polymers. *Washington, Textile Foundation*, 1943.

[49] OS Brueller. On the nonlinear characterization of the long term behavior of polymeric materials. *Polymer Engineering & Science*, 27(2):144–148, 1987.

[50] Richard A Schapery. On the characterization of nonlinear viscoelastic materials. *Polymer Engineering & Science*, 9(4):295–310, 1969.

[51] EH Lee. Stress analysis in visco-elastic bodies. *Quarterly of applied mathematics*, 13(2):183–190, 1955.

[52] Jens Rainer Maria Radok. Visco-elastic stress analysis. *Quarterly of Applied Mathematics*, 15(2):198–202, 1957.

[53] EH Lee and Jens Rainer Maria Radok. The contact problem for viscoelastic bodies. 1960.

[54] Turner Alfrey. Non-homogeneous stresses in visco-elastic media. *Quarterly of Applied Mathematics*, 2(2):113–119, 1944.

[55] HS Tsien. A generalization of alfrey's theorem for visco-elastic media. *Quarterly of Applied Mathematics*, 8(1):104–106, 1950.

[56] SC Hunter. The hertz problem for a rigid spherical indenter and a viscoelastic half-space. *Journal of the Mechanics and Physics of Solids*, 8(4):219–234, 1960.

[57] George AC Graham. The contact problem in the linear theory of viscoelasticity. *International Journal of Engineering Science*, 3(1):27–46, 1965.

[58] W. H. Yang. The contact problem for viscoelastic bodies. *Journal of Applied Mechanics*, 33:395–401, 1966.

[59] T. C. T. Ting. The contact stresses between a rigid indenter and a viscoelastic half-space. *Journal of Applied Mechanics*, 33:845–854, 1966.

[60] T. C. T. Ting. Contact problems in the linear theory of viscoelasticity. *Journal of Applied Mechanics*, 35:248–254, 1968.

[61] M. L. Oyen. Analytical techniques for indentation of viscoelastic materials. *Philosophical Magazine*, 86:5625–5641, 2006.

[62] J. A. Greenwood. Contact between an axisymmetric indenter and a viscoelastic half-space. *International Journal of Mechanical Sciences*, 52:829–835, 2010.

[63] G. Fu. Theoretical study of complete contact indentations of viscoelastic materials. *Journal of Materials Science*, 39:2877–2878, 2004.

[64] A. Yakovenko and I. Goryacheva. The periodic contact problem for spherical indenters and viscoelastic half-space. *Tribology International*, 161:107078, 2021.

[65] A. Papangelo and M. Ciavarella. Viscoelastic dissipation in repeated normal indentation of a hertzian profile. *International Journal of Solids and Structures*, 236–237: 111362, 2022.

[66] I. Argatov and G. Mishuris. Frictionless elliptical contact of thin viscoelastic layers bonded to rigid substrates. *Applied Mathematical Modelling*, 35:3201–3212, 2011.

[67] I. Argatov. An analytical solution of the rebound indentation problem for an isotropic linear viscoelastic layer loaded with a spherical punch. *Acta Mechanica*, 223:1441–1453, 2012.

[68] I. Argatov and G. Mishuris. An analytical solution for a linear viscoelastic layer loaded with a cylindrical punch: Evaluation of the rebound indentation test with application for assessing viability of articular cartilage. *Mechanics Research Communications*, 38:565–568, 2011.

[69] Y.-H. Chen, Y. Jia, F. Yang, C.-C. Huang, and S. Lee. Boussinesq problem of a burgers viscoelastic layer on an elastic substrate. *Mechanics of Materials*, 87:27–39, 2015.

[70] I. Kozhevnikov, J. Cesbron, D. Duhamel, H. Yin, and F. Anfosso-Lédée. A new algorithm for computing the indentation of a rigid body of arbitrary shape on a viscoelastic half-space. *International Journal of Mechanical Sciences*, 50:1194–1202, 2008.

[71] I. Kozhevnikov, D. Duhamel, H. Yin, and Z.-Q. Feng. A new algorithm for solving the multi-indentation problem of rigid bodies of arbitrary shapes on a viscoelastic half-space. *International Journal of Mechanical Sciences*, 52:399–409, 2010.

[72] J. Boussinesq. *Applications des Potentiels à l'étude de l'équilibre et du mouvement des solides élastiques*. Gauthier–Villard, Paris, France, 1885.

[73] W Wayne Chen, Q Jane Wang, Z Huan, and X Luo. Semi-analytical viscoelastic contact modeling of polymer-based materials. 2011.

[74] K. E. Koumi, D. Nelias, T. Chaise, and A. Duval. Modeling of the contact between a rigid indenter and a heterogeneous viscoelastic material. *Mechanics of Materials*, 77:28–42, 2014.

[75] Y. Liu, W. Wang, Z. Zhao, and H. Zhang. The effect of meso-structure and surface topography on the indentation variability of viscoelastic composite materials. *Composites Structures*, 220:81–92, 2019.

[76] S. Spinu. Viscoelastic contact modelling: Application to the finite length line contact. *Tribology in Industry*, 40:538–551, 2018.

[77] Y. Zhao, G. Morales-Espejel, and C. Venner. Aspects of modeling and numerical simulation of dry point contacts between viscoelastic solids. *Tribology International*, 165:107245, 2021.

[78] V. T. Nguyen and C. Hwu. Boundary element method for contact between multiple rigid punches and anisotropic viscoelastic foundation. *Engineering Analysis with Boundary Elements*, 118:295–305, 2020.

[79] V. T. Nguyen and C. Hwu. Indentation by multiple rigid punches on two-dimensional anisotropic elastic or viscoelastic solids. *International Journal of Mechanical Sciences*, 178:105595, 2020.

[80] E. Olsson and D. Jelagin. A contact model for the normal force between viscoelastic particles in discrete element simulations. *Powder Technology*, 342:985–991, 2019.

[81] D. Wang, G. de Boer, and A. Ghanbarzadeh. A numerical model for investigating the effect of viscoelasticity on the partial slip solution. *Materials*, 15:5182, 2022.

[82] K. E. Koumi, T. Chaise, and D. Nelias. Rolling contact of a rigid sphere/sliding of a spherical indenter upon a viscoelastic half-space containing an ellipsoidal inhomogeneity. *Journal of the Mechanics and Physics of Solids*, 80:1–25, 2015.

[83] S.C. Hunter. The rolling contact of a rigid cylinder with a viscoelastic half space. *Journal of Applied Mechanics*, 28:611–617, 1961. doi: 10.1115/1.3641789.

[84] L.W. Morland. Exact solutions for rolling contact between viscoelastic cylinders. *Quarterly Journal of Mechanics and Applied Mathematics*, 20:73–106, 1967. doi: 10.1093/qjmam/20.1.73.

[85] C. Panek and J.J. Kalker. Three-dimensional contact of a rigid roller traversing a viscoelastic half space. *IMA Journal of Applied Mathematics*, 26:299–313, 1980. doi: 10.1093/imamat/26.3.299.

[86] V.M. Aleksandrov, I.G. Goryacheva, and E.V. Torskaya. Sliding contact of a smooth indenter and a viscoelastic half-space (3d problem). *Doklady Physics*, 55:77–80, 2010. doi: 10.1134/S1028335810020055.

[87] B.N.J. Persson. Rolling friction for hard cylinder and sphere on viscoelastic solid. *European Physical Journal E*, 33:327–333, 2010. doi: 10.1140/epje/i2010-10663-3.

[88] J. Padovan and O. Paramadilok. Transient and steady state viscoelastic rolling contact. *Computers and Structures*, 20:545–553, 1985. doi: 10.1016/0045-7949(85)90149-4.

[89] L. Nasdala, M. Kaliske, A. Becker, and H. Rothert. An efficient viscoelastic formulation for steady-state rolling structures. *Computational Mechanics*, 22:395–403, 1998. doi: 10.1007/s004660050380.

[90] P. Le Tallec and C. Rahler. Numerical models of steady rolling for non-linear viscoelastic structures in finite deformations. *International Journal for Numerical Methods in Engineering*, 37:1159–1186, 1994. doi: 10.1002/nme.1620370704.

[91] U. Nackenhorst. The ale-formulation of bodies in rolling contact: Theoretical foundations and finite element approach. *Computer Methods in Applied Mechanics and Engineering*, 193:4299–4322, 2004. doi: 10.1016/j.cma.2004.01.039.

[92] J. Padovan, A. Kazempour, F. Tabaddor, and B. Brockman. Alternative formulations of rolling contact problems. *Finite Elements in Analysis and Design*, 11:275–284, 1992. doi: 10.1016/0168-874X(92)90017-V.

[93] G. Carbone and C. Putignano. A novel methodology to predict sliding and rolling friction of viscoelastic materials: Theory and experiments. *Journal of the Mechanics and Physics of Solids*, 61:1822–1834, 2013. doi: 10.1016/j.jmps.2013.04.001.

[94] N. Menga, C. Putignano, G. Carbone, and G.P. Demelio. The sliding contact of a rigid wavy surface with a viscoelastic half-space. *Proceedings of the Royal Society A: Mathematical, Physical and Engineering Sciences*, 470:20140392, 2014. doi: 10.1098/rspa.2014.0392.

[95] C. Putignano, G. Carbone, and D. Dini. Mechanics of rough contacts in elastic and viscoelastic thin layers. *International Journal of Solids and Structures*, 69-70: 507–517, 2015. doi: 10.1016/j.ijsolstr.2015.05.005.

[96] N. Menga, L. Afferrante, and G. Carbone. Effect of thickness and boundary conditions on the behavior of viscoelastic layers in sliding contact with wavy profiles. *Journal of the Mechanics and Physics of Solids*, 95:517–529, 2016. doi: 10.1016/j.jmps.2016.05.013.

[97] N. Menga, L. Afferrante, G. Demelio, and G. Carbone. Rough contact of sliding viscoelastic layers: Numerical calculations and theoretical predictions. *Tribology International*, 122:67–75, 2018. doi: 10.1016/j.triboint.2018.02.017.

[98] E.V. Torskaya and F.I. Stepanov. Effect of surface layers in sliding contact of viscoelastic solids (3-d model of material). *Frontiers in Mechanical Engineering*, 5: 26, 2019. doi: 10.3389/fmech.2019.00026.

[99] F.I. Stepanov and E.V. Torskaya. Study of stress state of viscoelastic half-space in sliding contact with smooth indenter. *Journal of Friction and Wear*, 37:101–106, 2016. doi: 10.3103/S1068366616020098.

[100] J.S. van Dokkum and L. Nicola. Green's function molecular dynamics including viscoelasticity. *Modelling and Simulation in Materials Science and Engineering*, 27: 075006, 2019. doi: 10.1088/1361-651X/ab3b23.

[101] E.R. Wallace, T. Chaise, and D. Nelias. Three-dimensional rolling/sliding contact on a viscoelastic layered half-space. *Journal of the Mechanics and Physics of Solids*, 143:104067, 2020. doi: 10.1016/j.jmps.2020.104067.

[102] X. Zhang, Q.J. Wang, and T. He. Transient and steady-state viscoelastic contact responses of layer-substrate systems with interfacial imperfections. *Journal of the Mechanics and Physics of Solids*, 145:104170, 2020. doi: 10.1016/j.jmps.2020.104170.

[103] S.K. Dayalan and N.K. Sundaram. Partial slip contact of a rigid pin and a linear viscoelastic plate. *International Journal of Solids and Structures*, 100:319–331, 2016. doi: 10.1016/j.ijsolstr.2016.09.018.

[104] J. Bonari and M. Paggi. Viscoelastic effects during tangential contact analyzed by a novel finite element approach with embedded interface profiles. *Lubricants*, 8:107, 2020. doi: 10.3390/lubricants8050107.

[105] V.T. Nguyen and C. Hwu. Time-stepping method for frictional contact of anisotropic viscoelastic solids. *International Journal of Mechanical Sciences*, 184: 105836, 2020. doi: 10.1016/j.ijmecsci.2020.105836.

[106] I. Goriacheva. Contact problem of rolling of a viscoelastic cylinder on a base of the same material. *Journal of Applied Mathematics and Mechanics*, 37:877–885, 1973. doi: 10.1016/0021-8928(73)90089-3.

[107] L.E. Goodman. Contact stress analysis of normally loaded rough spheres. *Journal of Applied Mechanics*, 29:515–522, 1962. doi: 10.1115/1.3636562.

[108] I. Goryacheva and F. Sadeghi. Contact characteristics of a rolling/sliding cylinder and a viscoelastic layer bonded to an elastic substrate. *Wear*, 184:125–132, 1995. doi: 10.1016/0043-1648(94)06527-B.

[109] I. Goryacheva, F. Stepanov, and E. Torskaya. Sliding of a smooth indentor over a viscoelastic half-space when there is friction. *Journal of Applied Mathematics and Mechanics*, 79:596–603, 2015. doi: 10.1016/j.jappmathmech.2015.07.005.

[110] I. Goryacheva, F. Stepanov, and E. Torskaya. Effect of friction in sliding contact of a sphere over a viscoelastic half-space. In P. Neittaanmäki, S. Repin, and T. Tuovinen, editors, *Mathematical Modeling and Optimization of Complex Structures*, pages 93–103. Springer International Publishing, Cham, Switzerland, 2016. doi: 10.1007/978-3-319-23449-4_8.

[111] I. Goryacheva and A. Miftakhova. Modelling of the viscoelastic layer effect in rolling contact. *Wear*, 430–431:256–262, 2019. doi: 10.1016/j.wear.2019.05.002.

[112] C. Putignano, G. Carbone, and D. Dini. Theory of reciprocating contact for viscoelastic solids. *Physical Review E*, 93:043003, 2016. doi: 10.1103/PhysRevE.93.043003.

[113] C. Putignano and G. Carbone. Viscoelastic reciprocating contacts in presence of finite rough interfaces: A numerical investigation. *Journal of the Mechanics and Physics of Solids*, 114:185–193, 2018. doi: 10.1016/j.jmps.2018.02.014.

[114] M. Santeramo, C. Putignano, G. Vorlaufer, S. Krenn, and G. Carbone. Viscoelastic steady-state rolling contacts: A generalized boundary element formulation for conformal and non-conformal geometries. *Journal of the Mechanics and Physics of Solids*, 171:105129, 2023. doi: 10.1016/j.jmps.2023.105129.

[115] Valentin L Popov. *Contact mechanics and friction*. Berlin: Springer Berlin Heidelberg., 2010.

[116] D. Maugis and M. Barquins. Fracture mechanics and adherence of viscoelastic solids. In L.-H. Lee, editor, *Adhesion and Adsorption of Polymers*, pages 203–277. Springer, Boston, MA, USA, 1980. doi: 10.1007/978-1-4613-3042-6_5.

[117] J.A. Greenwood and K.L. Johnson. The mechanics of adhesion of viscoelastic solids. *Philosophical Magazine A*, 43:697–711, 1981. doi: 10.1080/01418618108240494.

[118] V. Muller. On the theory of pull-off of a viscoelastic sphere from a flat surface. *Journal of Adhesion Science and Technology*, 13:999–1016, 1999. doi: 10.1163/156856199X00689.

[119] C.-Y. Hui, J.M. Baney, and E.J. Kramer. Contact mechanics and adhesion of viscoelastic spheres. *Langmuir*, 14:6570–6578, 1998. doi: 10.1021/la9803502.

[120] TCT Ting. The contact stresses between a rigid indenter and a viscoelastic half-space. *Journal of Applied Mechanics*, 33(4):845–854, 1966.

[121] G. Haiat, M.P. Huy, and E. Barthel. The adhesive contact of viscoelastic spheres. *Journal of the Mechanics and Physics of Solids*, 51:69–99, 2003. doi: 10.1016/S0022-5096(02)00075-6.

[122] Y.-Y. Lin and C.-Y. Hui. Mechanics of contact and adhesion between viscoelastic spheres: An analysis of hysteresis during loading and unloading. *Journal of Polymer Science Part B: Polymer Physics*, 40:772–793, 2002. doi: 10.1002/polb.10118.

[123] D.S. Dugdale. Yielding of steel sheets containing slits. *Journal of the Mechanics and Physics of Solids*, 8:100–104, 1960. doi: 10.1016/0022-5096(60)90013-2.

[124] G.I. Barenblatt. The mathematical theory of equilibrium cracks in brittle fracture. In H.L. Dryden, T. von Kármán, G. Kuerti, F.H. van den Dungen, and L. Howarth, editors, *Advances in Applied Mechanics*, volume 7, pages 55–129. Elsevier, Cambridge, MA, USA, 1962. doi: 10.1016/S0065-2156(08)70121-2.

[125] E. Bärthel and C. Frétigny. Adhesive contact of elastomers: Effective adhesion energy and creep function. *Journal of Physics D: Applied Physics*, 42:195302, 2009. doi: 10.1088/0022-3727/42/19/195302.

[126] H. Yu, Z. Li, and Q.J. Wang. Viscoelastic-adhesive contact modeling: Application to the characterization of the viscoelastic behavior of materials. *Mechanics of Materials*, 60:55–65, 2013. doi: 10.1016/j.mechmat.2013.01.001.

[127] I.G. Goryacheva, M.M. Gubenko, and Y.Y. Makhovskaya. Sliding of a spherical indenter on a viscoelastic foundation with the forces of molecular attraction taken into account. *Journal of Applied Mechanics and Technical Physics*, 55:81–88, 2014. doi: 10.1134/S0021894414010122.

[128] L. Afferrante and G. Violano. On the effective surface energy in viscoelastic hertzian contacts. *Journal of the Mechanics and Physics of Solids*, 158:104669, 2021. doi: 10.1016/j.jmps.2021.104669.

[129] V.B. Derjaguin. Theorie des anhaftens kleiner teilchen. *Progress in Surface Science*, 40:6–15, 1992. doi: 10.1016/0079-6816(92)90032-Y.

[130] M.H. Müser and B.N.J. Persson. Crack and pull-off dynamics of adhesive, viscoelastic solids. *EPL (Europhysics Letters)*, 137:36004, 2022. doi: 10.1209/0295-5075/ac45e2.

[131] B.N.J. Persson and E.A. Brener. Crack propagation in viscoelastic solids. *Physical Review E*, 71:036123, 2005. doi: 10.1103/PhysRevE.71.036123.

[132] G. Carbone, C. Mandriota, and N. Menga. Theory of viscoelastic adhesion and friction. *Extreme Mechanics Letters*, 56:101877, 2022. doi: 10.1016/j.eml.2022.101877.

[133] W. Yang, X. Wang, P. Chen, and X. Qiao. Viscoelastic adhesive contact between a sphere and a two-dimensional nano-wavy surface. *Applied Surface Science*, 586:152828, 2022. doi: 10.1016/j.apsusc.2022.152828.

[134] F. Pérez-Ràfols, J.S. Van Dokkum, and L. Nicola. On the interplay between roughness and viscoelasticity in adhesive hysteresis. *Journal of the Mechanics and Physics of Solids*, 170:105079, 2023. doi: 10.1016/j.jmps.2023.105079.

[135] U. Seifert and R. Lipowsky. Adhesion of vesicles. *Physical Review A*, 42(8):4768–4771, 1990. doi: 10.1103/PhysRevA.42.4768.

[136] Jacob N. Israelachvili. *Intermolecular and Surface Forces*. Academic Press, London, 3rd edition, 2011. ISBN 978-0123919274.

[137] C. Majidi and K. T. Wan. Adhesion of thin-walled cylindrical shells to substrates. *Journal of Applied Mechanics*, 74(5):1097–1103, 2007. doi: 10.1115/1.2722328.

[138] J. W. Hutchinson. Buckling of spherical shells revisited. *Proceedings of the Royal Society A: Mathematical, Physical and Engineering Sciences*, 472(2195):20160577, 2016. doi: 10.1098/rspa.2016.0577.

[139] A. V. Pogorelov. *Bendings of Surfaces and Stability of Shells*. American Mathematical Society, Providence, RI, 1988. ISBN 978-0821845328.

[140] C. Majidi. Soft adhesion mechanics: concepts and recent progress. *Soft Matter*, 5 (17):3382–3390, 2009. doi: 10.1039/B903686C.

[141] M. Barquins. Rolling friction of a rigid cylinder on a viscoelastic substrate. *Journal of Colloid and Interface Science*, 109(2):542–556, 1985. doi: 10.1016/0021-9797(85) 90337-7.

[142] K. L. Johnson. Adhesion and friction between a smooth elastic spherical asperity and a plane surface. *Proceedings of the Royal Society A: Mathematical, Physical and Engineering Sciences*, 453(1956):163–179, 1997. doi: 10.1098/rspa.1997.0011.

[143] B. N. J. Persson and A. I. Volokitin. Rubber friction on smooth surfaces. *European Physical Journal E*, 21:69–80, 2006.

[144] Roohollah Nazari, Ramin Aghababaei, Antonio Papangelo, and Michele Ciavarella. Adhesion-and friction-induced suppression of buckling in thin spherical shells in contact with a rigid wall. *International Journal of Engineering Science*, 215:104329, 2025.

[145] Liding Chen, Yufen Xu, Tingting Fan, Zhenkai Liao, Peng Wu, Xuee Wu, and Xiao Dong Chen. Gastric emptying and morphology of a 'near real'in vitro human stomach model (rd-iv-hsm). *Journal of Food Engineering*, 183:1–8, 2016.

[146] Jie Yin, Xi Chen, and Izhak Sheinman. Anisotropic buckling patterns in spheroidal film/substrate systems and their implications in some natural and biological systems. *Journal of the Mechanics and Physics of Solids*, 57(9):1470–1484, 2009.

[147] Hui Zheng, Peijian Chen, and Zhitong Chen. Cold-atmospheric-plasma–induced skin wrinkle. *Europhysics Letters*, 133(1):15001, 2021.

[148] Takara Abe, Isamu Hashiguchi, Yukitake Nakahara, Shunsuke Kobayashi, Ryuichi Tarumi, Hidetoshi Takahashi, Genya Ishigami, and Tomohiko G Sano. Snap and jump: How elastic shells pop out. *arXiv preprint arXiv:2410.08525*, 2024.

[149] Sen Lin, Yi Min Xie, Qing Li, Xiaodong Huang, Zhe Zhang, Guowei Ma, and Shiwei Zhou. Shell buckling: from morphogenesis of soft matter to prospective applications. *Bioinspiration & Biomimetics*, 13(5):051001, 2018.

[150] Ludovic Pauchard and S Rica. Contact and compression of elastic spherical shells: the physics of a 'ping-pong'ball. *Philosophical Magazine B*, 78(2):225–233, 1998.

[151] Chuan Qiao, Lu Liu, and Damiano Pasini. Elastic thin shells with large axisymmetric imperfection: from bifurcation to snap-through buckling. *Journal of the Mechanics and Physics of Solids*, 141:103959, 2020.

[152] D. P. Holmes and A. J. Crosby. Snapping surfaces. *Advanced Materials*, 19(21): 3589–3593, 2007. doi: 10.1002/adma.200700617.

[153] S. Kim et al. Snap-through instability of graphene membranes for nanomechanical switches. *Nano Letters*, 12(1):449–454, 2012.

[154] S. M. Sze and K. K. Ng. *Physics of Semiconductor Devices*. Wiley-Interscience, 3 edition, 2006.

[155] Avinoam Libai. *The nonlinear theory of elastic shells: One spatial dimension*. Cambridge University Press, Cambridge, 2012.

[156] J.G. Teng and J.M. Rotter. Buckling of thin shells: an overview. In *Buckling of Thin Metal Shells*, pages 25–65. CRC Press, UK, 2014.

[157] S Trabelsi, A Frikha, S Zghal, and F Dammak. Thermal post-buckling analysis of functionally graded material structures using a modified fsdt. *International Journal of Mechanical Sciences*, 144:74–89, 2018.

[158] Jia-Qin Xu and Gui-Lin She. Thermal post-buckling of graphene platelet reinforced metal foams doubly curved shells with geometric imperfection. *Structural Engineering and Mechanics, An Int'l Journal*, 87(1):85–94, 2023.

[159] Yi-Wen Zhang, Gui-Lin She, Lei-Lei Gan, and Yin-Ping Li. Thermal post-buckling behavior of gplrmf cylindrical shells with initial geometrical imperfection. *Geomechanics and Engineering*, 32(6):615–625, 2023.

[160] NK Gupta, N Mohamed Sheriff, and R Velmurugan. Experimental and theoretical studies on buckling of thin spherical shells under axial loads. *International journal of mechanical sciences*, 50(3):422–432, 2008.

[161] Yan Zhao, Yanping Cao, Xi-Qiao Feng, and Kang Ma. Axial compression-induced wrinkles on a core–shell soft cylinder: Theoretical analysis, simulations and experiments. *Journal of the Mechanics and Physics of Solids*, 73:212–227, 2014.

[162] Alice Nasto, Amin Ajdari, Arnaud Lazarus, Ashkan Vaziri, and Pedro M Reis. Localization of deformation in thin shells under indentation. *Soft Matter*, 9(29): 6796–6803, 2013.

[163] Yu-Chien Tseng, Pierre Amon, Loan M Dolbachian, and Jia-Yang Juang. Guided buckling of elastoplastic spherical shells induced by indenters of various shapes. *Extreme Mechanics Letters*, 44:101247, 2021.

[164] Alexander Yu Evkin. Large deflections of deep orthotropic spherical shells under radial concentrated load: asymptotic solution. *International Journal of Solids and Structures*, 42(3-4):1173–1186, 2005.

[165] Yiheng Sun, Guangjian Peng, Yahao Hu, Guijing Dou, Peijian Chen, and Taihua Zhang. Spherical indentation model for evaluating the elastic properties of the shell of microsphere with core-shell structure. *International Journal of Solids and Structures*, 230:111159, 2021.

[166] Xuan Cuong Nguyen, Yoshio Arai, and Wakako Araki. Effect of friction on buckling behavior in shallow spherical to hemispherical shells in contact with rigid boundaries under uniform external pressure. *Advances in Science and Technology. Research Journal*, 18(1), 2024.

[167] Riad Sahli, Jeppe Mikkelsen, Mathias Sätherström Boye, Marcelo A Dias, and Ramin Aghababaei. Frictional contact of soft polymeric shells. *Physical Review Letters*, 133(10):106202, 2024.

[168] Yufei Wu, Peijian Chen, Jun Liu, and Hui Zheng. Buckling behavior of soft spherical shells with patterned surface under indentation. *International Journal of Mechanical Sciences*, 270:109113, 2024.

[169] US Schwarz, S Komura, and SA Safran. Deformation and tribology of multi-walled hollow nanoparticles. *Europhysics Letters*, 50(6):762, 2000.

[170] Jiayi Shi, Sinan Müftü, and Kai-Tak Wan. Adhesion of an elastic convex shell onto a rigid plate. *The Journal of Adhesion*, 87(6):579–594, 2011.

[171] Richard M Springman and John L Bassani. Mechano-chemical coupling in the adhesion of thin-shell structures. *Journal of the Mechanics and Physics of Solids*, 57(6):909–931, 2009.

[172] RM Springman and JL Bassani. Mechano-chemical coupling in shell adhesion. In *IUTAM Symposium on Cellular, Molecular and Tissue Mechanics: Proceedings of the IUTAM symposium held at Woods Hole, Mass., USA, June 18-21, 2008*, pages 215–225. Springer, 2010.

[173] Chenxu Zhao, Xuanhan Chen, Wanliang Shan, and Kai-tak Wan. Adherence of a hyperelastic shell on a rigid planar substrate. *International Journal of Solids and Structures*, 236:111351, 2022.

[174] Andrea Cazzolli and Fabio Dal Corso. Snapping of elastic strips with controlled ends. *International Journal of Solids and Structures*, 162:285–303, 2019.

[175] Dean Pierson Updike and Arturs Kalnins. Axisymmetric behavior of an elastic spherical shell compressed between rigid plates. *J. Appl. Mech.*, 37, 635– 640, 1970.

[176] Dean Pierson Updike and Arturs Kalnins. Axisymmetric postbuckling and nonsymmetric buckling of a spherical shell compressed between rigid plates. *J. Appl. Mech.*, 39, 172., 1972.

[177] Antonio Papangelo, Roberto Lovino, and Michele Ciavarella. Electroadhesive sphere-flat contact problem: A comparison between dmt and full iterative finite element solutions. *Tribology international*, 152:106542, 2020.

[178] Dov Shilkrut and Eduard Riks. *Stability of nonlinear shells: on the example of spherical shells*. Elsevier, Amsterdam, 2002.

[179] Dean Pierson Updike and Arturs Kalnins. Contact pressure between an elastic spherical shell and a rigid plate. *J. Appl. Mech.*, 39, 1110, 1972.

[180] Ian D Johnston, Daniel K McCluskey, Christabel KL Tan, and Monica C Tracey. Mechanical characterization of bulk sylgard 184 for microfluidics and microengineering. *Journal of Micromechanics and Microengineering*, 24(3):035017, 2014.

[181] Anna Lee, P-T Brun, J Marthelot, G Balestra, F Gallaire, and Pedro M Reis. Fabrication of slender elastic shells by the coating of curved surfaces. *Nature communications*, 7(1):11155, 2016.

[182] Michele Ciavarella, J Joe, Antonio Papangelo, and JR Barber. The role of adhesion in contact mechanics. *Journal of the Royal Society Interface*, 16(151):20180738, 2019.

[183] Michele Ciavarella. Universal features in "stickiness" criteria for soft adhesion with rough surfaces. *Tribology International*, 146:106031, 2020.

[184] CR Calladine. Understanding imperfection-sensitivity in the buckling of thin-walled shells. *Thin-walled structures*, 23(1-4):215–235, 1995.

[185] Chenxu Zhao, Kai-tak Wan, and Wanliang Shan. Progressive adhesion mechanics of elastomeric shells against a rigid substrate: From thin to thick. *Extreme Mechanics Letters*, 68:102140, 2024.

[186] A Papangelo, R Nazari, and M Ciavarella. Friction for a sliding adhesive viscoelastic cylinder: Effect of maugis parameter. *European Journal of Mechanics-A/Solids*, 107:105348, 2024.

[187] A. Schallamach. The load dependence of rubber friction. *Proceedings of the Physical Society B*, 65(9):657, 1952.

[188] A. Schallamach. How does rubber slide? *Wear*, 17(4):301–312, 1971.

[189] A. D. Roberts and S. A. Jackson. Sliding friction of rubber. *Nature*, 257(5522): 118–120, 1975.

[190] KA Grosch. The relation between the friction and visco-elastic properties of rubber. *Proceedings of the Royal Society of London. Series A. Mathematical and Physical Sciences*, 274(1356):21–39, 1963.

[191] M. L. Williams, R. F. Landel, and J. D. Ferry. The temperature dependence of relaxation mechanisms in amorphous polymers and other glass-forming liquids. *Journal of the American Chemical Society*, 77(14):3701–3707, 1955.

[192] J. A. Greenwood. The theory of viscoelastic crack propagation and healing. *Journal of Physics D: Applied Physics*, 37(18):2557, 2004.

[193] D. Tabor. Surface forces and surface interactions. In *Plenary and Invited Lectures*, pages 3–14. Academic Press, 1977.

[194] L. Afferrante and G. Violano. On the effective surface energy in viscoelastic hertzian contacts. *Journal of the Mechanics and Physics of Solids*, 158:104669, 2022.

[195] M. Ciavarella, Q. A. Wang, and Q. Li. Maugis–tabor parameter dependence of pull-off in viscoelastic line hertzian contacts. *Journal of Adhesion*, 99(6):972–987, 2023.

[196] J. J. Wu. Adhesive contact between a cylinder and a half-space. *Journal of Physics D: Applied Physics*, 42(15):155302, 2009.

[197] A. Papangelo and M. Ciavarella. A numerical study on roughness-induced adhesion enhancement in a sphere with an axisymmetric sinusoidal waviness using lennard–jones interaction law. *Lubricants*, 8(9):90, 2020.

[198] A. Papangelo and M. Ciavarella. Detachment of a rigid flat punch from a viscoelastic material. *Tribology Letters*, 71(2):48, 2023.

[199] L. Afferrante and G. Carbone. The ultratough peeling of elastic tapes from viscoelastic substrates. *Journal of the Mechanics and Physics of Solids*, 96:223–234, 2016.

[200] S. C. Hunter. The rolling contact of a rigid cylinder with a viscoelastic half space. *Journal of Applied Mechanics*, 28(4):611, 1961.

[201] C. Mandriota, N. Menga, and G. Carbone. Adhesive contact mechanics of viscoelastic materials. *International Journal of Solids and Structures*, 290:112685, 2024.

[202] G. A. C. Graham. Two extending crack problems in linear viscoelasticity theory. *Quarterly of Applied Mathematics*, 27:497–507, 1969.

[203] J. R. Rice. Mechanics of quasi-static crack growth. Technical Report COO-3084-63; CONF-780608-3, Brown University, Division of Engineering, Providence, RI (USA), 1978.

[204] Richard A Schapery. A theory of viscoelastic crack growth-revisited (revised), 2021.

[205] Bo NJ Persson. Theory of rubber friction and contact mechanics. *The Journal of Chemical Physics*, 115(8):3840–3861, 2001.

[206] A. Lang and M. Klüppel. Influences of temperature and load on the dry friction behavior of tire tread compounds in contact with rough granite. *Wear*, 380:15–25, 2017.

[207] R. Hentschke and J. Plagge. Scaling theory of rubber sliding friction. *Scientific Reports*, 11(1):1–7, 2021.

[208] Romain Bugnicourt. *Simulation of the Contact between a Rough Surface and a Viscoelastic Material with Friction*. PhD thesis, Université de Lyon, 2017.

[209] R Nazari, A Papangelo, and M Ciavarella. Friction in rolling a cylinder on or under a viscoelastic substrate with adhesion. *Tribology Letters*, 72(2):50, 2024.

[210] M. Barquins. Adherence and rolling kinetics of a rigid cylinder in contact with a natural rubber surface. *Journal of Adhesion*, 26(1):1–12, 1988. doi: 10.1080/00218468808071271.

[211] J. C. Charmet and M. Barquins. Adhesive contact and rolling of a rigid cylinder under the pull of gravity on the underside of a smooth-surfaced sheet of rubber. *International Journal of Adhesion and Adhesives*, 16(4):249–254, 1996.

[212] B. N. J. Persson and E. A. Brener. Crack propagation in viscoelastic solids. *Physical Review E*, 71(3):036123, 2005.

[213] M. Barquins and A. D. Roberts. Rubber friction variation with rate and temperature: some new observations. *Journal of Physics D: Applied Physics*, 19(4):547, 1986.

[214] M. Ciavarella, G. Cricrì, and R. McMeeking. A comparison of crack propagation theories in viscoelastic materials. *Theoretical and Applied Fracture Mechanics*, 116: 103113, 2021.

[215] C. Y. Hui, B. Zhu, and R. Long. Steady state crack growth in viscoelastic solids: a comparative study. *Journal of the Mechanics and Physics of Solids*, 159:104748, 2022.

[216] R. Sahli, G. Pallares, C. Ducottet, I. E. Ben Ali, S. Al Akhrass, M. Guibert, and J. Scheibert. Evolution of real contact area under shear and the value of static friction of soft materials. *Proceedings of the National Academy of Sciences*, 115(3): 471–476, 2018.

[217] Frank Philip Bowden and David Tabor. *The Friction and Lubrication of Solids*, volume 1. Oxford University Press, 2001.